

NOTE TO USERS

This reproduction is the best copy available.

UMI[®]

Modeling and real-time control of sheet reheat phase in thermoforming

Mark Ajersch

Department of Electrical and Computer Engineering
Centre for Intelligent Machines – Systems and Control Group
Industrial Automation Lab
McGill University, Montreal, Canada
August 2004

A thesis submitted to McGill University in partial fulfillment of the requirements of a
Masters degree in Electrical and Computer Engineering

© **Mark Ajersch 2004**



Library and
Archives Canada

Bibliothèque et
Archives Canada

Published Heritage
Branch

Direction du
Patrimoine de l'édition

395 Wellington Street
Ottawa ON K1A 0N4
Canada

395, rue Wellington
Ottawa ON K1A 0N4
Canada

Your file *Votre référence*
ISBN: 0-494-12575-6
Our file *Notre référence*
ISBN: 0-494-12575-6

NOTICE:

The author has granted a non-exclusive license allowing Library and Archives Canada to reproduce, publish, archive, preserve, conserve, communicate to the public by telecommunication or on the Internet, loan, distribute and sell theses worldwide, for commercial or non-commercial purposes, in microform, paper, electronic and/or any other formats.

The author retains copyright ownership and moral rights in this thesis. Neither the thesis nor substantial extracts from it may be printed or otherwise reproduced without the author's permission.

AVIS:

L'auteur a accordé une licence non exclusive permettant à la Bibliothèque et Archives Canada de reproduire, publier, archiver, sauvegarder, conserver, transmettre au public par télécommunication ou par l'Internet, prêter, distribuer et vendre des thèses partout dans le monde, à des fins commerciales ou autres, sur support microforme, papier, électronique et/ou autres formats.

L'auteur conserve la propriété du droit d'auteur et des droits moraux qui protègent cette thèse. Ni la thèse ni des extraits substantiels de celle-ci ne doivent être imprimés ou autrement reproduits sans son autorisation.

In compliance with the Canadian Privacy Act some supporting forms may have been removed from this thesis.

Conformément à la loi canadienne sur la protection de la vie privée, quelques formulaires secondaires ont été enlevés de cette thèse.

While these forms may be included in the document page count, their removal does not represent any loss of content from the thesis.

Bien que ces formulaires aient inclus dans la pagination, il n'y aura aucun contenu manquant.


Canada

Abstract

The heating, or sheet reheat, phase in thermoforming is the focus of this work. The first objective is to develop a reliable state-space model of this process for simulation analysis. The second objective is to develop a simple linear real-time in-cycle controller for the sheet reheat phase. This controller will improve part quality, decrease energy expenditures and machine wear, and optimize heating time by assuring a desired sheet temperature distribution. The final result is a reduction in production cost per part for the thermoforming industry.

A sheet model is developed from first principles, and improved through the addition of energy absorption terms. The sheet model is tested against experimental results, giving errors of less than 5°C over the entire transient temperature curve at different depths after tuning.

A linearization assumption is made, and a two-loop control algorithm is designed for the sheet surface temperatures. These temperatures are monitored using infrared sensors at different locations on the sheet. Simple PI controllers are used in real-time to monitor and maintain these IR sensors about a given step or ramp input, with great precision (less than 1°C error).

Résumé

Ce travail traite de la commande automatique en temps réel du procédé de chauffage d'une feuille de polymère pour le thermoformage. Le système de commande améliorera la qualité de la pièce formée, diminuera les coûts d'énergie et de maintien d'équipement, et optimisera le temps de chauffage en assurant une distribution de température désirée sur la feuille. Les coûts de production par pièce thermoformée seront réduits.

Un modèle de la feuille est développé à partir des lois physiques, et est amélioré par l'inclusion de l'absorption d'énergie radiante à l'intérieur de la feuille. Ce modèle est validé par des résultats expérimentaux, donnant des erreurs de simulation d'environ 5°C sur les courbes transitoires de température à plusieurs profondeurs différentes.

À partir d'une hypothèse de linéarisation, l'algorithme de commande est défini en deux boucles. Des capteurs infrarouges mesurent les températures de surface de la feuille à des endroits différents. En temps réel, un compensateur PI maintient chacune de ces mesures de température avec une excellente précision (moins de 1°C d'erreur), que la sortie désirée soit une rampe ou un échelon.

Acknowledgements

I would primarily like to thank Professor Benoit Boulet for his guidance and thought-provoking analysis, throughout the duration of my work at McGill. I greatly appreciate his technical and financial help.

I have also benefited from the experience and attitude of Ammar Haurani and Guy Gauthier. Many interesting ideas and experiments were conceived during our group discussions, and carried out with their help.

I must also acknowledge the immense contributions from CNRC-NRC IMI. All experimental material, from the thermoforming oven and plastic sheets to the FEM forming and real-time software programs, was provided by IMI, and enabled me to complete this thesis. The guidance and experience of Robert Di Raddo was especially appreciated. Benoit Lanctot and Linda Pecora were excellent tutors in the usage of the FORMSIM software. Christian de Grandpré and Marc-André Rainville were also extremely helpful with experimental setups and were always available to answer questions.

Finally, I would like to thank my family and friends for their continued support.

Table of Contents

ABSTRACT	II
RÉSUMÉ	III
ACKNOWLEDGEMENTS.....	IV
TABLE OF CONTENTS	V
LIST OF FIGURES	VIII
LIST OF TABLES	IX
CHAPTER 1 INTRODUCTION.....	- 1 -
1.1 Thesis Objective.....	- 1 -
1.1.1 Benefits to Industry	- 2 -
1.2 Literature review	- 3 -
1.2.1 Thermoforming models	- 3 -
1.2.2 IR sensors	- 5 -
1.2.3 Industrial applications of real-time control.....	- 5 -
CHAPTER 2 THERMOFORMING	- 7 -
2.1 History.....	- 7 -
2.2 Markets.....	- 9 -
2.3 Sheet gage	- 11 -
2.4 Process Description	- 11 -
2.4.1 Clamping	- 11 -
2.4.2 Heating	- 12 -
2.4.2.1 Heat Sources	- 13 -
2.4.3 Forming	- 13 -
2.4.4 Trimming.....	- 15 -
2.5 Sheet Reheat phase.....	- 15 -
2.5.1 Zoned Heating	- 17 -
CHAPTER 3 MODELING THE SHEET-HEATER SYSTEM.....	- 18 -
3.1 Heat Transfer Basics	- 18 -
3.1.1 Conduction	- 18 -
3.1.2 Convection.....	- 21 -
3.1.3 Radiation	- 23 -
3.1.3.1 Emissivity	- 23 -
3.1.3.1.1 Heating Element Emissivity Calculations	- 26 -
3.1.3.2 View Factors.....	- 30 -
3.2 Plastic Sheet Modeling – Energy Absorption within the Sheet.....	- 31 -
3.2.1 Moore Model of Plastic Sheet	- 32 -
3.2.2 Energy Absorption within the sheet	- 35 -

3.3 Complete Heater-Sheet State-Space Model	- 38 -
3.3.1 Definitions	- 38 -
3.3.2 State equations	- 39 -
3.3.3 Model Validation	- 42 -
3.3.3.1 Test setup	- 42 -
3.3.3.2 Experimental results	- 44 -
3.3.3.3 Reasons for error	- 52 -
CHAPTER 4 REAL-TIME CONTROL OF AAA THERMOFORMING OVEN ..	- 56 -
4.1 AAA Machine Overview	- 57 -
4.1.1 System Actuators and Layout	- 58 -
4.1.2 Existing Control Structure	- 60 -
4.1.2.1 Modeling the actuators	- 62 -
4.1.2.1.1 Test setup	- 63 -
4.1.2.1.2 Experimental results	- 64 -
4.1.2.2 Actuator Heating/Cooling Rate	- 67 -
4.1.3 Infrared Sensors	- 68 -
4.1.3.1 Distance to Spot Ratio	- 70 -
4.1.3.2 IR Sensor Locations	- 71 -
4.1.4 OPAL-RT RT-LAB Operating System	- 72 -
4.1.4.1 RT-LAB system structure	- 72 -
4.1.4.1.1 System Inputs	- 74 -
4.1.4.1.2 System Outputs	- 76 -
4.2 Real-Time Control of Sheet Temperatures	- 76 -
4.2.1 Linearizing the sheet reheat system	- 77 -
4.2.2 Control algorithm: multilayer control	- 81 -
4.2.3 Inner loop Control: Embedded Heating Element Temperatures	- 83 -
4.2.3.1 Hybrid Feedforward-PID controller	- 84 -
4.2.3.2 On-off or Bang-Bang Control	- 93 -
4.2.4 Outer loop Control: Sheet Surface Temperatures using IR	- 95 -
4.2.4.1 IR sensor output conditioning	- 95 -
4.2.4.2 Steady-state relationship between heaters and sheet	- 96 -
4.2.4.2.1 Insulator sheet	- 96 -
4.2.4.2.2 Test Setup	- 97 -
4.2.4.2.3 Experimental Results	- 98 -
4.2.4.2.4 Pseudo-inverse	- 100 -
4.2.4.3 Steady-State Control of Sheet Temperatures	- 100 -
4.2.4.3.1 Transient Sheet Surface Temperature Responses	- 101 -
4.2.4.3.2 Model and Controller	- 103 -
4.2.4.3.3 Real-Time implementation	- 104 -
4.2.4.4 Ramp Input Control	- 107 -
CHAPTER 5 CONCLUSION	- 111 -
5.1 Summary	- 111 -

5.2 Recommendations and Future Work..... - 112 -
CHAPTER 6 REFERENCES..... - 114 -
APPENDIX A: LIST OF POLYMERS..... - 118 -
APPENDIX B: D-M-E INSULATOR SHEET SPECIFICATIONS - 119 -
APPENDIX C: NON-LINEAR MODEL MATLAB CODE - 120 -

List of Figures

Figure 2-1: Drape forming (before and after).....	- 13 -
Figure 2-2: Vacuum or Pressure forming	- 14 -
Figure 2-3: Temperature forming window for material X [17].....	- 16 -
Figure 2-4: Temperature distribution across sheet thickness	- 16 -
Figure 3-1: Closed Oven used in heating element emissivity calculations	- 27 -
Figure 3-2: Steady-State Temperature Curves at 350C Setpoint.....	- 30 -
Figure 3-3: Radiation ray tracing between finite parallel plate elements [10]	- 30 -
Figure 3-4: Plastic Sheet Discretization	- 32 -
Figure 3-5: Start of Heating Curves for 12mm sheet at 280C.....	- 34 -
Figure 3-6: Test Setup for Thick Sheet Experiments	- 43 -
Figure 3-7: 280C Experimental Temperature Curves	- 45 -
Figure 3-8: 280C Simulation Model Temperature Curves	- 46 -
Figure 3-9: 280C Simulation Error (vs. Experimental Data)	- 46 -
Figure 3-10: 320C Experimental Temperature Curves	- 47 -
Figure 3-11: 320C Simulated Model Temperature Curves	- 48 -
Figure 3-12: 320C Simulation Error (vs. Experimental Data)	- 48 -
Figure 3-13: 420C Experimental Temperature Curves	- 49 -
Figure 3-14: 420C Simulated Model Temperature Curves	- 50 -
Figure 3-15: 420C Simulation Error (vs. Experimental Data)	- 50 -
Figure 3-16: IR temperature measurement of Heating Element Surface (setpoint 300C).....	- 54 -
Figure 3-17: LI01 data line from IR Camera picture above (setpoint 300C)	- 54 -
Figure 3-18: Histogram showing temperature distribution along line LI01	- 55 -
Figure 4-1: AAA Thermoforming machine (front view)	- 58 -
Figure 4-2: Tempco 650W Heating element	- 59 -
Figure 4-3: Lower Heating tray.....	- 59 -
Figure 4-4: Top view of AAA Oven	- 60 -
Figure 4-5: PID control panel (for all 12 heater zones).....	- 61 -
Figure 4-6: PID Control Loop	- 62 -
Figure 4-7: B2 Embedded Thermocouple Temperature – 10% Duty Cycle	- 64 -
Figure 4-8: Closed-Loop PID model vs. Actual data	- 66 -
Figure 4-9: B2 Heating (100%) and Cooling (free) Curves	- 67 -
Figure 4-10: Raytek Thermalert® MIC™ IR sensor with cooling jacket	- 70 -
Figure 4-11: Examples of different $D : S$ ratios.....	- 70 -
Figure 4-12: Top view of AAA oven with IR sensors	- 71 -
Figure 4-13: RT-LAB Hardware Package.....	- 73 -
Figure 4-14: Thermocouple signal conditioners from Analog Devices (3B37, 3B47).....	- 75 -
Figure 4-15: Linearization function about 160°C setpoint (for HDPE)	- 79 -
Figure 4-16: Percent error for Linearization over entire HDPE forming range (140-180°C)	- 79 -
Figure 4-17: Linearization function for 350C setpoint.....	- 80 -
Figure 4-18: Percent Error for linearization over heating element active range (300-400°C)	- 81 -
Figure 4-19: Inner Loop Heating Element Control Schematic.....	- 82 -
Figure 4-20: Outer Loop Controller Block Diagram.....	- 82 -
Figure 4-21: Signal input from Analog Devices 3B37 Signal Conditioner.....	- 84 -
Figure 4-22: Signal input from Analog Devices 3B47 Signal Conditioner.....	- 84 -
Figure 4-23: Filtered and Unfiltered embedded thermocouple signal.....	- 86 -
Figure 4-24: Signal delay due to low pass filter.....	- 87 -
Figure 4-25: Hybrid Feedforward PID controller.....	- 88 -
Figure 4-26: Square Wave Function	- 89 -
Figure 4-27: Embedded Thermocouple reaction to various PID setpoints (zone B1).....	- 90 -
Figure 4-28: Cross section of ceramic heating element.....	- 91 -
Figure 4-29: Ceramic Heating element Conduction Delay (Heating Zone B2)	- 92 -

Figure 4-30: Block Diagram of Bang-Bang Inner Loop Controller	- 93 -
Figure 4-31: Conduction Delay Oscillations for Bang-Bang Controller (zone B1)	- 94 -
Figure 4-32: Signal conditioning of the IR output signal	- 96 -
Figure 4-33: Transient Sheet Surface Temperature Responses	- 101 -
Figure 4-34: First-Order fit of IR sensor responses to 150°C step on all zones	- 102 -
Figure 4-35: Simulink Model of Sheet/Heater system	- 103 -
Figure 4-36: Simulated PI Control response to step I/P of [175 150 125 100]	- 104 -
Figure 4-37: Open-loop Control of IR Measurements (nominal setpoint)	- 105 -
Figure 4-38: Closed-Loop Control of IR Measurements (nominal setpoint)	- 106 -
Figure 4-39: Embedded Thermocouple Heater Temperatures (all zones)	- 107 -
Figure 4-40: Velocity Feedforward PI controller for Ramp input	- 108 -
Figure 4-41: IRT1 Sensor Response to Ramp input	- 109 -
Figure 4-42: IRT1 Sensor Error for Ramp Input	- 109 -
Figure 4-43: Heating Element Response to Ramp Input	- 110 -

List of Tables

Table 2-1: US Polymers Converted via Thermoforming	- 9 -
Table 2-2: Major Thermoforming Industries and their products [10]	- 10 -
Table 3-1: Material Thermal Conductivity Ranges	- 20 -
Table 3-2: Range in Values for Convection Heat Transfer Coefficient [10]	- 22 -
Table 3-3: Emissivity of certain materials [18]	- 25 -
Table 3-4: Experimental Heating Element Emissivity Results	- 29 -
Table 3-5: Tuned Simulation Parameters for 280C, 320C and 420C tests	- 51 -
Table 4-1: B2 parameters for several duty cycles	- 65 -
Table 4-2: Heating and Cooling Rates for zone B2	- 68 -
Table 4-3: Open-Loop Insulator Sheet Step testing results	- 98 -

Chapter 1 Introduction

1.1 Thesis Objective

Thermoforming is an industrial process in which plastic sheets are heated and then formed into useful parts. It can be divided into three distinct phases: heating, forming and cooling. The sheet is heated in an oven until it becomes pliable. The softened sheet is then formed over the mold and cooled until it hardens. A more detailed description of the thermoforming process is found in the following chapter.

The heating, or sheet reheat, phase is the focus of this work. The first objective is to develop a reliable state-space model of this process for simulation analysis. The second objective is to develop a simple linear real-time in-cycle controller for the sheet reheat phase. There are two different control strategies for this type of system, in-cycle and cycle-to-cycle. A cycle-to-cycle controller by definition only takes an action after the whole cycle has been completed, i.e., the part has been formed, in order to improve the next part. The in-cycle controller, however, reacts while the part is being heated, so that a desired sheet temperature profile can be attained in an optimal heating time.

Each of these objectives has separate benefits. The non-linear state-space model can be used off-line in order to determine the optimal system parameters. Once the system parameters have been found, the desired forming time and temperature distribution profile for a typical part can be quickly estimated from the model output. The temperature distribution can then be achieved using the simple real-time in-cycle controller, ensuring a satisfactorily formed part at the machine output.

At present, the industry standard is an open-loop control system, where the machine operator “tweaks” the oven temperatures until a satisfactory part is made. At this point these settings are maintained until machine drift or other factors cause the final parts to become unsatisfactory, whereupon the operator will readjust the settings. Using the model, the operator can first determine the machine parameters, and obtain a temperature distribution, either across the sheet surface, or even within the sheet. Then the operator will only have to input this desired temperature profile for the final part. The in-cycle controller will then determine the oven temperature settings that will reach this profile in the shortest possible time.

1.1.1 Benefits to Industry

The development of such a controller will benefit the thermoforming industry in several different ways.

The quality of the part will improve, on average, due to the better energy distribution within the sheet. Also, this even temperature distribution can lead to less rejected parts, a major benefit to the thermoforming industries that make the larger, higher-end, more expensive parts (gas tanks, for instance). The material cost per part will then decrease.

Similarly, the time needed to produce a sheet with the desired temperature distribution will be optimized. Using the sheet reheat model, the optimal heating trajectories can be determined, shortening the heating time, and increasing the number of parts that can be produced per shift and, consequently, the machine throughput as well.

Other benefits to industry derived from this controller include the minimization of the energy input to the thermoforming oven. By controlling the energy entering the sheet, an

optimal oven temperature setting can be determined in order to lower the heating costs. The machine itself may also require less maintenance and repair work. Heating elements become less efficient as they age, and the controller will compensate for this loss of efficiency by directing the adjoining elements to heat more. The end result of all of these benefits is a decrease in production cost per part, an important savings for the thermoforming industry.

1.2 Literature review

Interesting technological advances have been put forward in most polymer processes, especially extrusion blow molding and injection molding. Less work has been done in the thermoforming industry, but a large number of interesting articles have been published in the last five years. Most of these are related to the development of sheet models during the reheat phase, but some work has also been done modeling the heating elements as well. Only one paper was found that discussed cycle-to-cycle control in thermoforming. Michaeli and van Marwick [19] proposed a two-level controller to monitor the distribution of the wall thickness in thermoformed parts, and suggested two methods of measuring this property on-line, either using ultrasound sensors, or by triangulation laser.

1.2.1 Thermoforming models

Smaller sheet models can be used on-line to determine the time-varying temperatures within the sheet as it is being heated. The initial work in modeling the sheet reheat phase of thermoforming for thick sheets was done by Moore et al. [16,17], who proposed a discretization of the sheet across its thickness. Moore developed simulated H-infinity and

model-predictive in-cycle controllers for this sheet model as well. Duarte and Covas [4,5] investigated the inverse heating problem for a roll-fed (or thin sheet) thermoforming machine. They developed another model determining ideal heating element temperatures to give a uniform sheet surface temperature. This model included energy absorption within the sheet according to the Beer-Lambert law. Two differing solutions were proposed, and a sensitivity analysis involving parameter perturbation was performed. Monteix et al. [6] also developed a control-volume method for determining radiant heat transfer within the plastic sheet. Their model also included one-dimensional energy absorption due to Beer-Lambert Law.

Larger finite-element models (FEM) of the thermoforming process are used in simulation in order to pre-determine optimal operating conditions for precise sheet thickness distribution during thermoforming. The first such computer-aided model was developed by Throne [1], who investigated the effects of zoned heating and changes in heater-sheet distance on the sheet surface temperatures. Yousefi et al. [3] improved FEM modeling of reheat phase in thermoforming due to uncertainty treatment of several machine parameters. DiRaddo et al. [23] examined the effects of machine drift by comparing experimental results to the FEM model. Other FEM models include those developed by Sala et al. [20], a numerical solution based on physical testing of polymer parameters and tested experimentally against the forming of a low-temperature refrigerator cell.

The sheet itself is not the only aspect of the thermoforming oven that has been modeled. Much work has been done discussing the heating elements that provide energy to the sheet. Schmidt et al. [8] characterized the spectral responses of several different types of heating elements, discovering that halogen heating elements were more efficient than

their ceramic or quartz counterparts. Petterson and Stenstrom [22] developed a steady-state and transient model of an electric IR heater, as applied to a paper dryer (for the pulp and paper industry).

1.2.2 IR sensors

Several researchers investigated the measurement validity and accuracy of infrared temperature sensors, similar to those used to measure sheet surface temperatures inside a thermoforming oven. Lappin and Martin [2] first discussed the implementation of these sensors on a thermoforming machine, as well as potential calibration and noise issues. Bugbee et al. [7] characterized three different types of IR sensors, according to calibration and sensor body temperature errors. A new approach to the calibration of IR thermometers was proposed and prototyped by Baker et al. [9]

1.2.3 Industrial applications of real-time control

Real-time process control has not yet been applied in thermoforming. However, in other industries, much work has been done to develop models that will achieve this objective. Safarty et al. [21] applied advanced process control to the semi-conductor industry, developing a method of wafer-to-wafer testing to improve throughput and flexibility of the manufacturing process. Using trained neural networks and machine vision algorithms, Peng et al. [25] developed an intelligent approach for optimizing robot arc welding in real-time. Finally, Hossain and Suyut [24] successfully integrated a dynamic statistical process control model with a real-time industrial process.

In Chapter 2, thermoforming is described in more detail. The sheet model is developed from first principles and then tested against experimental results in Chapter 3. Chapter 4 includes a description of the experimental real-time setup, as well as the first real-time in-cycle sheet surface temperature controllers developed for sheet reheat. The final chapter contains a brief summary, and offers potential model-based real-time control solutions combining the twin objectives of this work: the absorption model from Chapter 3 and the real-time controllers from Chapter 4.

Chapter 2 Thermoforming

Thermoforming is a generic term describing the many techniques for producing useful plastic parts from a flat sheet. In its simplest form, thermoforming is the draping of a heated (and softened) plastic sheet over a mold.

This chapter first gives a brief history of thermoforming, before listing examples of thermoformed parts. All phases of the process are then described in small detail, with special emphasis on the sheet reheat phase and zoned heating as they relate to the development of an in-cycle controller.

2.1 History

Thermoforming, in one form or another, has been around for many centuries. The earliest civilizations in Egypt and Micronesia heated tortoise shells in hot oil. The keratin within the shell was then cooled and shaped to form food containers and bowls. In the Americas, the natural cellulose in tree bark was heated in hot water, to produce boats and canoes [10].

J.W. Hyatt developed the first commercially viable plastic material, called “celluloid” in the mid-19th century. Most products in this age were made by drape-forming softened plastic sheets. Sharps piano keys for example were drape formed over small wooden blocks.

The modern age of thermoforming began approximately at the time of the Second World War. Two major developments occurred concurrently. The first was material-based: new resins (PVC – polyvinyl chloride, PMMA – polymethyl methacrylate to name but two)

were developed for commercialization. The second was technology-based: the invention of the screw extruder and the roll-fed thermoformer enabled continuous forming. After the war, thermoforming became the primary process for the packaging industry to the extent that the thermoformed package was the significant packaging development of the 1950s [10].

As time progressed, larger thermoformed pieces became more commonplace. Shower stalls and refrigerator door liners, as well as large plastic signs for interstate fast food franchises were all thermoformed products developed in the 1970s. Even automobile bodies were being made using the thermoforming process. The packaging industry continued to grow as well, with food containers now made of foam PS (polystyrene).

Today, thermoforming is regarded as the area of polymer processing with the greatest growth potential, due to its high degree of craftsmanship and experience. Process control and material advances will allow more complex parts to be made. Twin-sheet thermoforming, for instance, is the process used to make automobile gas tanks that meet the strict PZEV (Partial Zero Emissions Vehicle) mandates adopted in California [17]. The next developments will be to attempt to curb heating costs, and reduce the amount of waste material.

2.2 Markets

Table 2-1 below gives an idea of the amount of thermoformable material that is consumed in the United States, as well as the annual growth rate [10].

Table 2-1: US Polymers Converted via Thermoforming

Polymer	<i>Amount Thermoformed (Mkg)</i>				<i>Annual Growth</i>
	1977	1983-4	1992	1995	1984-1992 (%)
ABS	70	127	202	240	6
PMMA	36	38	42	50	2
HDPE	10	26	59	87	11
PP	8	22	72	115	16
PS	392	480	640	720	4
Total	544	782	1181	1450	5

The list of polymer names can be found in Appendix A: List of Polymers . Thermoforming is then still a growing industry, its volume of production increasing at a rate of approximately 5% per year. The newer polymers such as PP (polypropylene) and PET (polyethylene terephthalate) are experiencing faster annual growth than the established polymers like PS and PMMA.

Table 2-2 on the following page lists the major thermoforming industries and their products.

Table 2-2: Major Thermoforming Industries and their products [10]

<i>Industry</i>	<i>Product</i>
Packaging	<ul style="list-style-type: none"> • Blister packs, bubble packs • Electronics (A/V cassette holders) • Foams (meat, poultry trays) • Egg cartons • Portion (medical unit dose) • Form fill seal (jelly, crackers, nuts, bolts) • Convenience (carry-out)
Vehicular	<ul style="list-style-type: none"> • Automotive door innerliners • Automotive instrument panel skins • Aircraft cabin wall panels, overhead compartment doors • Snowmobile, ATV shrouds, windshields • Tractor shrouds • Truck cab door fascia, instrument cluster fascia • RV interior components
Industrial	<ul style="list-style-type: none"> • Tote bins • Pallets, single or double deck • Parts or transport trays • Equipment cases
Building	<ul style="list-style-type: none"> • Shutters, window fascia • Skylights • Exterior lighting shrouds • Storage modules • Bath and shower surrounds
Other	<ul style="list-style-type: none"> • Exterior and interior advertising signs • Swimming and wading pools • Luggage • Golf club cases • Boat hulls, surfboards

2.3 Sheet gage

All the products listed above are clearly not the same size. The individual peanut butter package is not made from the same sheet thickness as the refrigerator door liner. The sheet gage, or thickness, splits the thermoforming process into two broad categories: thin-gage and heavy-gage.

Thin-gage thermoforming implies a sheet thickness of less than 1.5mm. This can be further subdivided into film forming, with sheet thicknesses less than 0.25mm, and thin-sheet forming, where the thicknesses are between 0.25mm and 1.5mm.

Heavy-gage thermoforming implies a sheet thickness greater than 3mm. Heavy sheet forming is classified by sheet thicknesses between 3 and 10mm, and plate forming by sheet thicknesses greater than 10mm.

2.4 Process Description

The thermoforming process can be split into 5 parts: clamping, heating, forming, cooling and trimming. A brief description of each phase will be given, with respect to the gage of the sheet.

2.4.1 Clamping

Clamping is the method used to hold the sheet in place during the other 4 phases. It varies depending on the sheet thickness. For thin-gage thermoforming, the sheets are supplied to the machine in the form of rolls. These roll-fed machines are primarily used in the packaging industry. The clamping is done by parallel continuous loop pin-chains that

pierce the sheet at 25mm intervals approximately 25mm from the sheet edge.

For heavy-gage thermoforming, the clamping mechanism is a clamp frame. Since heavy-gage machines only form one sheet at a time, this mechanism is much simpler than the thin-gage transport chain. The sheet is placed between two identical frames, one stationary, and one hinged, and then anchored in place for heating, forming and trimming.

2.4.2 Heating

The sheet heating phase is the focus of this thesis. As stated above, the objective is to control the heating phase such that the sheet temperature distribution meets the desired specifications in the smallest amount of time possible. Section 2.5 will treat this in more detail.

In general, there are three heat transfer modes used to increase the sheet temperature: conduction, convection and radiation. Conduction is heating by contact, meaning the sheet is in direct contact with the heating medium. Convection is heating by hot air, and radiation is heating by infrared heat from a heat source. These are all explained in detail in Chapter 3.

Thin-gage roll-fed sheets are primarily heated by passing the sheet between banks of infrared radiant heaters. However, there are two primary heat mechanisms for heavy-gage sheet: internal conduction and radiation. The exterior of the thick sheet is heated by radiation, but not excessively, as this could damage the sheet surface. The sheet heating time is partly determined by the conduction of heat from the surface to the interior, and

by the absorption of radiant energy inside the sheet.

2.4.2.1 Heat Sources

There are several different types of heat sources within the thermoforming oven. They range from simple nickel-chrome heating wires to calrods, from ceramic bricks or tiles to quartz plates or halogen bulbs. Each of these has its advantages and disadvantages. Quartz can be turned on and off like lightbulbs, but are quite fragile and break often, whereas ceramics do not break as often but take a long time to reach their temperature setpoints.

2.4.3 Forming

The forming mechanisms for thin and heavy-gage sheets are very similar. There are two major types: drape forming, and vacuum forming [Throne].

In drape forming, the heated plastic sheet is stretched over a positive or male mold as in Figure 2-1 below.

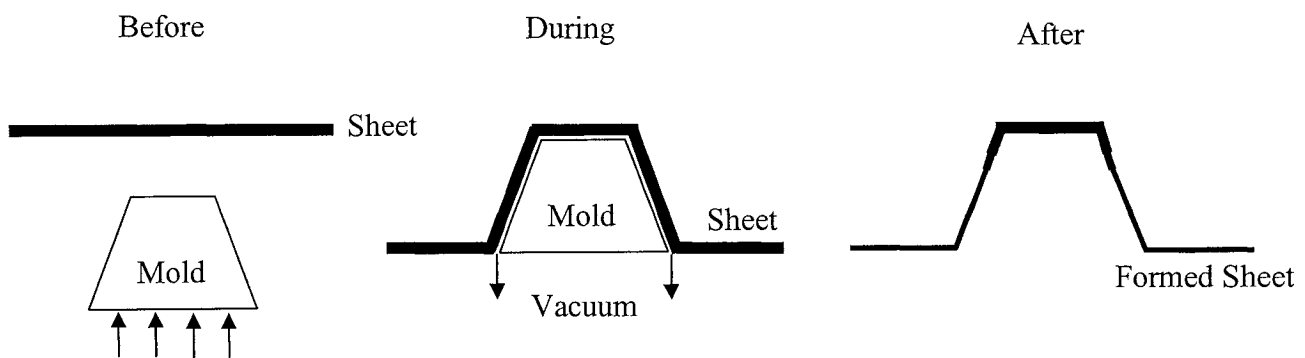


Figure 2-1: Drape forming (before and after)

Either the mold is raised to the sheet, or the sheet is draped over the mold. The air

between the mold and sheet is evacuated via the vacuum. The resulting formed part has a thick rim, gradually thinning sidewalls and is thinnest along the edges.

Another type of forming occurs when the heated sheet is sealed against the female mold or cavity by vacuum or air pressure as in Figure 2-2 below. Miniature holes in the cavity ensure a solid seal while the part is forming. Contrary to forming with male molds, the final part has thicker edges and is thinnest in the bottom corners and along the rim.

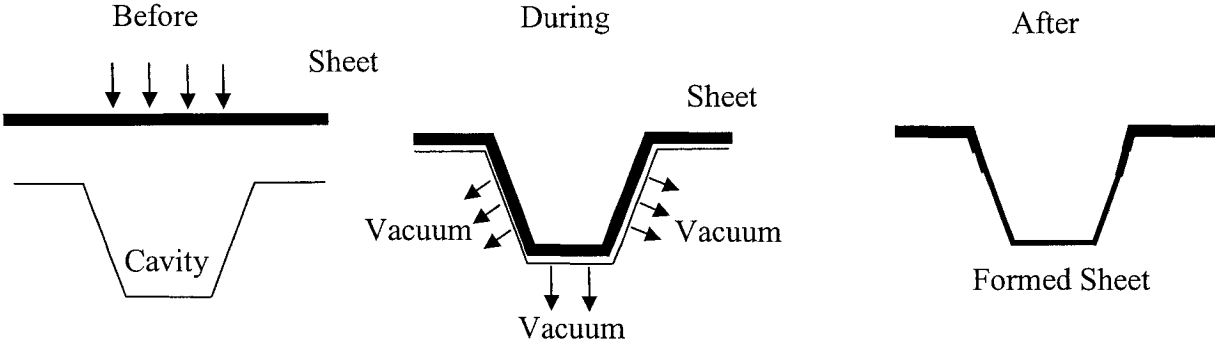


Figure 2-2: Vacuum or Pressure forming

These are the simplest methods of sheet forming, but there are more complicated types. Certain heavy-gage parts require a second step in the forming phase in order to get the right thickness distribution. These second steps include billow prestretching, where air is blown underneath the heated sheet to create a large bubble. This bubble will ensure that the sheet is properly stretched before the vacuum is applied. Another method of prestretching the sheet is to use a plug assist. The plug is the smaller male counterpart to the vacuum forming female mold, used to stretch the heated sheet to every section of the female mold.

2.4.4 Trimming

Trimming eliminates all plastic pieces not needed for the final part. These pieces are then re-ground and re-formed into new sheets, to make more parts. Certain products can specify a maximum amount of regrind material within their sheets.

The thin-gage sheet is trimmed while still on the production line, generally by a hydromechanical trimming device, like a camelback or humpback trimmer.

The heavy-gage sheet is generally trimmed on a trimming fixture, not on the forming machine. The trimming can be done manually with a hook-knife, router, or band-saw, or automatically with a water jet or laser, or with a multi-axis trimming fixture. [10]

2.5 Sheet Reheat phase

The sheet reheat, or heating, phase affects all subsequent steps in the forming process. The two factors that affect sheet reheat are the heating element temperatures and the sheet heating time. Every material has a temperature window in which forming is possible. Below the minimum temperature, the material is not fully molten and cracks will occur during forming. Above the maximum temperature, the material will scorch or burn on the surface, resulting in a rejected part. The objective of sheet reheat control is to heat the centerline temperature within the sheet to the minimum forming temperature as fast as possible, while ensuring that the surface temperature remains below the maximum forming temperature. Figure 2-3 below will clarify this statement.

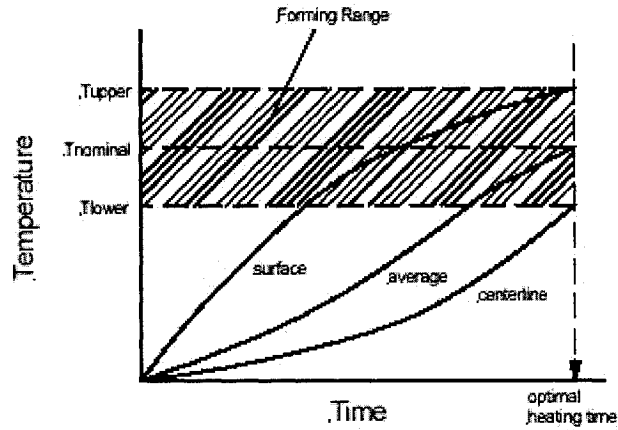


Figure 2-3: Temperature forming window for material X [17]

The forming window in Figure 2-3 occurs between T_{lower} and T_{upper} . The optimal heating time is the shortest amount of time the system will take to heat the centerline temperature of the sheet to T_{lower} .

The temperatures will of course vary across the thickness of the sheet. The smaller these temperature gradients are, the easier the part will be to mold. Figure 2-4 shows the variations of temperature within the sheet, as the heating time increases.

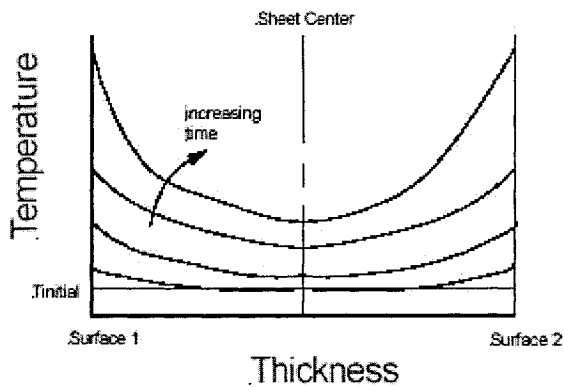


Figure 2-4: Temperature distribution across sheet thickness

2.5.1 Zoned Heating

If the oven was uniformly held at a given temperature, “hot” spots would occur. Certain sheet zones would be receive more energy or heat from the heating elements, and therefore their temperatures would increase much faster than their neighbors, due to a phenomenon called the “view factor” (see section 3.1.3.2). For this reason, modern thermoforming ovens are divided into several zones. The purpose of this zoning is to ensure some control over the temperatures at certain locations on the sheet surface. Some parts require temperature uniformity across the surface, while others might require hotter spots at certain locations to ensure that the final part thickness at that spot is as desired. However, finding the correct heating element temperatures that produce the correct sheet temperature distribution is quite difficult. Also variances in material properties (even within the same batch of material) can cause temperature variations on the sheet surface, since the sheets might not all receive energy at the same rate.

For these reasons, in-cycle control is needed. It will maintain the desired temperature distribution (“hot spots” or uniform), while minimizing the heating time, and consequently will increase the throughput of the machine and eliminate rejected parts.

The purpose of this section was to provide the reader with some background information about thermoforming in general, before moving on to the modeling and real-time control sections. A special focus was placed upon the sheet reheat phase, as any in-cycle control effort will originate there. If desired, further information can be obtained from [10].

Chapter 3 Modeling the Sheet-Heater System

The first task to be completed in controlling any system is to build a proper model. In this particular case, a model of the physical interactions between the heating element and the plastic sheet inside the oven must be developed. The sheet reheat phase of the thermoforming process can be modeled by a combination of the three mechanisms of heat transfer: conduction, convection, and radiation, which are described below in detail.

Secondly, the sheet model will be developed using previous work done by Moore [16,17], who proposed the discretization of the plastic sheet across its thickness. However, this model will incorporate the absorption of energy within the sheet as it is heated.

Thirdly, a state-space description of the heating element-plastic sheet system will be developed, and tested against experimental results.

3.1 Heat Transfer Basics

The first section of this chapter presents the basic modes of heat transfer: conduction, convection and radiation, as they relate individually to thermoforming.

3.1.1 Conduction

Conduction is defined as the mode of heat transfer through direct physical contact. Due to the translational and vibrational motion of the molecules in a material, energy is transmitted through the material. If there is a temperature gradient in the material, then energy will be transferred from the area at higher temperature to the area at lower

temperature. This net transfer of energy can also be labeled diffusion of energy. An example of conduction is the gradual warming of the end of a metal spoon placed in cup of hot coffee.

Conduction is governed by Fourier's Law [15].

$$q_x = -k \frac{\partial T}{\partial x} \quad (3.1)$$

Here the heat flux q_x (W/m^2) is the heat transfer rate in the x direction per unit area perpendicular to the direction of heat transfer. The heat flux is proportional to the temperature gradient, $\partial T/\partial x$, in this direction. The thermal conductivity constant k ($\text{W}/\text{m} \cdot \text{K}$) is a characteristic of the material and does not depend on temperature. The minus sign maintains the convention of energy being transferred from higher temperature to lower temperature.

Table 3-1 gives typical values for thermal conductivity in different materials:

Table 3-1: Material Thermal Conductivity Ranges

Material	Conductivity
Aluminum alloy	190
Stainless Steel	12-27
Iron	13-40
Nickel	60
HDPE	0.3-2.5
Nylon	0.2-1.15
Polystyrene	0.1-0.2
Polypropylene	0.1-0.3
Ceramic/metallic	13-21
Potting/casting ceramic	5-36
Machinable ceramic	0.41-31
Glass	0.06-2
Carbon	24
Wood	0.05-0.17
Diamond	2000

Using Fourier's law above, the general three-dimensional heat conduction equation can be derived [15]:

$$\frac{\partial}{\partial x} \left(k \frac{\partial T}{\partial x} \right) + \frac{\partial}{\partial y} \left(k \frac{\partial T}{\partial y} \right) + \frac{\partial}{\partial z} \left(k \frac{\partial T}{\partial z} \right) + q_{\text{int}} = \rho C \frac{\partial T}{\partial t} \quad (3.2)$$

For constant thermal conductivity k , the equation becomes:

$$\frac{\partial^2 T}{\partial x^2} + \frac{\partial^2 T}{\partial y^2} + \frac{\partial^2 T}{\partial z^2} + \frac{q_{\text{int}}}{k} = \frac{1}{\alpha} \frac{\partial T}{\partial t} \quad (3.3)$$

Here, ρ represents the density of the material (kg/m^3), and C , the heat capacity ($J/(kg \cdot K)$). The thermal diffusivity, $\alpha = k/\rho C$, indicates the rate at which the heat will diffuse through the material. q_{int} represents the internal energy generated within the body.

An initial assumption was made in modeling the sheet reheat process: due to the relatively small thickness (gage) of the plastic sheet as compared to the distance from the heating element, the conduction of energy through the sheet would only occur in one direction, in the direction of heat transfer. In other words, there would be no lateral conduction of energy within the sheet. In this case, the one dimensional Fourier's Law can be applied as above and integrated into the model.

3.1.2 Convection

Convection heat transfer occurs between a surface and a moving or stationary fluid when they are at different temperatures. More specifically, convection heat transfer is due to cumulative motion of the fluid molecules that are moving in large numbers across the surface of the solid. There are two forms of convection heat transfer, classified according to the nature of the flow. The first is forced convection, when the fluid is caused by an external source, like a fan or a blower. The second is free or natural convection, which is simply due to the differences in fluid density, causing buoyancy forces to act upon the fluid.

Convection is governed by Newton's law of cooling. [18]

$$q = h(T_s - T_\infty) \quad (3.4)$$

Here q is the convective heat flux per unit area (W/m^2), h is the convection coefficient ($W/(m^2 \cdot K)$), T_s is the surface temperature of the solid, and T_∞ , the fluid temperature. The sign convention indicates a positive heat transfer if the surface temperature is greater than the fluid temperature, and negative in the opposite case.

Table 3-2 below shows typical values for the convection coefficient h for different fluids:

Table 3-2: Range in Values for Convection Heat Transfer Coefficient [10]

Fluid	Conventional Heat Transfer Coefficient h ($W/(m^2 \cdot K)$)
Quiescent Air	5-10
Air moved with fans	10-30
Air moved with blowers	30-100
Water spray	300-900
Oil in pipes	300-1800
Water in pipes	600-6000

For sheet reheat, convection occurs between the sheet surface and the air inside the oven. Generally speaking, during the heating of the sheet, fans are not used to blow air inside the oven. Therefore, the value of h typically used is of the order of quiescent air, or 5-10 ($W/(m^2 \cdot K)$).

3.1.3 Radiation

Thermal radiation is the third mode of heat transfer. Energy is radiated from a body due to its surface temperature along the intermediate portion of the electromagnetic spectrum. Thermal radiation occurs between 0.1 and 100 μm , encompassing all of the visible and IR regions, as well as a portion of the UV range [18]. Note that certain properties examined in this section (emissivity, transmittivity, etc.) are wavelength-dependent. To get the total emissivity, for instance, the wavelength dependent value for the emissivity needs to be integrated over the entire wavelength range (from 0.1-100 μm). For the remainder of this thesis, only total values will be considered.

An ideal radiator, or blackbody, emits thermal energy at the following rate, according to the Stefan-Boltzmann law [18]:

$$q_b = \sigma T_s^4 \quad (3.5)$$

Here, q_b is the energy flux emitted per unit area by the blackbody (W/m^2), σ is the Stefan-Boltzmann constant ($\sigma = 5.669 \times 10^{-8} \text{ W}/(\text{m}^2 \cdot \text{K}^4)$), and T_s is the surface temperature of the blackbody.

3.1.3.1 Emissivity

A blackbody is so named because materials that obey the Stefan-Boltzmann law do not reflect any radiation. In other words, all radiation that strikes the surface of the blackbody is absorbed. However, most bodies occurring in nature obey the following relation [15]:

$$1 = \eta + \tau + \alpha \quad (3.6)$$

If, in Equation (3.6) above, the total energy incident onto the surface of a body is 1, then the reflectivity η is the fraction that is reflected, the absorptivity α is the fraction absorbed, and the transmittivity τ is the fraction transmitted. For most solid materials, τ is considered to be zero, as thermal radiation is not transmitted through the body [15]. This type of body is called a gray body.

To define total emissivity (since emissivity alone depends on wavelength) of a body, assume two bodies of exactly the same size, one black and one gray, are at thermal equilibrium, meaning each is receiving exactly as much energy as it is emitting. For the gray body, the equilibrium equation is:

$$q_g A = q_i A \alpha \quad (3.7)$$

q_i is the heat flux striking the surface area, A , of the body, and α is its absorptivity. q_g is the power emitted by the gray body. For the black body, the equilibrium equation becomes:

$$q_b A = q_i A (1) \quad (3.8)$$

Here, q_b represents the power emitted by the black body. The ratio of the emissive power of the gray body to that of a black body, at the same temperature is defined as the emissivity of the body [15]:

$$\varepsilon = \frac{q_g}{q_b} = \alpha \quad (3.9)$$

Then the total emissive power emitted by a gray body, using the Stefan-Boltzmann law, is:

$$q_g = \varepsilon \sigma T_s^4 \quad (3.10)$$

Emissivity values vary from 0 to 1, depending on the smoothness and regularity of the body surface. In Table 3-3 below, it can be noted that a more polished surface has a lower emissivity than an oxidized, rough surface, especially for metals.

Table 3-3: Emissivity of certain materials [18]

Material	Emissivity
Polished metals	0.03-0.13
Metals, as received	0.1-0.4
Oxidized Metals	0.3-0.7
Oxides, Ceramics	0.4-0.8
Carbon, Graphites	0.75-0.9
Minerals, Glasses	0.8-0.95
Plastics	0.9-0.95
Special paints, Anodized finishes	0.9-0.97

The net radiative heat flux between an emitter (heating element) and a receiver (plastic sheet) is given by the following equation [10]:

$$q_{rad} = \sigma \varepsilon_{eff} (T_h^4 - T_s^4) \quad (3.11)$$

q_{rad} is the net radiative heat flux per unit area, σ is the Stefan-Boltzmann constant, T_h is the surface temperature of the heating element, and T_s is the surface temperature of the sheet. ε_{eff} is called the gray body correction factor and is defined below [10]:

$$\varepsilon_{eff} = \left[\frac{1}{\varepsilon_h} + \frac{1}{\varepsilon_s} - 1 \right]^{-1} \quad (3.12)$$

ε_h is the emissivity of the heating element, and ε_s is the emissivity of the plastic sheet. From equation (3.12) above, it can be assumed that the emissivity of the plastic sheet is 0.95. However to find the emissivity of the ceramic heating element used in the thermoforming oven, some experimentation was needed. The section below describes the methodology used to determine an experimental emissivity value for the heating element.

3.1.3.1.1 Heating Element Emissivity Calculations

Test setup

Using a closed oven, temperature measurements (both surface and embedded) of a black body and the heating element in question will be taken. The closed oven is chosen so that each of the bodies in question can receive an equal amount of energy; in other words, there are no energy losses due to convection. The oven used in the experiment is shown in Figure 3-1.

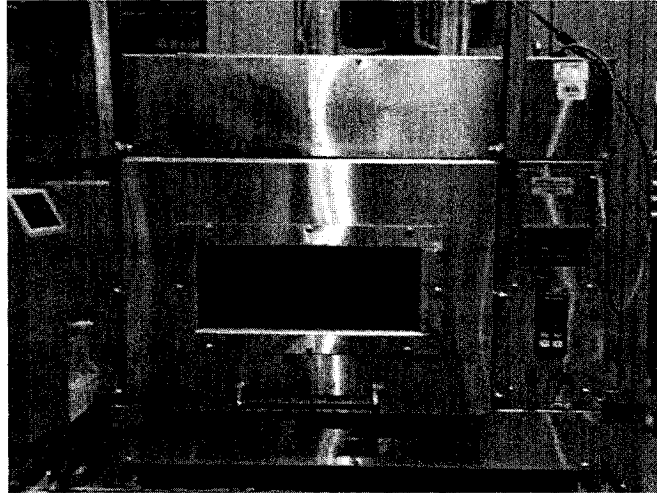


Figure 3-1: Closed Oven used in heating element emissivity calculations

At steady-state within the closed oven, any body will receive as much energy as it emits. Therefore, the portion of energy q_{rad} emitted by the oven and received by the body is equivalent to the energy emitted by that same body, whether the body is black or grey. The radiative heat rate equation can then be used to determine the emissivity of the heating element:

$$q_{rad} = \sigma \epsilon_b F_b T_b^4 \quad (3.13)$$

Here σ is the Stefan-Boltzmann constant, ϵ_b is the emissivity of the body, F_b is the view factor (see Section 3.1.3.2 for a description of view factors), and T_b is the temperature of the body.

The “black body” in this case is a small rectangular block of polished and sanded aluminum (87mm x 73mm x 12mm) that has been painted black with thermal paint. A small hole has been drilled 18mm into the block in order to insert the thermocouple which will be measuring the embedded “black body” temperature. The importance of using the black body is to ensure an emissivity of 1, since all energy should be absorbed

by the black body.

Assuming that the radiant energy received by both the black body and the heating element is the same, the following simplifications to equation (3.13) above can be made:

$$\begin{aligned} q_{rad}(BB) &= q_{rad}(heater) \\ \sigma \epsilon_{BB} F_{BB} T_{BB}^4 &= \sigma \epsilon_h F_h T_h^4 \end{aligned} \quad (3.14)$$

As both bodies are very close together, and are small when compared to the oven, then the ratio of their view factors becomes the ratio of their surface areas.

$$\sigma \epsilon_{BB} A_{BB} T_{BB}^4 = \sigma \epsilon_h A_h T_h^4 \quad (3.15)$$

The emissivity of the black body is 1 by definition. Also, σ can be eliminated from both sides. Finally, the equation for the emissivity of the heater can be obtained:

$$\epsilon_h = \frac{A_{BB} T_{BB}^4}{A_h T_h^4} \quad (3.16)$$

So there are four factors that affect the emissivity of the heating element: the respective surface areas of the black body and the heating element, as well as their respective temperatures, measured in Kelvins.

The surface area of the rectangular black body was measured to be 16542 mm². Also, the surface area of the heating element was estimated to be 34800mm², assuming that the heater was rectangular, with the following dimensions: 240mm long, 60mm wide and 10mm thick.

Experimental results

Tests were performed at 150°C, 250°C, 350°C, and 450°C in order to determine whether the emissivity of the heating element depends on the ambient temperature. If so, then this

would have to be incorporated into the model.

Table 3-4 below shows the experimental results, at several different oven temperatures (all values are steady-state temperatures (in °C)):

Table 3-4: Experimental Heating Element Emissivity Results

Oven Setting	Test #	Air Temp	Emb Black Body	Emb Heater	Emissivity
150C	1	95.6/103	106	109	0.4605
250C	1	178	190.5	193.5	0.4633
350C	1	289.3	300.2	299.6	0.4773
450C	1	362	380	379.5	0.4768

Initial startup temperature data were obtained as well, for the 250°C, 350°C, and 450°C cases, until the oven stabilized at the desired setpoint. However, each test did take several hours to attain a steady state temperature, at which point the steady-state data was collected.

Figure 3-2 below shows the steady-state temperatures for the 350°C test. The measurements were taken using type-K thermocouples, which have an operating range of 0-500°C. The data was collected and logged using the Agilent 34970A Data Acquisition Switch Unit, scanning at a rate of 10 sets of measurements per second for startup, and at a slower rate of one set of measurements per 10 seconds, approaching steady-state.

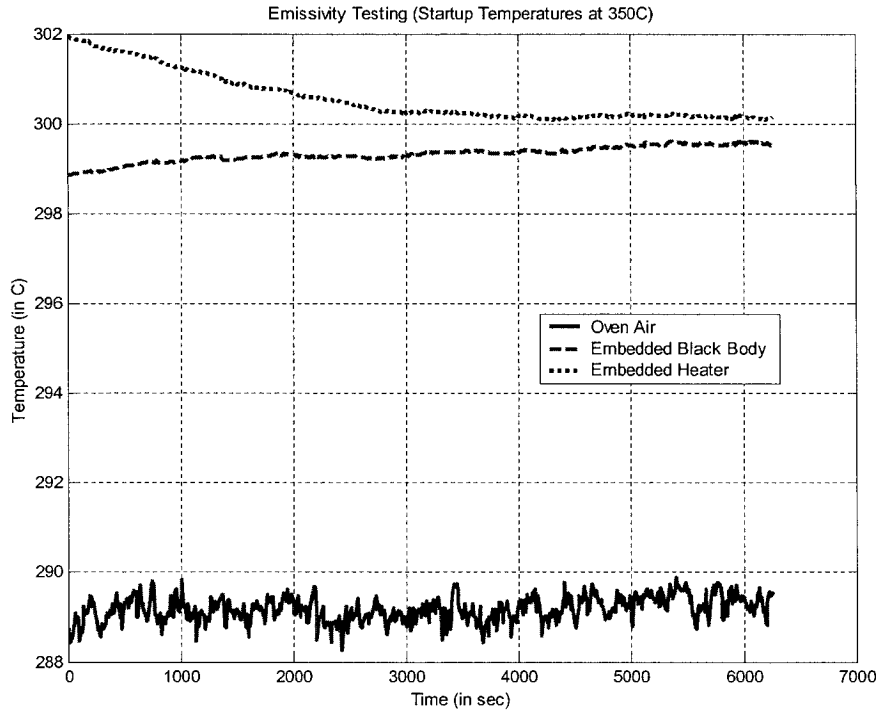


Figure 3-2: Steady-State Temperature Curves at 350C Setpoint

3.1.3.2 View Factors

The final component of the radiative heat transfer equation is called the view factor. Simply put, it corresponds to the fraction of energy emitted by surface A_1 that is received by surface A_2 .

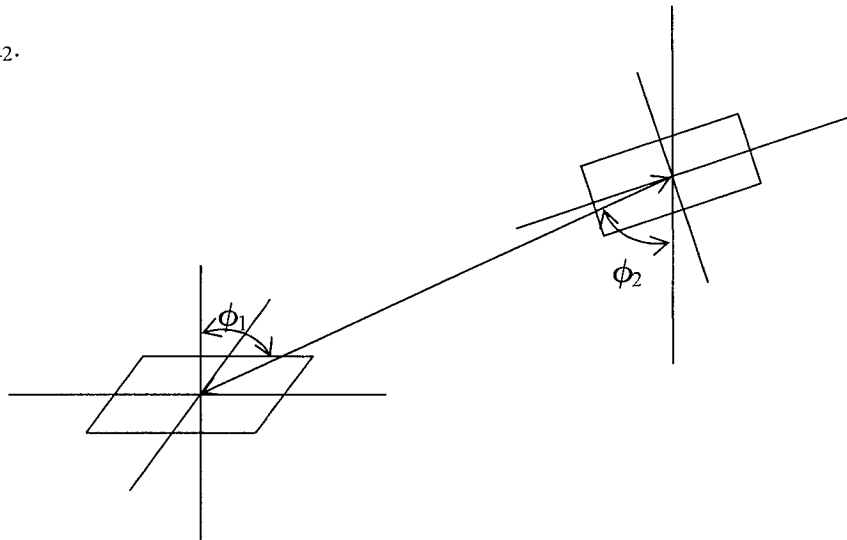


Figure 3-3: Radiation ray tracing between

finite parallel plate elements [10]

The intensity of radiation emitted by a surface element dA_1 is constant in a hemisphere of radius r from the surface. Any surface, dA_2 for instance, collecting radiation from another receives an amount that is proportional to its projection onto the surface area of the hemisphere [10]. The radiative heat flux equation then becomes:

$$q_{1 \leftrightarrow 2} = \sigma F_g (T_h^4 - T_s^4) \int_{A_1} \int_{A_2} \frac{\cos \phi_1 \cos \phi_2}{\pi r^2} dA_1 dA_2 \quad (3.17)$$

The view factor F is represented by the double-integral term. $\cos \phi_i$ are the direction cosines, and r is the solid angle radius between elements.

The reciprocity relation for view factors was derived for black bodies, but can apply to diffuse (meaning reflected energy is equally transferred in all directions) gray bodies as well. It states:

$$A_i F_{ij} = A_j F_{ji} \quad (3.18)$$

The reciprocity relation states that the fraction of energy leaving surface i and striking surface j (F_{ij}) is proportional to the fraction of energy leaving surface j and striking surface i (F_{ji}) by the ratio of their respective areas. This equation is useful for determining one view factor from another.

Incorporating all these elements, the final net radiative heat transfer equation becomes:

$$q_{hs} = \sigma A_h F_{hs} \varepsilon_{eff} (T_h^4 - T_s^4) \quad (3.19)$$

3.2 Plastic Sheet Modeling – Energy Absorption within the Sheet

Moore [16,17] developed a comprehensive model of the plastic sheet, using the basic heat transfer equations above. The sheet itself was discretized into several layers, each

defined by a node upon which boundary conditions were applied. This section explains Moore's sheet model in more detail, with some improvements regarding the absorption of energy within the plastic sheet.

3.2.1 Moore Model of Plastic Sheet

Moore divided the plastic sheet into N nodes, each a distance Δz from the next. Node 1 represented the upper surface of the sheet and node N the lower. Convention dictates that the node be located in the centre of each isothermal layer [15].

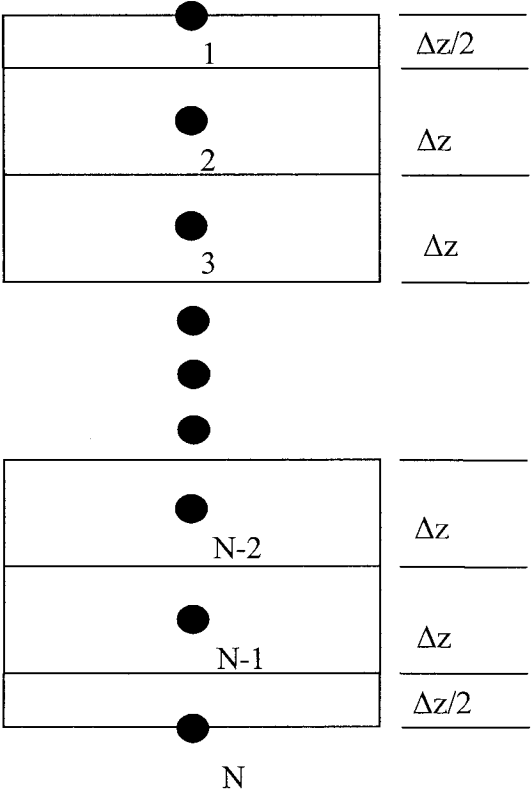


Figure 3-4: Plastic Sheet Discretization

Moore hypothesized that the primary mode of heat transfer occurring at the sheet surface was due to radiative heat transfer, proven later by Boulet et al., [26] with some

cooling effects due to natural convection and conduction. The energy balance equation for the surface nodes, 1 and N, is given below:

$$\rho V C p \frac{\partial T_{1,N}}{\partial t} = q_{in} - q_{out} \quad (3.20)$$

This equation states that the rate of change of energy for the outermost layers is equal to the energy flow rate into the layer minus the energy flow rate out of the layer. Dividing this equation into contributions from each heat transfer mode gives:

$$\frac{dT_1}{dt} = \frac{1}{\rho V C p} \left[q_{rad} + q_{conv} - \frac{kA}{\Delta z} (T_{1,N} - T_{2,N-1}) \right] \quad (3.21)$$

Note that, using the convention described above, the volume V in this case is equal to the area A of the surface multiplied by $\Delta z/2$, as the height of this layers is half the size of the others.

The conduction heat transfer from nodes 1 to 2 (or N to N-1) is given by $\frac{kA}{\Delta z} (T_{1,N} - T_{2,N-1})$.

The terms q_{rad} and q_{conv} are given below:

$$q_{conv} = h(T_{\infty} - T_{1,N}) \quad (3.22a)$$

$$q_{rad} = \sigma \epsilon_{eff} A_h \left[\sum_{i=1}^M (T_{heater_i}^4 - T_{1,N}^4) F_i \right] \quad (3.22b)$$

Here M denotes the number of independent heater banks in the thermoforming oven.

Within the sheet, conduction was presumed to be the sole mode of heat transfer, as the sheet slowly increased in temperature. The one-dimensional conduction equation is then used for the interior nodes of the sheet:

$$\rho C p \frac{\partial T_i}{\partial t} = k \frac{\partial^2 T_i}{\partial z^2} \quad (3.23)$$

Using a simple approximation for the second order term, the equation becomes:

$$\frac{dT_i}{dt} = \frac{k}{\rho C_p} \left(\frac{T_{i-1} - 2T_i + T_{i+1}}{\Delta z^2} \right) \quad (3.24)$$

However, the assumption that the energy within the sheet would be solely transferred through conduction was shown to be false. Some of the radiative energy striking the sheet surface actually penetrates into the surface before being absorbed by the plastic. This was demonstrated by Boulet et al. [26] in experimental research with thick sheets (12mm) at CNRC-NRC IMI.

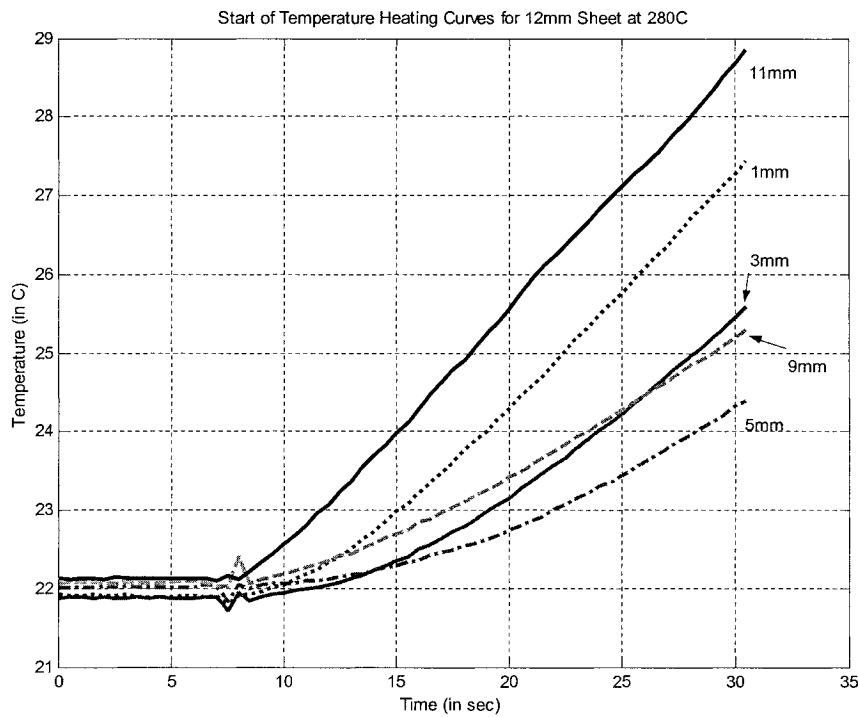


Figure 3-5: Start of Heating Curves for 12mm sheet at 280C

Since all thermocouples used in this experiment indicate an increase in temperature at

approximately the same time (8 seconds), the internal temperatures must be affected by a heat transfer mode other than conduction. If conduction were the sole mode of heat transfer for these depths, then a staggered start to the heating process would be seen above. Therefore, a secondary mode of energy transfer must be happening as well. This can only be due to radiation, which means that a certain portion of the energy enters into the sheet directly from the start of heating. Therefore the transmittivity of the plastic is not zero. The material then must absorb some of this transmitted energy as it passes through the sheet. This absorption of energy is described in detail in the section below.

3.2.2 Energy Absorption within the sheet

In a thermoforming oven, the heating element radiates energy towards the plastic sheet surface. The largest part of the energy is absorbed by the sheet (95% for a typical plastic - Table 3-3) and a small portion is reflected. Of that 95%, some is absorbed by the sheet itself, and some is transmitted through the sheet. In this case, the transmittivity τ is **not** zero. Therefore the energy balance equation for the interior nodes becomes [4]:

$$\frac{\partial T_i}{\partial t} = \frac{k}{\rho C p} \frac{\partial^2 T_i}{\partial x^2} + \dot{q}_{abs} \quad (3.25)$$

According to the Beer-Lambert Law [26], the transmittivity of a material depends on two main parameters: the spectral absorption coefficient of the material, as well as the material thickness. The law is stated below:

$$\begin{aligned} \ln(T_\lambda) &= -A_\lambda z \\ T_\lambda &= e^{-A_\lambda z} \end{aligned} \quad (3.26)$$

Note how both the transmittivity and absorptivity properties are wavelength-dependent.

Let A be the average absorptivity of the material across its spectrum. All that remains is to discretize the continuous transmittivity function, so that the amount of energy dissipated in each layer can be easily found.

Looking at the discretized sheet from Figure 3-4, it is noted that the exterior thicknesses are equal to $\Delta z/2$, and the interior ones equal to Δz . When the net radiative heat flux of intensity q_{rad} strikes the sheet surface, a portion of q_{rad} is absorbed inside the first zone and another portion is transmitted through the zone. By definition, the absorbed fraction of q_{rad} is $\beta(z)$, where z is the depth within the sheet. The calculation of $\beta(z)$ is done using the Beer-Lambert law. Then, when the thickness of the zone is Δz , the total absorbed energy becomes equal to the integral sum of all energies absorbed over that distance:

$$\begin{aligned}\beta(\Delta z) &= \int_0^{\Delta z} A e^{-Az} dz \\ \beta(\Delta z) &= \left[1 - e^{(-A\Delta z)} \right] = \beta_{in}\end{aligned}\quad (3.27)$$

Here A is the absorption coefficient with units of m^{-1} . With the thickness of the zone equal to $\Delta z/2$, the absorbed energy becomes:

$$\begin{aligned}\beta(\Delta z/2) &= \int_0^{\Delta z/2} A e^{-Az} dz \\ \beta(\Delta z/2) &= \left[1 - e^{(-A\Delta z/2)} \right] = \beta_{ex}\end{aligned}\quad (3.28)$$

Assuming a radiant source located on the top of the sheet shown in Figure 3-4, the following calculations can be made using the definitions above:

The absorbed energy in zone 1 is equal to:

$$Q_{a1} = \beta_{ex} Q \quad (3.29)$$

The radiant energy transmitted through zone 1 is simply equal to the remainder:

$$\begin{aligned} Q &= Q_{t1} + Q_{a1} \\ Q_{t1} &= (1 - \beta_{ex}) Q \end{aligned} \quad (3.30)$$

The absorbed energy in zone 2 is:

$$\begin{aligned} Q_{a2} &= \beta_{in} Q_{t1} \\ Q_{a2} &= \beta_{in} (1 - \beta_{ex}) Q \end{aligned} \quad (3.31)$$

The radiant energy transmitted through zone 2 is:

$$\begin{aligned} Q_{t1} &= Q_{t2} + Q_{a2} \\ Q_{t2} &= (1 - \beta_{in}) Q_{t1} = (1 - \beta_{in})(1 - \beta_{ex}) Q \end{aligned} \quad (3.32)$$

Similarly for zone 3, the absorbed energy becomes:

$$Q_{a3} = \beta_{in} Q_{t2} = \beta_{in} (1 - \beta_{in})(1 - \beta_{ex}) Q \quad (3.33)$$

The transmitted energy through zone 3:

$$Q_{t3} = (1 - \beta_{in}) Q_{t2} = (1 - \beta_{in})^2 (1 - \beta_{ex}) Q \quad (3.34)$$

For zone n, the following equations for the absorbed and transmitted energy can be derived:

$$\begin{aligned} Q_{an} &= \beta_{in} (1 - \beta_{in})^{n-2} (1 - \beta_{ex}) Q \\ Q_{tn} &= (1 - \beta_{in})^{n-1} (1 - \beta_{ex}) Q \end{aligned} \quad (3.35)$$

For the bottommost zone (zone N), the equations become:

$$\begin{aligned} Q_{aN} &= \beta_{ex} (1 - \beta_{in})^{N-2} (1 - \beta_{ex}) Q \\ Q_{tN} &= (1 - \beta_{in})^{N-1} (1 - \beta_{ex})^2 Q \end{aligned} \quad (3.36)$$

The last equation corresponds to the radiant energy transmitted through the entire

thickness of the plastic sheet. So the absorbed energy inside the plastic sheet is the difference between the energy entering in the plastic sheet and the energy transmitted:

$$Q_{ABS} = Q - Q_{IN} = \left\{ 1 - (1 - \beta_{in})^{N-1} (1 - \beta_{ex})^2 \right\} Q \quad (3.37)$$

The remaining section of this chapter will serve to put together the complete model for the heating element-plastic sheet system.

3.3 Complete Heater-Sheet State-Space Model

The state-space model of the heating element-plastic sheet system is discussed in this section. Using the derivations above, along with parts of the Moore model, a detailed representation of the CNRC-NRC IMI thermoforming machine (AAA) is obtained. It will then be tested against experimental data. Some tuning of the model parameters (conduction, convection, absorption coefficients, etc.) will be needed to correlate the results of the simulation to the experimental data.

3.3.1 Definitions

Many state-space systems can be defined from first principles and initial conditions. The differential equations that describe the system can then be turned into equations of the following form [12]:

$$\begin{aligned} \dot{x} &= Ax + Bu \\ y &= Cx + Du \end{aligned} \quad (3.38)$$

Here, x represents the state of the system, u represents the inputs, and y the outputs. A , B , C , and D (often $D = 0$) are the matrices that relate each of them to the other.

The sheet is divided into 6 equal zones, each with 5 layers, making a total of 30

different locations at which the temperature will be calculated. Each of these is defined as a state of the system. There are 12 sets of heating elements, each with its own PID controller. Each of these is considered an input to the system. The outputs can be selected as desired, by choosing the entries of matrix C . Then, the temperature at any point within the sheet, or on the sheet surface, can be examined during the entire heating cycle.

3.3.2 State equations

The state equations for this system are derived from the energy balance equations seen above. Let the plastic sheet be divided into M zones. For a given sheet zone i , the energy balances at the sheet surface are similar to those seen in the Moore model, but the absorption terms have been included:

$$\begin{aligned} Upper &\Rightarrow \frac{dT_{i1}}{dt} = \frac{2}{\rho C_p \Delta z} \left\{ \left(\frac{k}{\Delta z} T_{i2} - \frac{k}{\Delta z} T_{i1} \right) + \left(h T_{\infty top} - h T_{i1} \right) + \left(Q_{T_{i1}} + Q_{B_{i1}} \right) \right\} \\ Lower &\Rightarrow \frac{dT_{i5}}{dt} = \frac{2}{\rho C_p \Delta z} \left\{ \left(\frac{k}{\Delta z} T_{i4} - \frac{k}{\Delta z} T_{i5} \right) + \left(h T_{\infty bottom} - h T_{i5} \right) + \left(Q_{T_{i5}} + Q_{B_{i5}} \right) \right\} \quad (3.39) \end{aligned}$$

Note that the temperature at node 1 for zone i is given by T_{i1} , and the temperature at node 5 is given by T_{i5} .

Within the large brackets, the first term represents the conduction heat transfer, the second convection heat transfer, and the final term represents a combination of radiation heat transfer, energy absorption and energy transmission. Energy is absorbed both from the top and the bottom of the sheet, as the system has radiant energy sources (heating elements) acting on both sides of the sheet. Therefore, there are both upper and lower absorption terms. The indices correspond to the node number in each case. Here the first

term in the large bracket represents conduction as above, but the second term represents energy transmission and absorption only.

The energy balance equations for the interior layers also resemble the Moore equations.

But with absorption included, they become:

$$\begin{aligned}
 \frac{dT_{i2}}{dt} &= \frac{1}{\rho C_p \Delta z} \left\{ \frac{k}{\Delta z} [T_{i1} - 2T_{i2} + T_{i3}] + [Q_{T_{i2}} + Q_{B_{i2}}] \right\} \\
 \frac{dT_{i3}}{dt} &= \frac{1}{\rho C_p \Delta z} \left\{ \frac{k}{\Delta z} [T_{i2} - 2T_{i3} + T_{i4}] + [Q_{T_{i3}} + Q_{B_{i3}}] \right\} \\
 \frac{dT_{i4}}{dt} &= \frac{1}{\rho C_p \Delta z} \left\{ \frac{k}{\Delta z} [T_{i3} - 2T_{i4} + T_{i5}] + [Q_{T_{i4}} + Q_{B_{i4}}] \right\}
 \end{aligned} \tag{3.40}$$

The absorption terms are described in greater detail here, for the upper and lower heat sources respectively:

$$\begin{aligned}
 Q_{T_{i1}} &= \beta_1 Q_{RT_i} \\
 Q_{T_{i2}} &= \beta_2 (1 - \beta_1) Q_{RT_i} \\
 Q_{T_{i3}} &= \beta_2 (1 - \beta_2)(1 - \beta_1) Q_{RT_i} \\
 Q_{T_{i4}} &= \beta_2 (1 - \beta_2)^2 (1 - \beta_1) Q_{RT_i} \\
 Q_{T_{i5}} &= \beta_2 (1 - \beta_2)^3 (1 - \beta_1) Q_{RT_i}
 \end{aligned} \tag{3.41}$$

$$\begin{aligned}
 Q_{B_{i5}} &= \beta_2 (1 - \beta_2)^3 (1 - \beta_1) Q_{RB_i} \\
 Q_{B_{i4}} &= \beta_2 (1 - \beta_2)^2 (1 - \beta_1) Q_{RB_i} \\
 Q_{B_{i2}} &= \beta_2 (1 - \beta_1) Q_{RB_i} \\
 Q_{B_{i1}} &= \beta_1 Q_{RB_i}
 \end{aligned} \tag{3.42}$$

The total radiant energy (both top and bottom) hitting the sheet is shown below:

$$\begin{aligned}
 Q_{RT_i} &= \sigma \varepsilon_{eff} \sum_{j=1}^{P_T} F_{T_{ij}} \left(T_{S_{T_j}}^4 - T_{i1}^4 \right) \\
 Q_{RB_i} &= \sigma \varepsilon_{eff} \sum_{j=1}^{P_B} F_{B_{ij}} \left(T_{S_{B_j}}^4 - T_{i5}^4 \right)
 \end{aligned} \tag{3.43}$$

Here, P_T and P_B represent the number of heating element zones on the top and bottom of the oven respectively. Similarly, $T_{S_{T_j}}$ and $T_{S_{B_j}}$ are the surface temperatures of each heating zone. In order to fit these equations into state-space form, some simplifications must be made. The following variables can be defined:

$$\begin{aligned}
a &= \frac{1}{\rho C_p \Delta x} \\
b &= \frac{k}{\Delta x} \\
c_1 &= \sigma \varepsilon_{eff} \beta_1 \\
c_2 &= \sigma \varepsilon_{eff} \beta_1 (1 - \beta_2) \\
c_3 &= \sigma \varepsilon_{eff} \beta_2 (1 - \beta_1)(1 - \beta_2) \\
c_4 &= \sigma \varepsilon_{eff} \beta_2 (1 - \beta_1)(1 - \beta_2)^2 \\
c_5 &= \sigma \varepsilon_{eff} \beta_2 (1 - \beta_1)(1 - \beta_2)^3
\end{aligned} \tag{3.44}$$

Finally, the state-space matrix equations for zone i become:

$$\begin{aligned}
\begin{bmatrix} \dot{x}_1^i \\ \dot{x}_2^i \\ \dot{x}_3^i \\ \dot{x}_4^i \\ \dot{x}_5^i \end{bmatrix} &= \begin{bmatrix} -2a(h+b) & 2ab & 0 & 0 & 0 \\ ab & -2ab & ab & 0 & 0 \\ 0 & ab & -2ab & ab & 0 \\ 0 & 0 & ab & -2ab & ab \\ 0 & 0 & 0 & 2ab & -2a(h+b) \end{bmatrix} \begin{bmatrix} x_1^i \\ x_2^i \\ x_3^i \\ x_4^i \\ x_5^i \end{bmatrix} \\
&+ \begin{bmatrix} 2ah & 0 \\ 0 & 0 \\ 0 & 0 \\ 0 & 0 \\ 0 & 2ah \end{bmatrix} \begin{bmatrix} T_{\infty top} \\ T_{\infty bottom} \end{bmatrix} + \frac{a}{\sigma \varepsilon_{eff}} \begin{bmatrix} 2c_1 & 2c_5 \\ c_2 & c_4 \\ c_3 & c_3 \\ c_4 & c_2 \\ 2c_5 & 2c_1 \end{bmatrix} \begin{bmatrix} Q_{RT}^i \\ Q_{RB}^i \end{bmatrix}
\end{aligned} \tag{3.45}$$

The superscript i denotes the sheet zone. The state variables are the temperatures at each of the sheet layers. For instance, if the number of sheet zones M is equal to 6, each zone having 5 layers, there is a total of 30 state variables.

One final simplification gives:

$$\begin{aligned}
Q_{RT}^i &= \sigma \varepsilon_{eff} \sum_{j=1}^{P_T} F_{T_{ij}} \left(T_{S_{T_j}}^4 - T_{i1}^4 \right) = \sigma \varepsilon_{eff} \left\{ \left[\sum_{j=1}^{P_T} F_{T_{ij}} T_{S_{T_j}}^4 \right] - F_{T_i} \left(x_1^i \right)^4 \right\} \\
Q_{RB_i} &= \sigma \varepsilon_{eff} \sum_{j=1}^{P_B} F_{B_{ij}} \left(T_{S_{B_j}}^4 - T_{i5}^4 \right) = \sigma \varepsilon_{eff} \left\{ \left[\sum_{j=1}^{P_B} F_{B_{ij}} T_{S_{B_j}}^4 \right] - F_{B_i} \left(x_5^i \right)^4 \right\}
\end{aligned} \tag{3.46}$$

The final version of the matrix equations for zone i can then be written as follows:

$$\dot{x}^i = Ax^i + B_\infty T_\infty + a \begin{bmatrix} 2c_1 & 2c_5 \\ c_2 & c_4 \\ c_3 & c_3 \\ c_4 & c_2 \\ 2c_5 & 2c_1 \end{bmatrix} \begin{bmatrix} \sum_{j=1}^{P_T} F_{T_{ij}} T_{S_{T_j}}^4 \\ \sum_{j=1}^{P_B} F_{B_{ij}} T_{S_{B_j}}^4 \end{bmatrix} - a \begin{bmatrix} 2c_1 F_T & 2c_5 F_B \\ c_2 F_T & c_4 F_B \\ c_3 F_T & c_3 F_B \\ c_4 F_T & c_2 F_B \\ 2c_5 F_T & 2c_1 F_B \end{bmatrix} \begin{bmatrix} \left(x_1^i \right)^4 \\ \left(x_5^i \right)^4 \end{bmatrix} \tag{3.47}$$

The problem with building a controller for this system becomes apparent when the final term of the above equation is observed. The radiation heat transfer portion of the energy balance depends on the temperature at the sheet surface to the 4th power, which is non-linear. For this reason, complex robust linear controllers, like H-infinity and model predictive control, may prove difficult to use to control the system.

3.3.3 Model Validation

In order to be able to use the model to design a controller for the system, the model must first be validated. In other words, experiments must be performed so that the model can be tuned to the parameters of the actual sheet-heater system. Then this tuned model can be used to simulate the actual plant of the system.

3.3.3.1 Test setup

Testing was done in the AAA thermoforming oven at CNRC-NRC IMI. In order to

properly determine the conduction and absorption properties of HDPE, a sheet thick enough to accommodate several thermocouples was needed. For this reason, a 12mm thick sheet was used. The dimensions of the sheet were 205mm by 230mm. The test setup is shown in Figure 3-6 below:

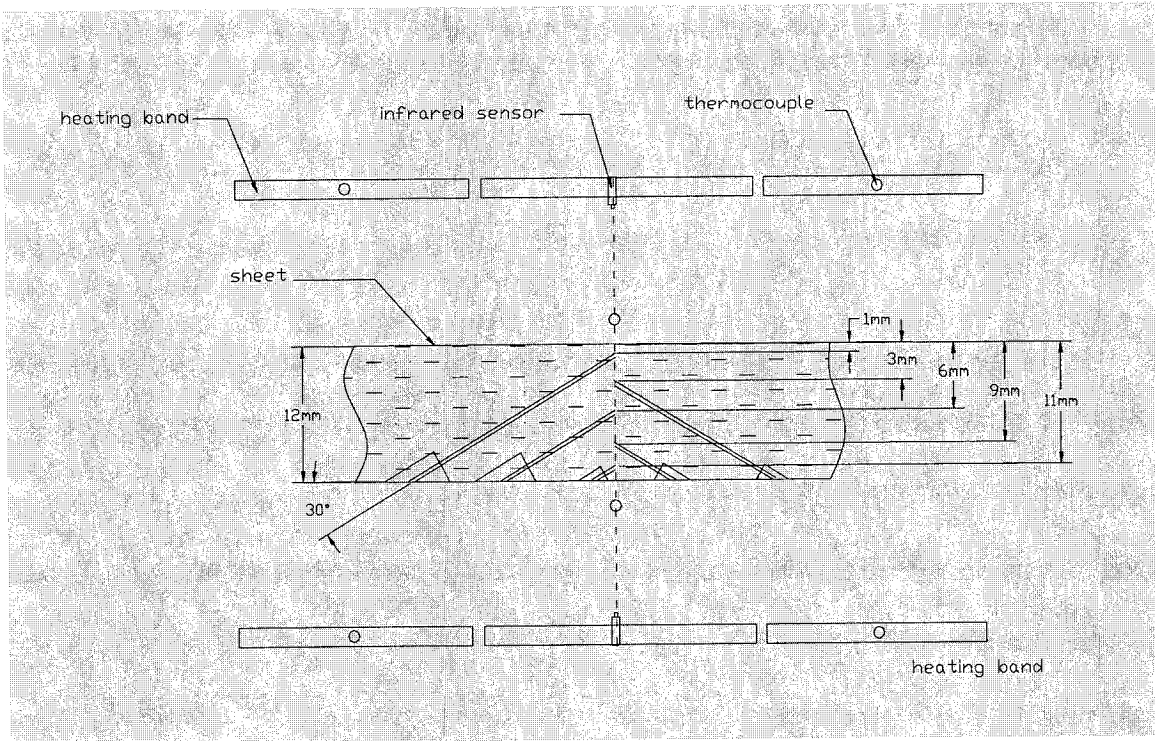


Figure 3-6: Test Setup for Thick Sheet Experiments

The 5 thermocouples were inserted into small holes that were drilled in the sheet at an angle of 30 degrees. The holes were drilled in such a way that the end of each thermocouple was precisely located on the centre plane of the sheet. Thermocouples were placed at depths of 1, 3, 5, 9, and 11 mm. The upper and lower surface temperatures of the sheet were measured using Raytek Non-Contact Compact Series MID IR sensors. The simulated 12mm sheet was divided into 5 nodes, each separated by a depth of 3 mm. Therefore, the only nodes that correspond to physical thermocouple locations are at 3 and

9mm. The IR measurements taken at the sheet surfaces were difficult to correlate to the simulation model, and therefore were not used in the comparisons. Also these IR measurements will be used directly for control, whereas the internal temperatures will have to be inferred from the model results, as no thermocouples can be inserted into the sheet during the heating cycle.

3.3.3.2 Experimental results

Three tests were performed, each with only the lower heater bank active. The upper bank was turned off in order to minimize the sag effect on the sheet. Heating from both sides decreases the length of the test, which can cause degradation of the sheet. For the first test, the lower zones were held at 280°C. The second test saw a slightly higher setpoint for the lower zones, 320°C. Finally, for the third test, the setpoint was at 420°C.

The first in each set of graphs below show the experimental temperature curves at 1mm, 3mm, 9mm, and 11mm, as measured from the lower surface of the sheet. The second represents the tuned simulation data, in the centre zone of the sheet, at each of the 5 nodes (0, 3, 6, 9 and 12mm), also from the lower surface. The third graph is simply the difference between the simulation and experimental data at 3mm and 9mm, or the simulation error.

The model parameters that can be tuned are the following: upper and lower ambient air temperatures, convection coefficient, heat capacity, density, conduction coefficient, and absorption coefficient. The latter four are strictly material dependent, and only the conduction coefficient k is not temperature dependent. However, to keep the model as simple as possible, these temperature dependencies were not taken into account. These

will be investigated as part of the larger McGill University-CNRC-NRC IMI research program.

For the 280°C case, the results are shown in Figure 3-7, Figure 3-8, and Figure 3-9.

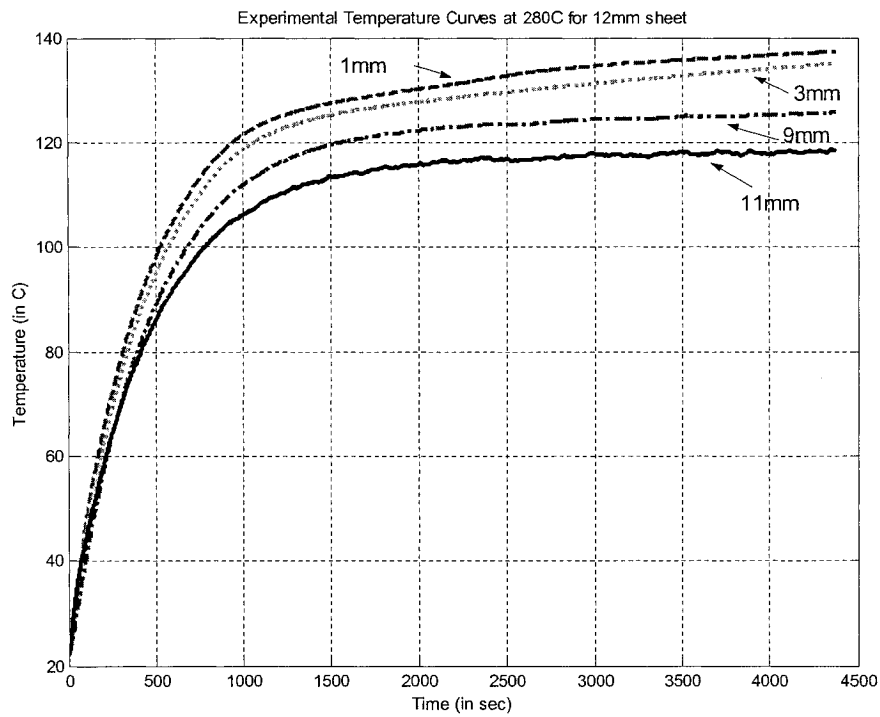


Figure 3-7: 280C Experimental Temperature Curves

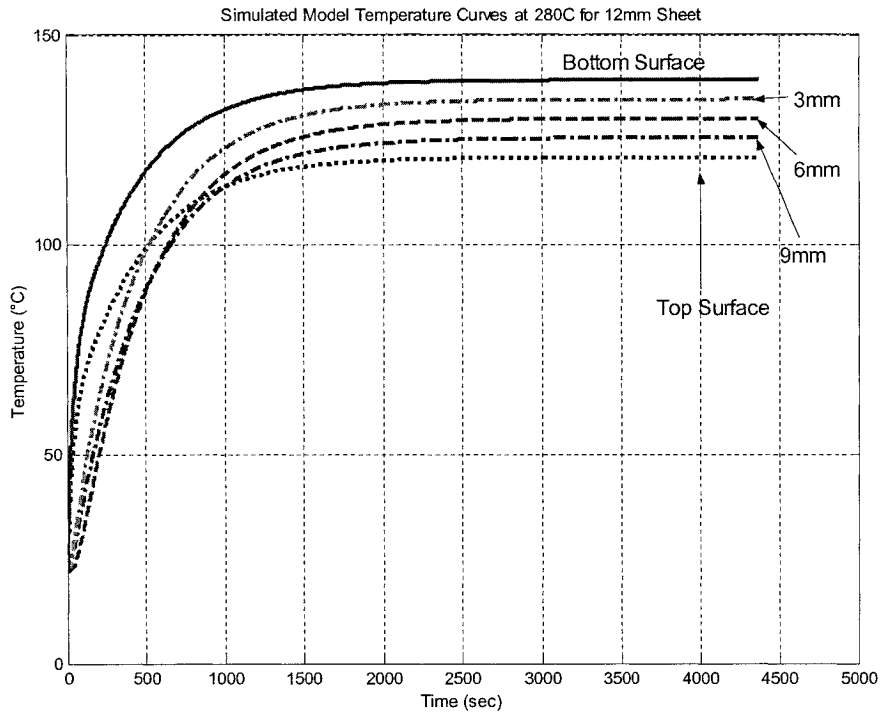


Figure 3-8: 280C Simulation Model Temperature Curves

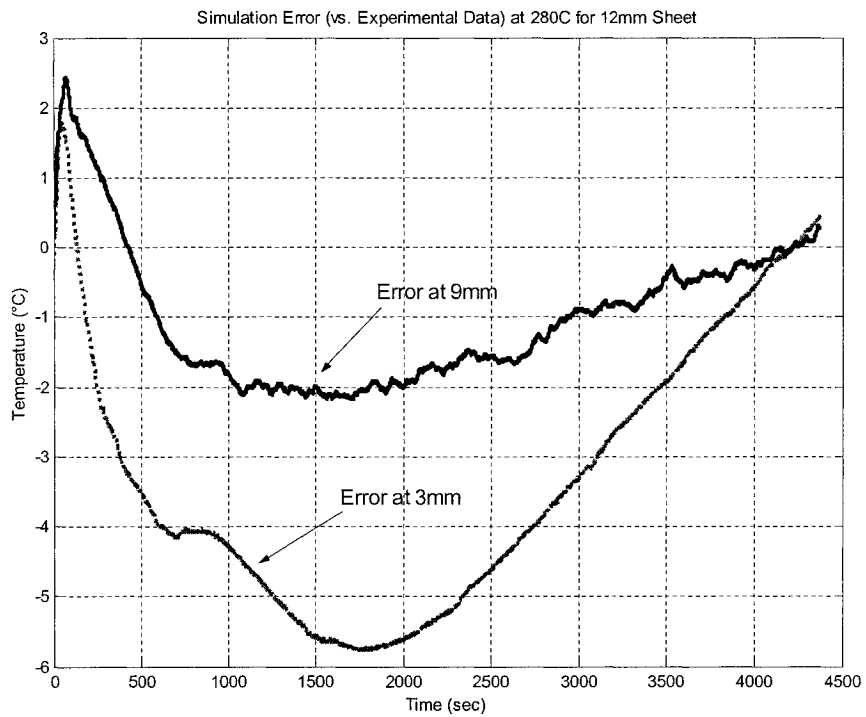


Figure 3-9: 280C Simulation Error (vs. Experimental Data)

For this test, the model parameters were tuned such that the resulting temperature error curves remain within 6°C of their corresponding experimental data. The parameter values are listed in Table 3-5 below. Figure 3-10, Figure 3-11, and Figure 3-12 show the curves for the 320°C tests:

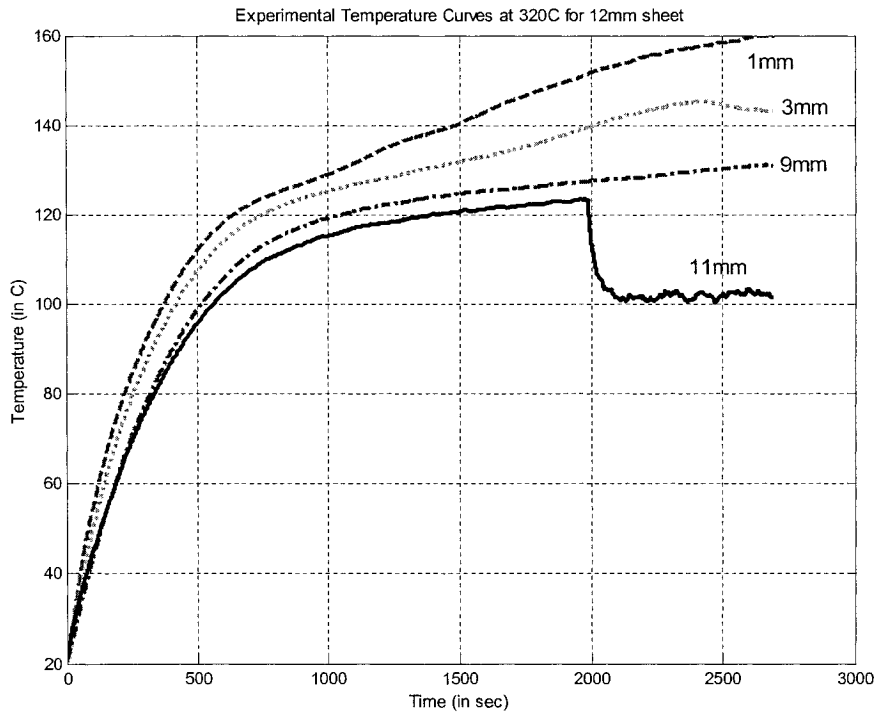


Figure 3-10: 320C Experimental Temperature Curves

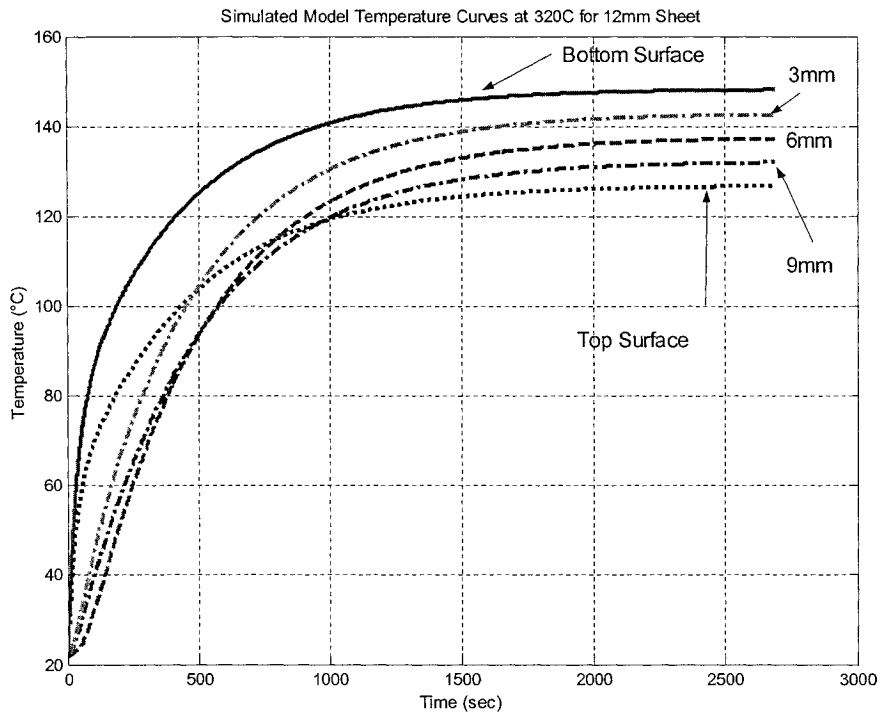


Figure 3-11: 320C Simulated Model Temperature Curves

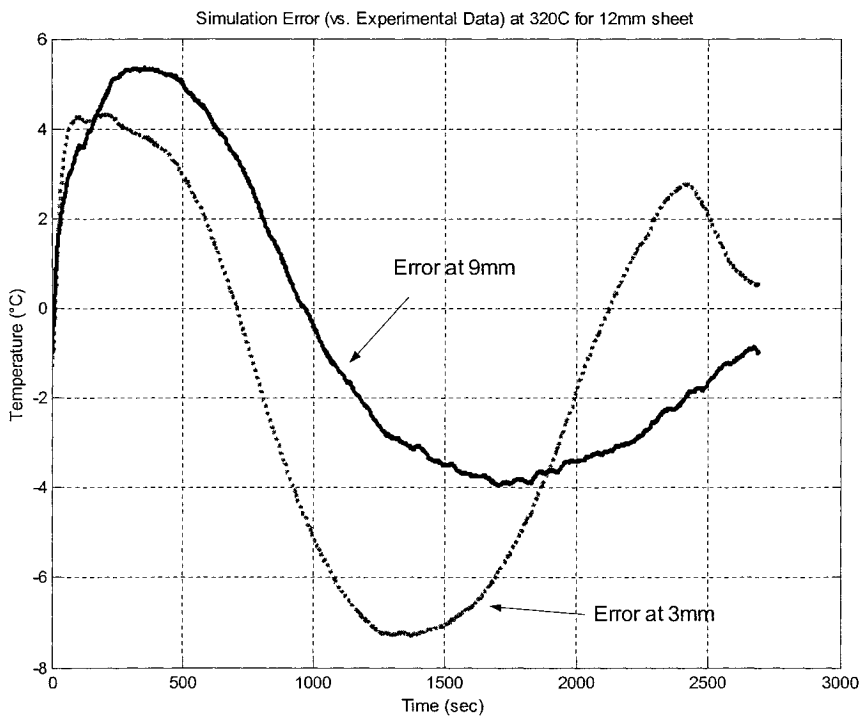


Figure 3-12: 320C Simulation Error (vs. Experimental Data)

Note that the 11mm thermocouple registered a measurement error at approximately 2000 seconds. Any data collected after this time by this thermocouple was ignored. Also, the temperature error curves again remain within 8°C of their setpoints.

Finally, the 420°C test results are described in Figure 3-13, Figure 3-14, and Figure 3-15 below:

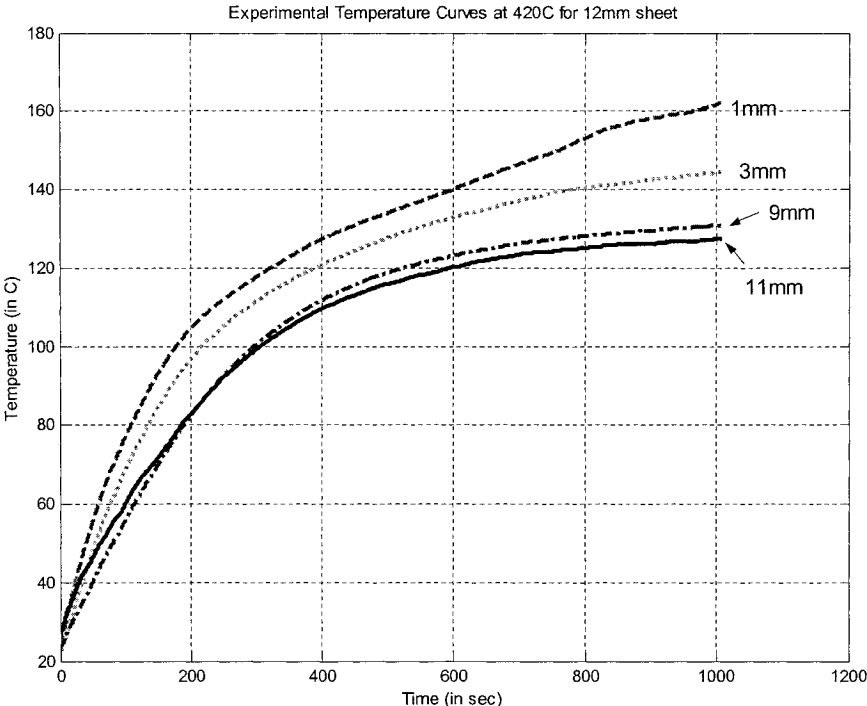


Figure 3-13: 420C Experimental Temperature Curves

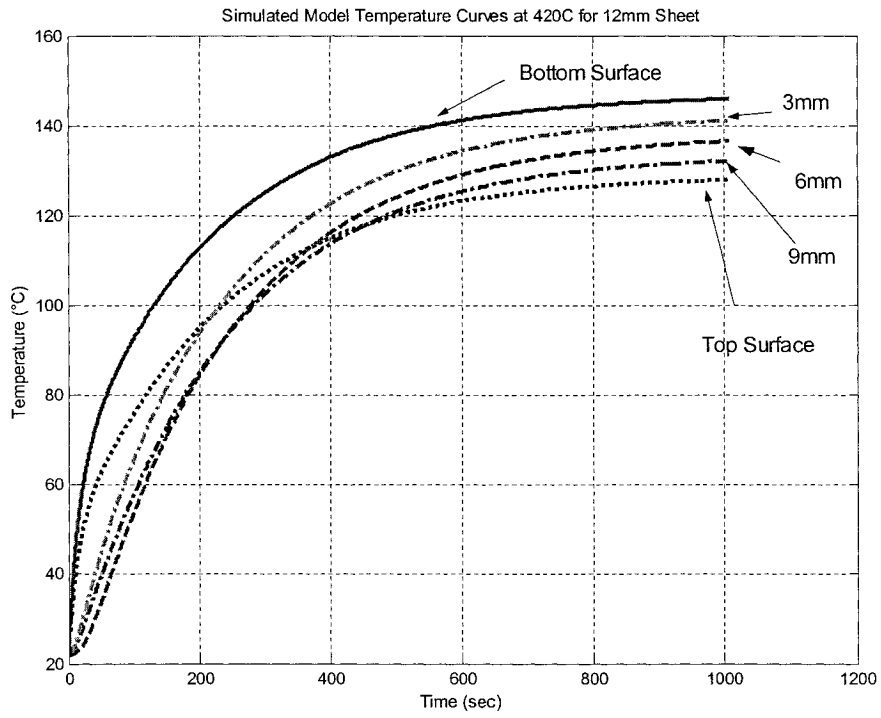


Figure 3-14: 420C Simulated Model Temperature Curves

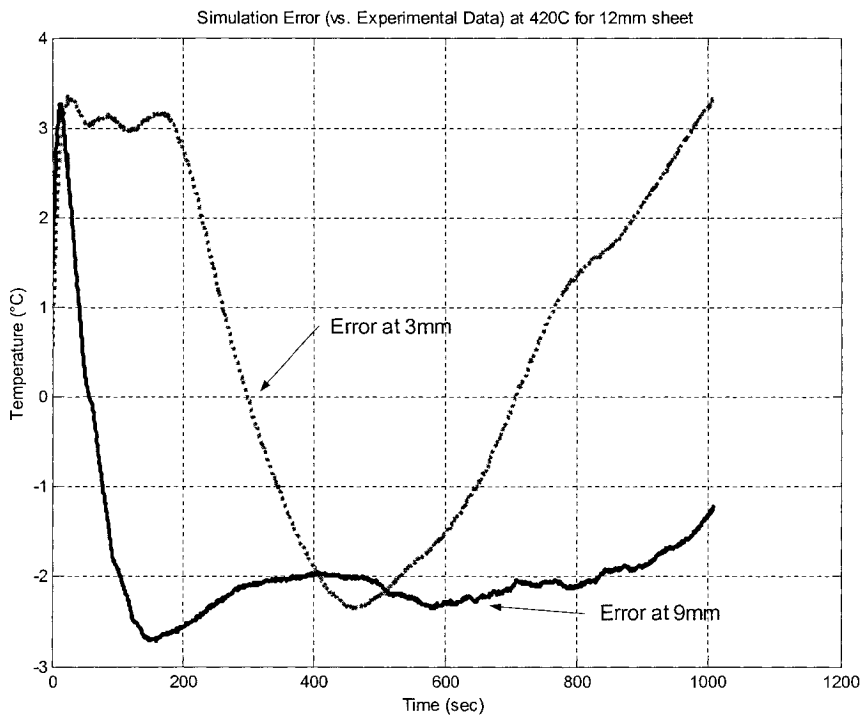


Figure 3-15: 420C Simulation Error (vs. Experimental Data)

For this last test, the error seems to be the closest to the setpoint, as the margin is only approximately 3°C.

A closer look at Table 3-5 reveals the tuned simulation parameters for each case:

Table 3-5: Tuned Simulation Parameters for 280C, 320C and 420C tests

<i>Parameter</i>	<i>280C</i>	<i>320C</i>	<i>420C</i>
Air Temp Bottom (C)	145C	155C	155C
Air Temp Top (C)	115C	120C	120C
k (W/(m·K))	38.4	38.4	38.4
h (W/(m ² ·K))	30	30	20
ρ (kg/m ³)	850	850	550
C_p (J/(kg·K))	1700	1700	1000
A (m ⁻¹)	30	30	30
% error at 3mm	0.33%	0.35%	2.28%
% error at 9mm	0.22%	-0.77%	-0.94%

The percent error formula used is given below, where *Experimental* is the final experimental temperature and *Simulated* is the final temperature from the simulation:

$$\text{Percent error} = \frac{\text{Experimental} - \text{Simulated}}{\text{Experimental}} \times 100\% \quad (3.48)$$

It quickly becomes clear that the 420°C test parameters are not logical. To make the simulated temperatures resemble the experimental ones, certain parameters, namely

density (ρ) and heat capacity (C_p) were chosen well outside of their acceptable range for HDPE. Also, the ambient air temperatures cannot be the same for the 320°C test and the 420°C test. Simple measurements have been performed indicating that the air temperature should be at least 175°C above the sheet and close to 200°C below it for a heater setpoint of 420°C.

For the other two cases, the material parameters obtained via simulation are close to the nominal values for HDPE. Similarly, the physical parameters of the system approach those measured during other testing (ambient air temperatures). The only parameter not within nominal range is the convection coefficient, h . Because of the large openings at either end of the oven, there may be unseen air currents causing major conduction effects at the sheet surfaces, such that the upper sheet surface temperature is higher than the lower sheet surface temperature, contrary to a more typical oven, where the lower surface is hotter.

Other potential reasons for error are enunciated more clearly below:

3.3.3.3 Reasons for error

The simulation model remains a work in progress, for several reasons. Each of the temperature dependent parameters must be adjusted as the temperature of the sheet increases. So, for instance, the constant heat capacity can be replaced with a temperature-dependent version, thereby improving the response of the model. For instance, increasing the heat capacity will have an effect on the transient response of the sheet model. This increase will create a larger thermal inertia. Therefore, it will take more energy to heat the same amount of plastic, which essentially means a slowing down of the transient

response of the sheet model. A similar temperature-dependent function can be implemented for the density as well. These functions are being investigated by other students and researchers at McGill and CNRC-NRC IMI.

There are also a couple of important points regarding the heating elements themselves. The model views each oven zone as a large heater block, of size 30cm by 30cm approximately. However, the actual oven is composed of 3 heating elements each of size 6cm by 25cm, with a small 4cm gap between each heater (see Chapter 4 – Figure 4-4 for the oven dimensions). These small gaps do not represent much surface area by themselves, but when added up, they total 40% of the oven surface. Therefore, the model overestimates the amount of actual heating surface area when the oven is heating the sheet. However, this problem may be counterbalanced by another physical phenomenon. The heating element does not uniformly heat to the temperature setpoint of the PID. Figure 3-16 below shows an actual representation of the surface temperature of a heating element at a setpoint of 300C, taken with the AGEMA Infrared camera.

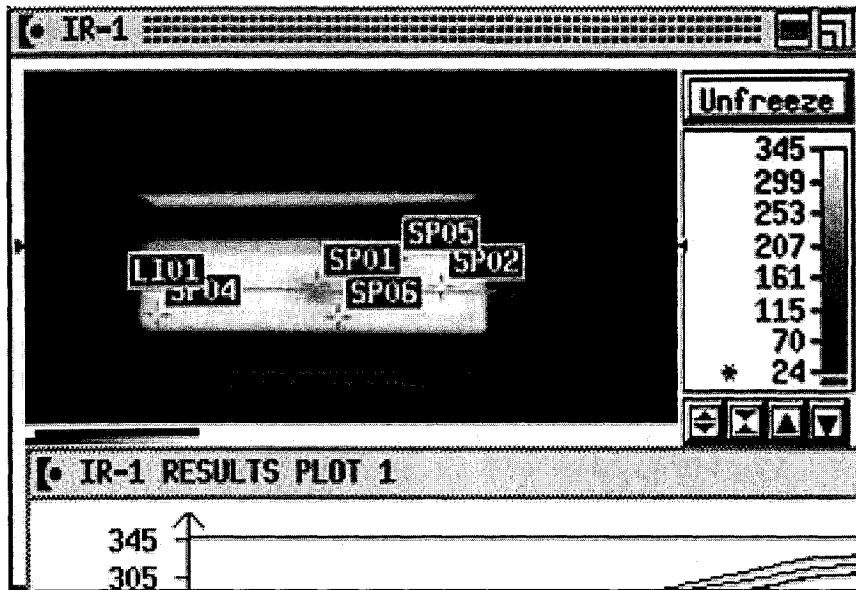


Figure 3-16: IR temperature measurement of Heating Element Surface (setpoint 300C)

The temperatures along the line LI01, as well as a histogram showing the temperature distribution over the whole line are given below:

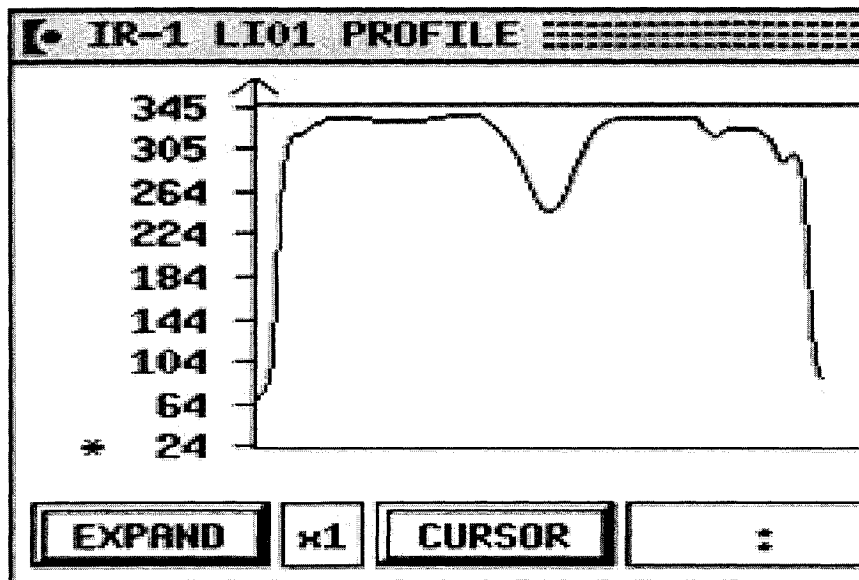


Figure 3-17: LI01 data line from IR Camera picture above (setpoint 300C)

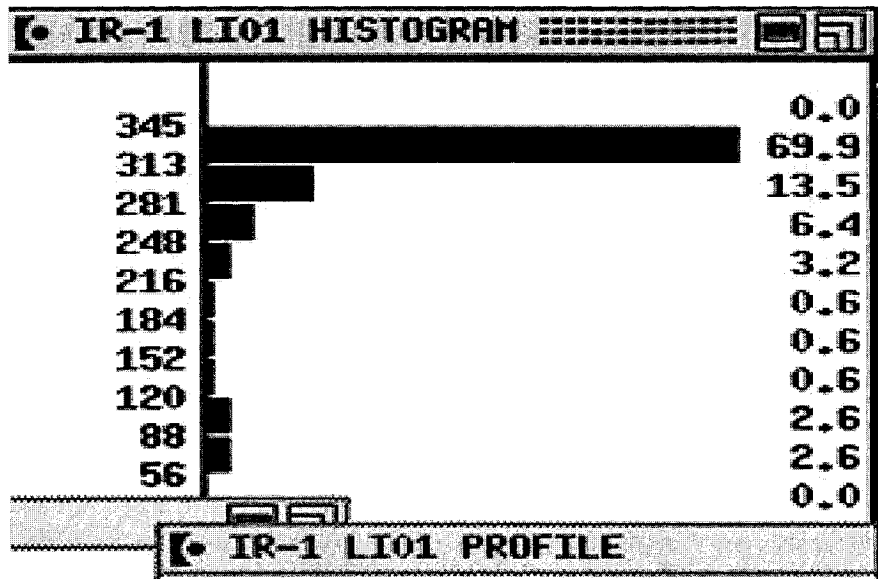


Figure 3-18: Histogram showing temperature distribution along line LI01

The embedded thermocouple measuring the temperature that is compared to the PID setpoint appears to be in a “cold” spot when compared to the rest of the surface area of the heating element. This shows that the model is underestimating the surface temperature of the whole heating element by taking the lower setpoint value instead of the actual value. These two effects combined need to be studied in greater detail so that the simulation model developed in this chapter can be completed.

Finally, the model tuning performed above is done with one large assumption: that the sheet exhibits **only** one-dimensional conduction heat transfer (i.e. through the depth of the sheet). It assumes that the sheet is thin enough that each sheet zone does not lose (or gain) any conduction energy from its adjacent zones. This assumption may not hold true for these sample tests, as the sheet used was 12mm thick. This is another area where the model can be improved.

Chapter 4 Real-time control of AAA Thermoforming oven

Real-time control of any process is a complicated and difficult task to accomplish. Often, for industrial processes like thermoforming, any control effort is done in open-loop. This means the machine operator checks the final result (i.e., a thermoformed sheet), and adjusts the settings on the machine if the results are not satisfactory. The operator will then “tweak” the machine settings until he/she gets a part that is deemed acceptable. The settings are then left alone until shutdown or until machine drift has caused part errors, whereupon the entire “tweaking” process will have to be repeated. However, using the OPAL-RT RT-LAB real-time operating software, real-time control becomes much easier to implement. Infrared sensors are placed in positions such that specific sheet surface temperatures are measured with 0.1°C accuracy. The sheet temperatures can then be controlled as desired during the heating cycle.

First, an overview of the AAA thermoforming machine at CNRC-NRC IMI will be given. The existing control structure of the system will be examined, a PID feedback control loop connected to Solid-State Relays. These relays act as switches, allowing current to flow through the heating elements when the PID output is high, and blocking the current when it is low. Also, the actuators of the system (the heating elements themselves) will be studied, more specifically their heating and cooling rates (which are not the same). Then the IR sensors will be investigated as well: a brief explanation of how they work, how they are calibrated, and where they are located within the AAA oven. Finally, a description of the OPAL-RT RT-LAB hardware and software used to develop and operate the real-time model and controller will be shown as well.

The next section of this chapter will focus on the control algorithm proposed and implemented for the AAA thermoforming machine. The multilayer algorithm will be broken down into its inner and outer loops. The inner loop will focus on the replacing of the hardware PID control with a software version within the RT-LAB model. The outer loop will focus first on developing the steady-state relationship between the heating elements and the temperatures measured by the IR sensors in different locations. Using this steady-state gain matrix, a basic PI controller is then implemented for each of the IR sensors for both step and ramp inputs.

4.1 AAA Machine Overview

First, the AAA thermoforming oven used at CNRC-NRC IMI will be examined. The zones of heating elements, the PID blocks used to monitor and control the temperature of each zone, and the oven layout will all be discussed. Then, the hardware added to the AAA machine for the purposes of real-time process control will be described. The infrared sensors and the OPAL-RT RT-LAB operating software will be discussed one at a time.

4.1.1 System Actuators and Layout

The AAA thermoforming machine at CNRC-NRC IMI is shown in Figure 4-1 below. By thermoforming machine standards, it is small, used to form small sheets of 69 cm x 99 cm maximum. Note that the sheet enters into the oven between the trays of heating elements, which are situated above and below the sheet entry plane.

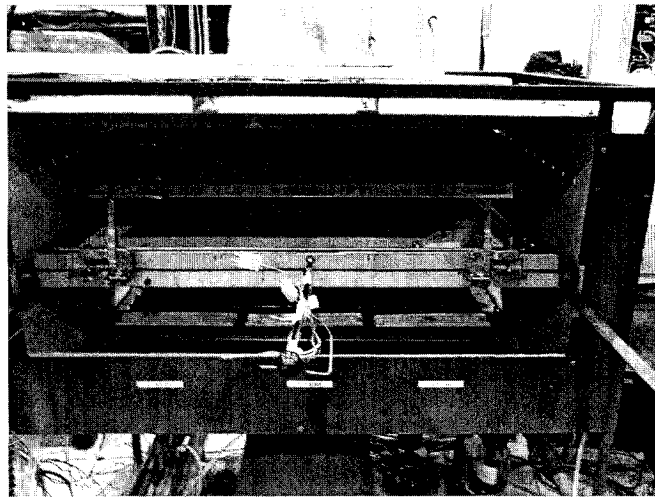


Figure 4-1: AAA Thermoforming machine (front view)

Inside the oven, the heating elements are arranged in the following manner: 36 heating elements are split equally between top and bottom, divided in such a way that there are 12 heating zones. Each zone contains 3 heating elements connected in parallel, one of which is shown in Figure 4-2. Each Tempco-made heating element supplies up to 650W of 3-phase power. The basic ceramic infrared heater design consists of a high-temperature nickel-chromium alloy resistance coil evenly distributed and embedded into the ceramic during the casting process. The coil is located as close as possible to the element surface in order to deliver maximum efficiency. The range of infrared wavelengths is from 2-10 μm [27].

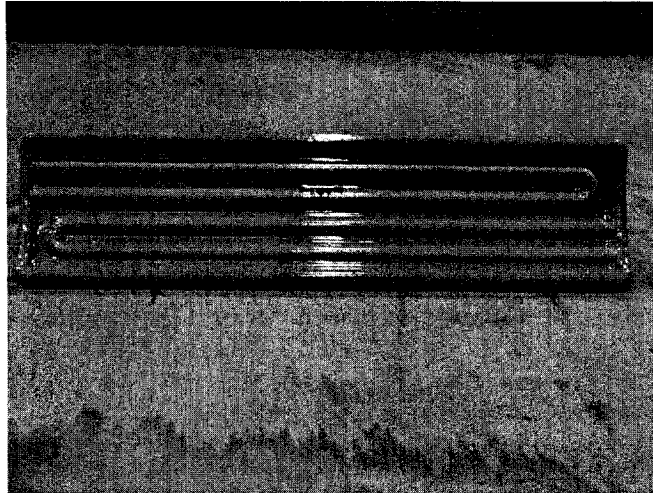


Figure 4-2: Tempco 650W Heating element

The heating elements are laid out in a similar manner, top and bottom. A view of the lower tray can be seen in Figure 4-3 below:

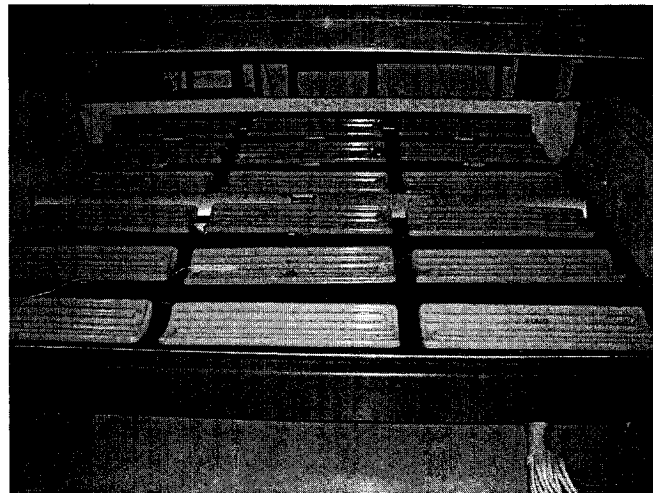


Figure 4-3: Lower Heating tray

The exact dimensions of the heating tray are given in Figure 4-4.

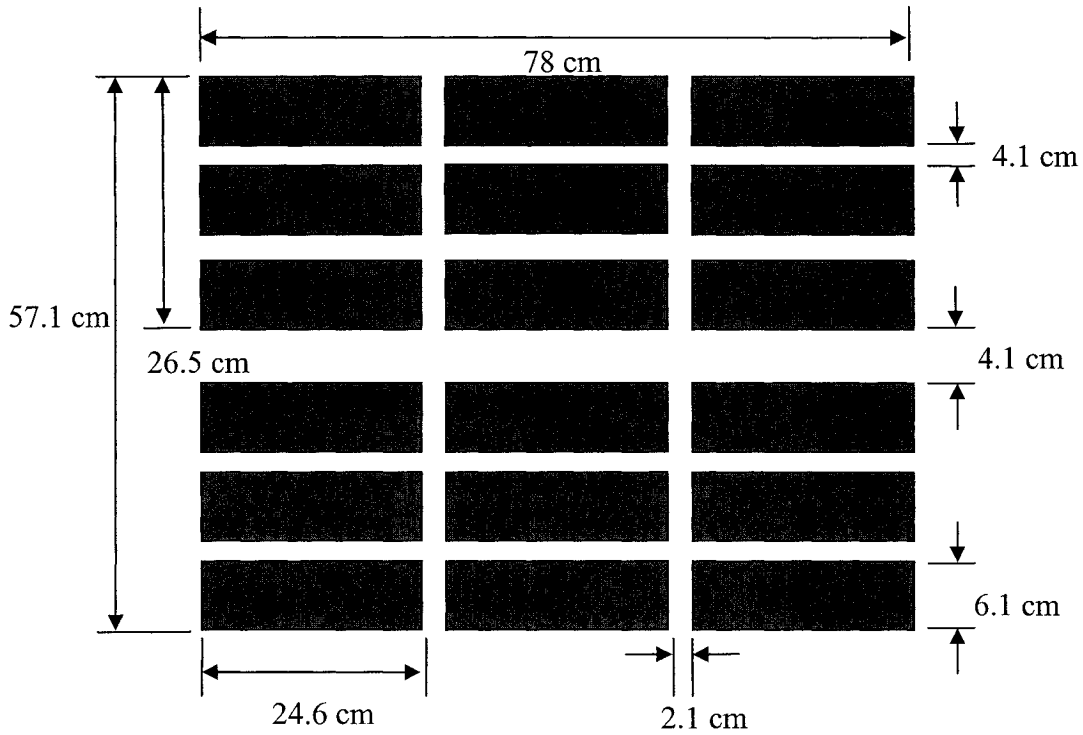


Figure 4-4: Top view of AAA Oven

4.1.2 Existing Control Structure

The central heating element in each zone has an embedded thermocouple. This thermocouple sends a signal to a PID controller, which maintains all three of the heating elements (including the two without thermocouples) in that zone at the given setpoint temperature. Figure 4-5 below shows the LED displays of the PID controllers.



Figure 4-5: PID control panel (for all 12 heater zones)

The PID by definition has a proportional term, an integral term and a derivative term that act upon the signal error. Each of these provides separate adjustments of low frequencies (integral), midfrequencies (proportional), and high frequencies (derivative) [12]. The PID controller equation is given below:

$$G_c(s) = k\left(1 + \frac{1}{T_I s} + T_D s\right) \quad (4.1)$$

Here k is the proportional gain, T_I is the integral time, and T_D is the derivative time. The PID then activates a SSR (solid-state relay), if necessary, which closes the high-voltage loop and sends current to the heating elements, thereby increasing their embedded temperature. The simplified control circuit diagram can be seen in the schematic below.

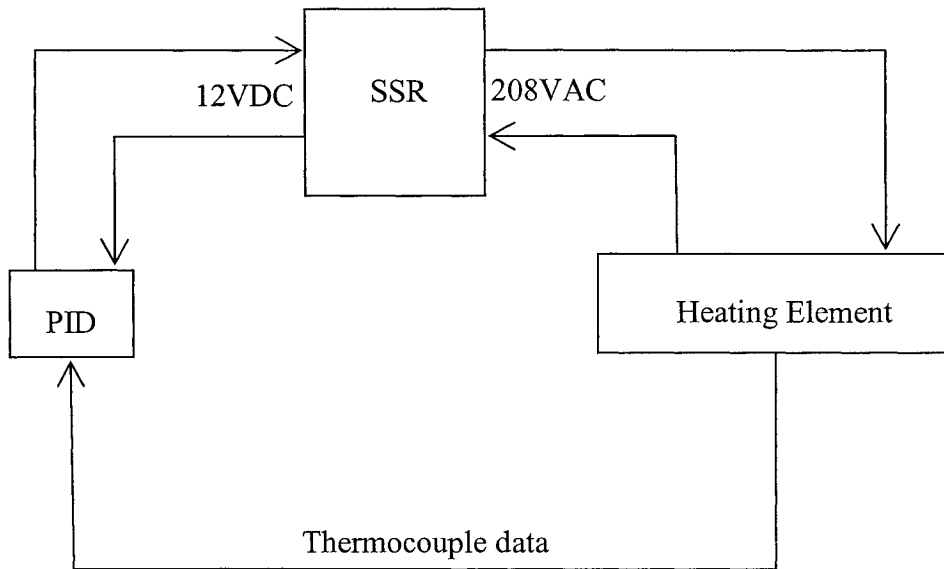


Figure 4-6: PID Control Loop

The PID was set to a 3 second duty cycle. When the pulsed output of the PID was high, or 12V, the SSR allowed 60Hz AC current to pass to the heating element, increasing its temperature. When the pulsed output was low, the SSR remained open, preventing the passage of current to the heating element. The magnitude of the current passing through the heating elements was approximately 8 Amperes. This magnitude did not depend on the length of duty cycle.

4.1.2.1 Modeling the actuators

After developing the sheet model in the previous chapter, the next step was to develop a relationship between the input power and the heating element temperatures. This relationship would provide the final piece to the global transfer function relating the input power to the sheet surface temperature.

The heating element transfer function was determined by open-loop testing. The PID was placed in manual mode, and the input was changed from a temperature setpoint to a percentage of duty cycle. The magnitude of the step input corresponding to the length of the duty cycle can be determined from the following relation:

$$\text{mag}(\text{Step}) = \text{mag}(\text{pulse}) * \frac{\text{duty}}{100} \quad (4.2)$$

Given that the pulsed current magnitude was ~8A, the magnitude of the step was simply calculated according to the equation above. From there it is easy to transform the step input into an input power, simply by multiplying the step current magnitude by the input voltage of 208VAC. Zones B2, B5, T2 and T5 were tested in manual mode, for several different duty cycles. The objective of these tests was to determine the reaction of the heating element to differences in input power, at different locations (interior and surface).

4.1.2.1.1 Test setup

Two measurements were taken, one from the embedded thermocouple located inside the heating element (the same one the PID used as input), and the other from a Raytek Thermalert™ SX Infrared sensor, capable of measuring temperature without contacting the sheet. Using a smooth, polished mirror (with no losses due to reflectivity as measured by another Raytek instrument - the Raytek MX2 portable non-contact IR thermometer), the Raytek Thermalert™ sensor was pointed directly at the centre of the heating element in order to measure its surface temperature. The data was collected using the OPAL-RT real-time system (see section 4.1.4).

4.1.2.1.2 Experimental results

Figure 4-7 shows the evolution of the embedded and surface temperatures for zone B2 with a 10% duty cycle.

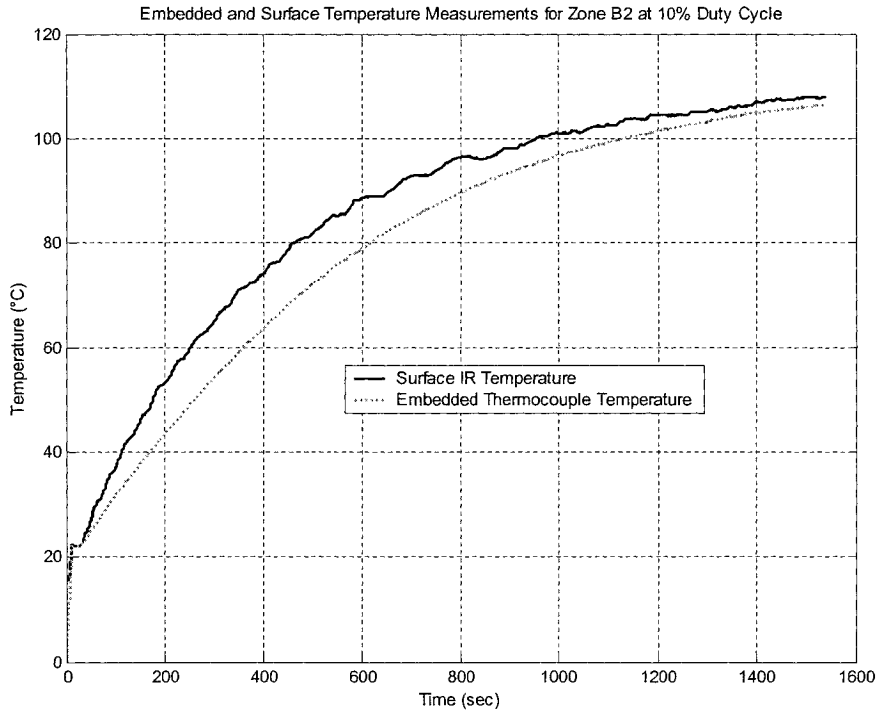


Figure 4-7: B2 Embedded Thermocouple Temperature – 10% Duty Cycle

Each curve displays the characteristics of a first-order transfer function. Any first order system can be described completely using two parameters [12]: the steady-state gain K , and the time constant τ . The equation is shown below, in relation to this system:

$$\frac{\text{Temperature}}{\text{Duty Cycle}} = \frac{K}{\tau s + 1} \quad (4.3)$$

Table 4-1 lists the parameters for B2 for several different duty cycles.

Table 4-1: B2 parameters for several duty cycles

Step	<i>Surface</i>		<i>Embedded</i>	
	τ	K	τ	K
0-10%	415.43	8.75	498.68	8.58
0-20%	380.53	7.40	450.91	7.36
0-40%	297.79	5.84	361.76	5.9
0-60%	277.09	5.02	336.68	5.2
0-100%	244.04	3.93	293.5	4.17

Note that the time constants in each case were very long, over 400 seconds in some cases.

This is a known property of ceramic heating elements, and there are other types that react more quickly (quartz, halogen) [8]. It was beyond the scope of this project to integrate different heating elements than those that were already installed in the AAA machine.

However, it is to be noted that the heating element would never be operated in open-loop conditions for it would take far too long to heat a sheet to the forming temperature.

Therefore, it makes more sense to look at the final entry of the table, where the duty cycle is 100%. Essentially, this means that the current is always passing through the element, which mimics the initial heating much more closely. Also, the steady-state gain values for each case were not the same, as the embedded thermocouple is not the same distance from the wire inside the ceramic as the surface measurement.

It is apparent in all cases that the steady-state gain K and time constant τ depend on the

input power, which increases the complexity of the heating element model. Using best-fit 2nd-order polynomial functions to represent the variation of K and τ with respect to the duty cycle, the next step is to try to model the PID to demonstrate how difficult it is to tune the model to the real system. The results for a step from room temperature to 210°C are shown in Figure 4-8 below.

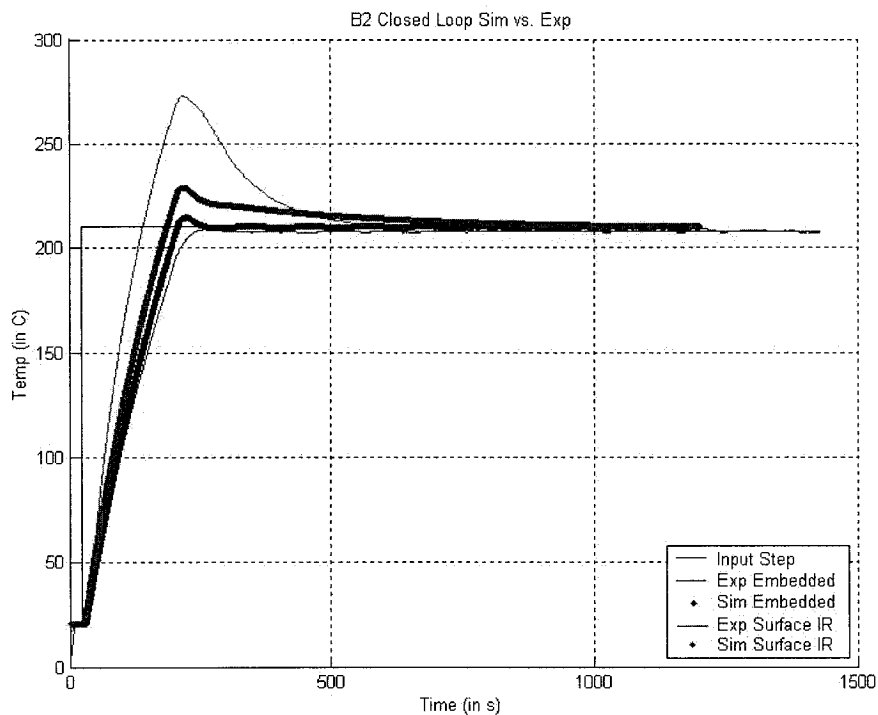


Figure 4-8: Closed-Loop PID model vs. Actual data

The thinner lines represent the experimental data, and the thicker ones represent the results of the simulation. There is a large overshoot in the surface temperature, that the model was incapable of reproducing. Similarly, the settling time for the surface temperature is much longer for the simulation than for the actual data.

For all these reasons, it was determined that the PID should be eliminated from the model altogether. But some way of controlling the surface temperature of the heater must be

maintained if there is to be any sheet temperature control at all. The complete control solution is described in section 4.2.

4.1.2.2 Actuator Heating/Cooling Rate

Another test was performed to determine the heating and cooling rates of only the embedded thermocouple. This gives a more accurate idea of how quickly the heating element reacts to the current at typical operating conditions, both for heating and cooling. For this test, the PID in manual mode was set to 100% of the duty cycle to mimic maximum heating, and set to 0% to mimic maximum cooling. Figure 4-9 below shows the resulting heating and cooling curves for the embedded thermocouple within the heating element:

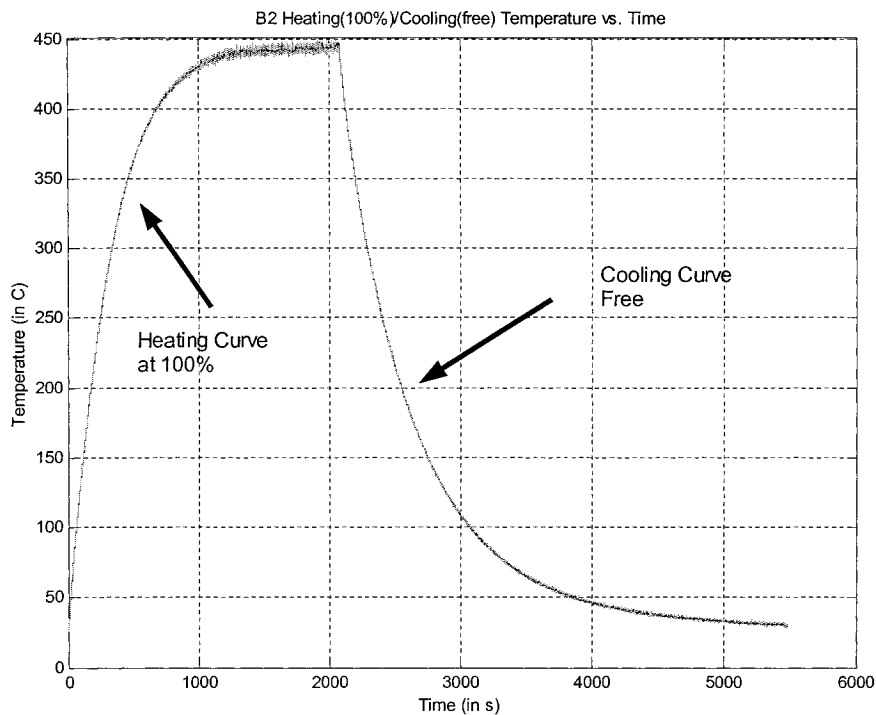


Figure 4-9: B2 Heating (100%) and Cooling (free) Curves

These curves are broken down further in the following table.

Table 4-2: Heating and Cooling Rates for zone B2

HEATING (100%)		COOLING (Free)	
Temperature (°C)	Heating Rate (°C/s)	Temperature (°C)	Cooling Rate (°C/s)
27.9	1.36	445	0.96
50	1.17	400	0.67
100	0.95	350	0.55
150	0.82	300	0.44
200	0.71	250	0.35
250	0.55	200	0.25
300	0.40	150	0.16
350	0.23	100	0.06
400	N/A	50	N/A

The heating rates are greater than the cooling rates as expected. Cooling is done by free convection, which is a natural process, and therefore much slower than the heating, which is an active process. This phenomenon will have important effects on the controller designs.

4.1.3 Infrared Sensors

In order to control the plastic sheet surface temperature, a non-contact method of measuring the surface temperature must be used. If a contact method of measuring

temperature, like a thermocouple, were used, there could be sheet degradation at the point of contact due to conduction. Infrared sensors are also capable of measuring higher temperatures than contact thermocouples, at a faster rate as well.

The infrared thermometer can be compared to a human eye. The lens of the eye can be seen as the optics through which the radiation from the object reaches the retina, or detector, through the atmosphere [29]. Every object radiates infrared energy along a given wavelength due to its temperature. The wavelength-dependent emissivity affects the amount of energy seen by the IR detector, as discussed in the previous chapter. Therefore, an emissivity value needs to be input into the IR sensor before accurate measurements can be taken. In this case, the IR sensors will be evaluating the surface temperatures of a plastic sheet. The emissivity of plastic is given as approximately 0.95 (see Table 3-3).

The Raytek Thermalert® MIC™ Miniature Infrared Sensors must be operated within a certain ambient temperature range. If they are used outside of this range (25-85°C) without some form of cooling, they may become damaged and their measurement precision may suffer. Observing Figure 4-10 below, the small cylindrical shaped sensor can be seen at one end, and the square electronics housing at the other. The two pieces are connected by an insulating tube, which protects the sensor from overheating. Cool air is pumped into the tube to maintain the operating temperature of the sensors within the desired range.

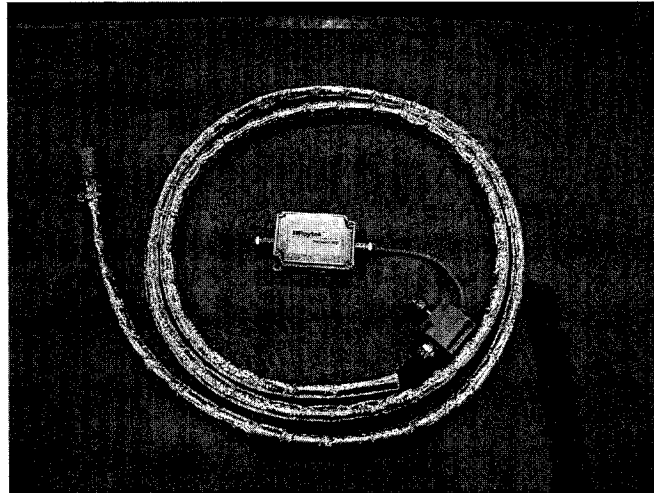


Figure 4-10: Raytek Thermalert® MIC™ IR sensor with cooling jacket

4.1.3.1 Distance to Spot Ratio

The optical detector receives the focused infrared energy of a circular measurement spot on the object whose temperature is being measured. The optical resolution of the sensor is defined as the ratio of the distance D of the object to the sensor with respect to the size S of the optical spot [27]. Figure 4-11 gives an idea of two different $D : S$ ratios:

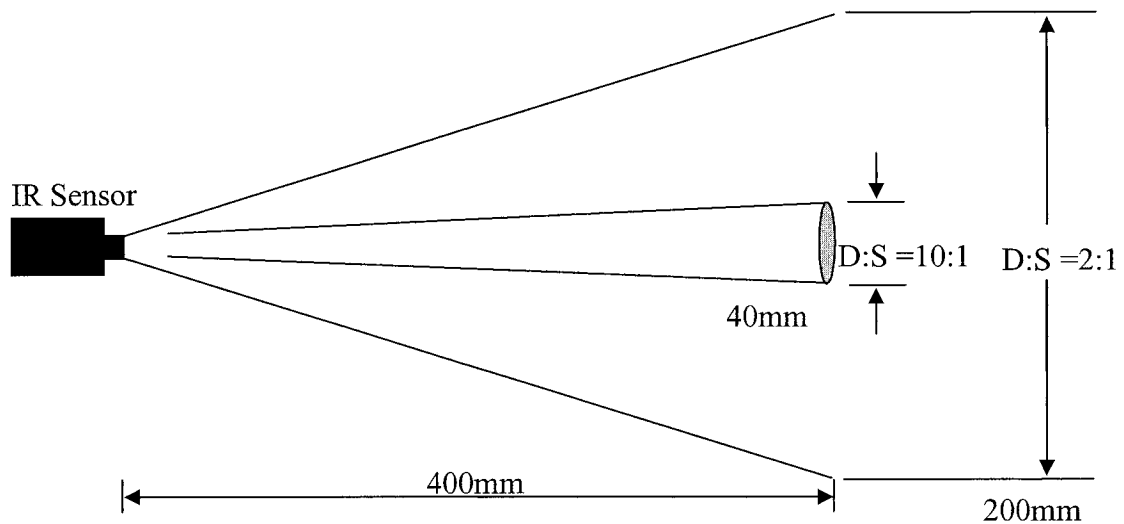


Figure 4-11: Examples of different $D : S$ ratios

The Raytek Thermalert® MIC™ Miniature Infrared Sensors used in the AAA thermoforming oven at CNRC-NRC IMI have a $D : S$ ratio of 10. This means that since they are all approximately placed 15-18cm away from the plastic sheet, each sensor measures a circular area on the sheet surface with diameter 1.5-1.8cm.

4.1.3.2 IR Sensor Locations

If each IR sensor measures an area of $1.76-2.54\text{cm}^2$ (from above section), then it would require more than 350 sensors to measure one side of a 30cm by 30cm sheet. Obviously, this is not practical. Therefore, the following sensor arrangement was chosen. In Figure 4-12 below, the star shapes represent the locations of the IR sensors with respect to the heating elements. There are 7 IR sensors per tray, and 14 in all.

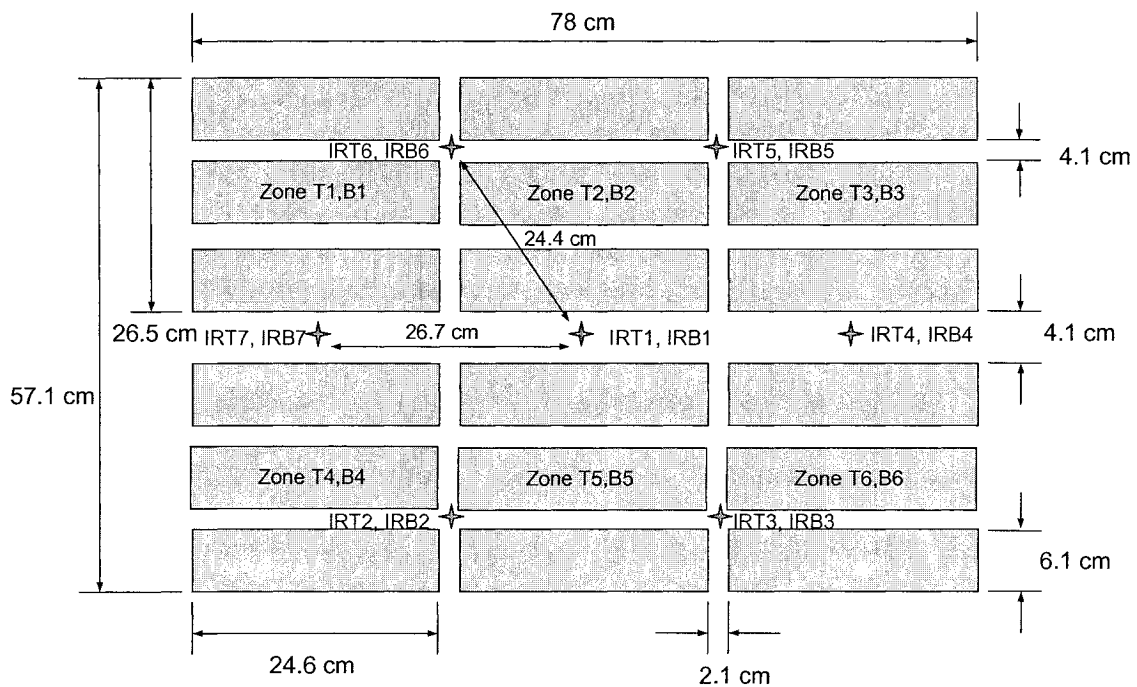


Figure 4-12: Top view of AAA oven with IR sensors

For the upper heater bank, the centre IR sensor is labeled T1, and the front right one T2. The others are labeled in a counter-clockwise manner up to T7. Similar notation is used for the lower bank, starting with B1 in the centre. Note that for all of the development done in this thesis only T1, B1, T2 and T3 were present.

4.1.4 OPAL-RT RT-LAB Operating System

The OPAL-RT RT-LAB software package makes real-time control of the thermoforming process possible. The main purpose of this software is to allow the user to design a high-level controller using MATLAB Simulink or some other design tool, and incorporating this controller directly to the hardware without having to code by hand. In this way, the key to developing real-time simulation success becomes the advanced simulation and modeling algorithms. Consequently, it becomes feasible to use the control system model as an embedded controller for the industrial real-time process.

4.1.4.1 RT-LAB system structure

The RT-LAB software runs on a hardware package of the following items: Command Station, Compilation node, Target nodes, the communication links (real-time FireWire and Ethernet), and the I/O boards.

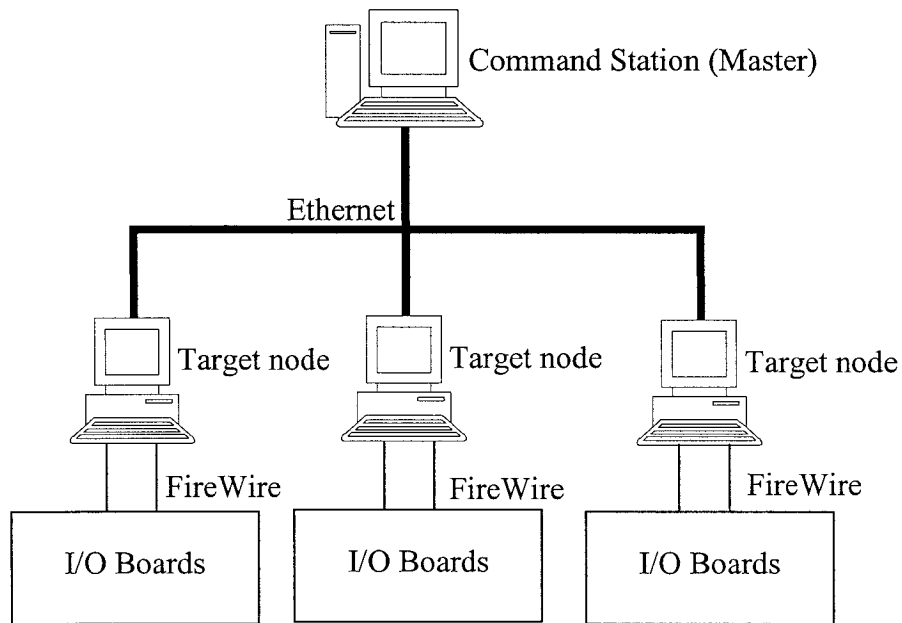


Figure 4-13: RT-LAB Hardware Package

Figure 4-13 gives an example of a typical system representation. This system is comprised of one Command Station, and three target nodes (one of which is designated the compilation node).

The Command Station is a PC workstation that uses Windows 2000 as its operating system, and serves as the user interface. It permits the user to do the following tasks: edit and modify models, run original software simulations of the model, generate and separate code, and control the parameters of the RT-LAB simulation [30].

The target nodes use QNX as their preferred operating system for real-time simulation. Ethernet cables are used to connect the target nodes to the Command Station. The target nodes are communication and real-time processing computers dedicated to the following tasks: real-time execution of the simulation, real-time communication with the I/O devices, initialization and synchronization of the I/O devices, data acquisition from I/O

devices, and data recording. The FireWire link permits communication with the I/O devices.

One of the target nodes must double as the compilation node; in other words, it must first debug the user's source code, then compile the C code, and finally load it onto the target node before operation.

The I/O boards are used to send and receive data from the model to the hardware in the system, namely the system inputs (the sensors) and the system outputs (the actuators).

At CNRC-NRC IMI, the system is simple; there is only one target node, which doubles as the compilation node, and one Command Station.

4.1.4.1.1 System Inputs

The inputs to the target node, then, are the sensor outputs. Each sensor output is connected to a differential channel of an Acromag IP320 12-bit Analog/Digital Converter (A/D). Each card has 20 differential, or 40 single-ended channels. Each channel is capable of converting an input of 0-10VDC into a 12-bit digital signal. In other words, the signal has a resolution of 0.0025V per bit.

The input signals to the RT-LAB system are IR sensor sheet temperature measurements, the ambient temperatures of the IR sensors themselves, the signal indicating sheet entry into the oven and finally, the embedded thermocouple temperature measurements from the heating elements. Some of these inputs do not however have an output voltage that corresponds to the 0-10VDC range required by the A/D. The embedded thermocouples output a voltage that is of the order of milliVolts, which require some signal conditioning (i.e., amplification) before they are input to the A/D. The signal conditioners from

Analog Devices are shown in Figure 4-14:

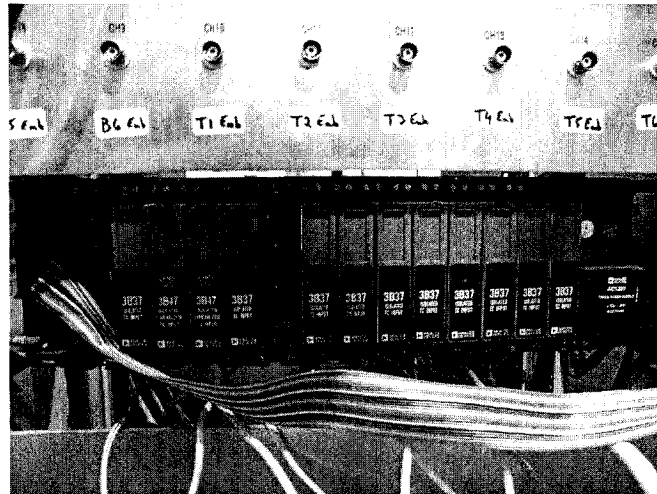


Figure 4-14: Thermocouple signal conditioners from Analog Devices (3B37, 3B47)

The 3B47 takes the thermocouple input signal, which has a range of 0-500°C, and converts it into a 0-10V signal. The 3B37 converts a thermocouple input range of -100-1350°C into a 0-10V signal. Consequently, each of these will have a different gain and offset that will need to be incorporated into the RT-LAB model.

The outputs of the Thermalert MID IR sensors are in the 0-5VDC range. The IR sensor has a temperature range of 0-500°C as well. The gain in this case is 10mV/°C. It was determined that conditioning was not necessary for these sensors, as the sensors do not need to measure the sheet surface temperature more accurately than 0.1°C, which corresponds to a range of 1mV (or less than 1 bit). Any greater measurement precision is superfluous for thermoforming. Similar logic can be applied to the ambient temperature measurements of the IR sensors, since only approximate (within 1°C) temperatures are required to monitor these inputs in order to avoid overheating.

4.1.4.1.2 System Outputs

The system outputs will be the signals replacing the outputs of the PID. These signals are input to the solid-state relays (SSRs) for each heating zone. The SSRs switch on and off according to their DC input voltage. This voltage is of the range of 4-32VDC. The system outputs its signals through an Acromag IP220 12-bit High-Density Analog Output board (D/A), which takes the signal produced by the RT-LAB software, and converts it into an analog signal recognizable by the SSR. The output range of the D/A is -10 to 10VDC, which is within the input range of the SSR, meaning no additional signal conditioning is necessary.

Note that each of the A/D and D/A cards is connected to the Acromag APC8621 PCI Bus Carrier Board, whose role is to ensure communication between the I/O cards and the RT-LAB software.

4.2 Real-Time Control of Sheet Temperatures

Using the IR sensors installed at different locations within the bank of heating elements, the objective of this section is to demonstrate that simple control algorithms can be used to maintain the plastic sheet (or a reasonable alternative) surface temperatures at a constant level, or even make these temperatures follow a ramp function.

First, the control algorithm will be proposed. The non-linear system (due to the radiative heat transfer term) described above can be simplified to a linear system by directly controlling the temperature instead of the energy.

Second, the multilayer control algorithm will be explained in detail. The system requires

two separate levels of controllers; the inner loop will act directly on the heating elements (performing the same role as the hardware PID, but this time using RT-LAB), and the outer loop on the sheet surface temperatures.

The different types of controllers proposed for controlling the heating elements will be discussed here. The hardware PID from section 4.1.2.1 was replaced with a software version, but due to the slower heating curve, a simple on-off (or “bang-bang”) controller was chosen.

Finally, the control of the sheet surface temperature was achieved with simple PI controllers for each of the sensors. A sensitivity matrix was determined to show the relationship between each heating zone and each IR sensor. Using this matrix, it was determined that the 1st order model for the heating element was not needed, as the sheet temperature reacted 10 times more slowly than the heating element. Consequently, simple 1st order models were obtained for the sheet temperature functions. Simple PI controllers were then designed using these models and tested in real-time on the AAA thermoforming machine. Finally, in order to simulate a more realistic sheet reheat function, temperature ramps were input to the system, and a feed-forward controller with PI was implemented and tested.

4.2.1 Linearizing the sheet reheat system

Since the state-space system representing the energy inside the sheet is non-linear, the controller options become more complicated. Non-linear controllers often must be designed specifically for the system, and cannot be ported over to similar systems very easily. A controller designed for the AAA thermoforming machine at IMI might not

achieve the same results on another thermoforming machine, if these non-linearities are not taken into account. Another source of non-linearity is the heating elements themselves (see Table 4-1 for non-linear gain and time constant functions), but the inner feedback control loop eliminates these potential problems.

For this reason, it makes sense to investigate the error caused by linearizing this system about a given operating point to verify that the approximation does not stray too far from reality. From calculus [11], the linear approximation of a function is given as:

$$f(x) \approx f(x_1) + f'(x_1)(x - x_1) \quad (4.3)$$

Let the operating point in this case be T_{set} , and the function $f(T) = T^4$. Then, using the equation above, the linear approximation becomes:

$$\begin{aligned} T^4 &\approx T_{set}^4 + 4T_{set}^3 \times (T - T_{set}) \\ T^4 &\approx T_{set}^4 + 4T_{set}^3 T - 4T_{set}^4 \\ T^4 &\approx 4T_{set}^3 T - 3T_{set}^4 \end{aligned} \quad (4.4)$$

Noting that the typical forming temperature for an HDPE sheet is within the range of 140-180°C, the operating point is chosen as 160°C. The first figure below represents the radiant energy function (T^4) and its linear approximation, while the second shows the percent error over the entire temperature range (less than 2%).

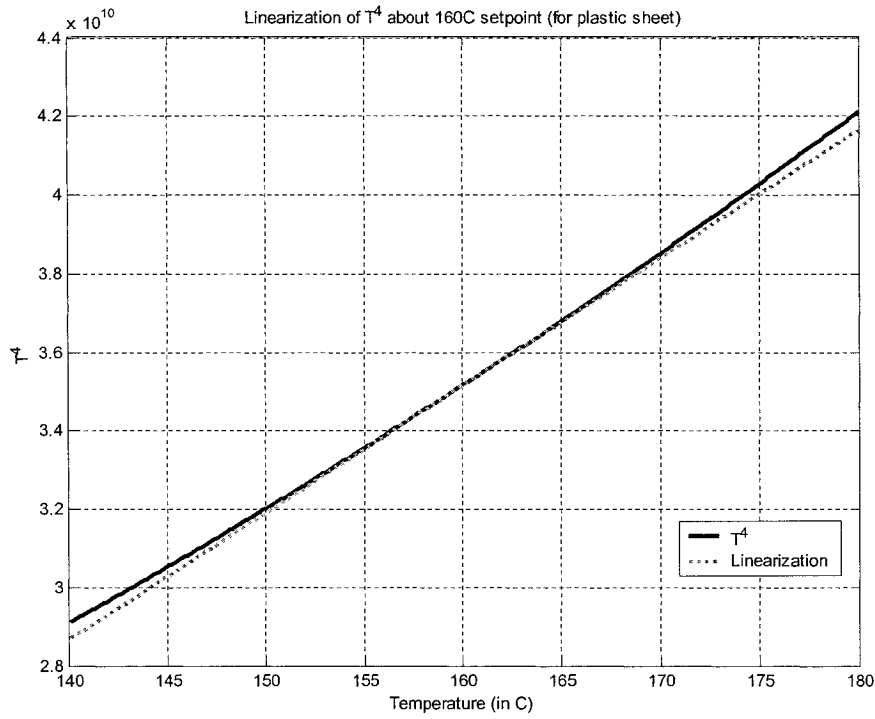


Figure 4-15: Linearization function about 160°C setpoint (for HDPE)

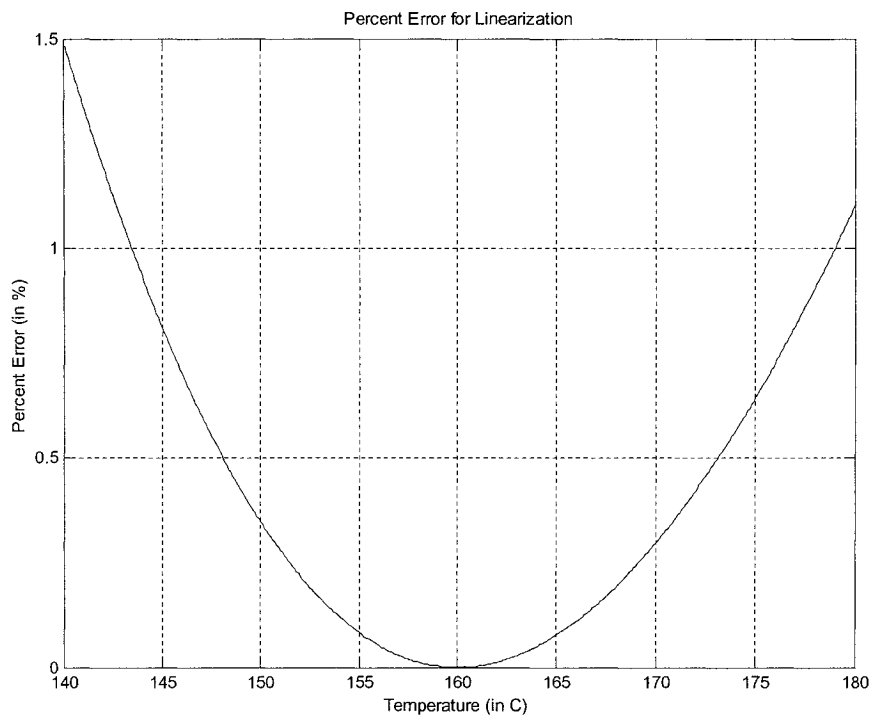


Figure 4-16: Percent error for Linearization over entire HDPE forming range (140-180°C)

The radiant heat transfer function takes the temperature in degrees Kelvin. Logically, the percent error decreases as the operating point is raised. Consequently, the linearization function gives even better results when looking at the surface temperature of the heating elements. The linearizing range was chosen as 300-400°C, with a setpoint of 350°, because the heating element will most likely be operating in this temperature range during the sheet reheat phase. In other words, between sheets, the heating elements will be held at a setpoint somewhere in this range, and will not be permitted to cool down (because of their long heating and cooling times – see Table 4-2).

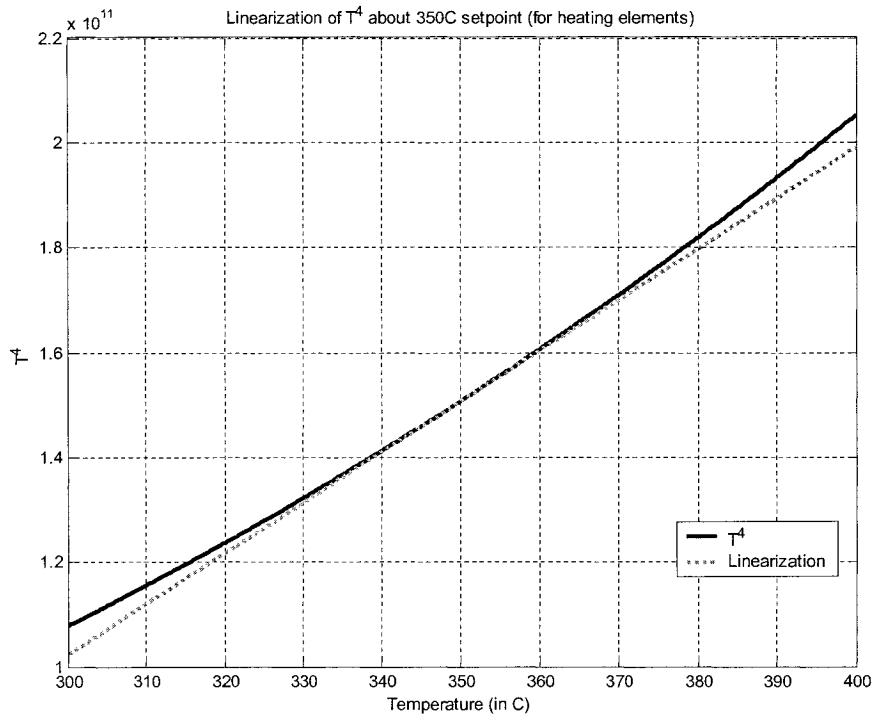


Figure 4-17: Linearization function for 350C setpoint

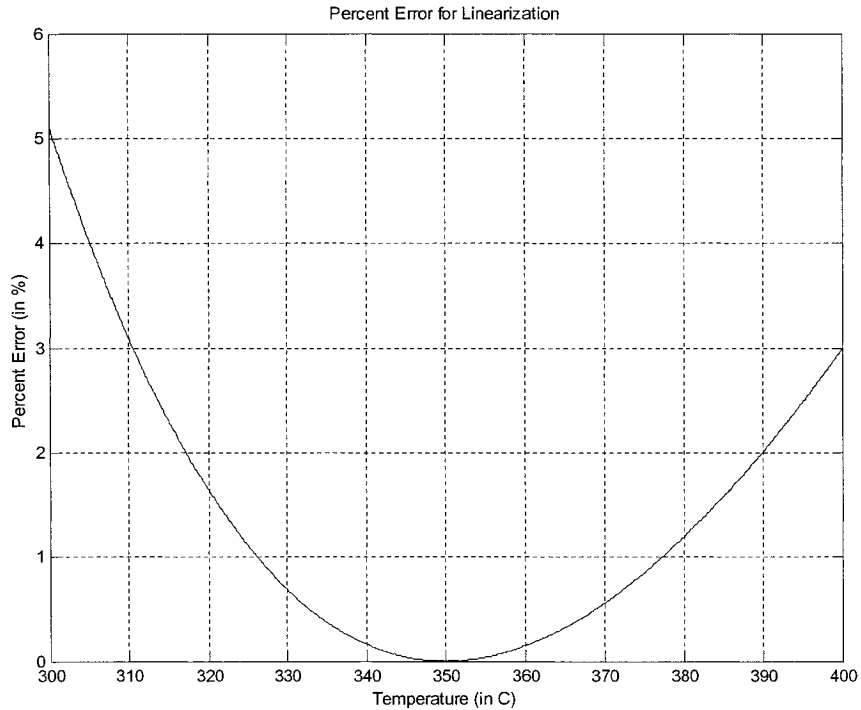


Figure 4-18: Percent Error for linearization over heating element active range (300-400°C)

4.2.2 Control algorithm: multilayer control

The typical thermoforming oven knows only two states: empty (no sheet), or full (sheet). The controller must take this duality into account. When there is a sheet in the oven, the controller acts as it normally would, measuring the sheet surface temperature with the IR sensors, and taking the appropriate action based on the measurement. However, when the sheet is **not** in the oven, the heating elements must be maintained at their predetermined operating points. So the second function of the controller must be to monitor the heating element temperatures, and adjust accordingly as the measurements change.

The controller then must have two layers, or loops. The inner loop maintains the operating point of the heating elements when there is no sheet present in the oven. This loop is shown in Figure 4-19:

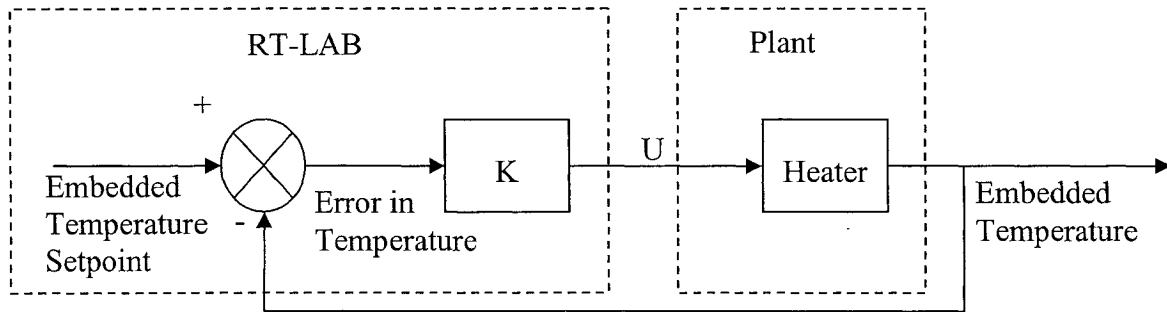


Figure 4-19: Inner Loop Heating Element Control Schematic

For the inner loop control, the controller K (designed in Simulink and running in real-time with RT-LAB) receives the embedded temperatures from each of the 12 heating zones in the plant, compares them to the desired setpoint and reacts accordingly by sending a signal to each zone. Based on the type of controller (bang-bang or PID), the signal has to be of a certain shape. This will be explained further in section 4.2.3.

The outer loop controller is more complicated, as can be noted in the block diagram of Figure 4-20:

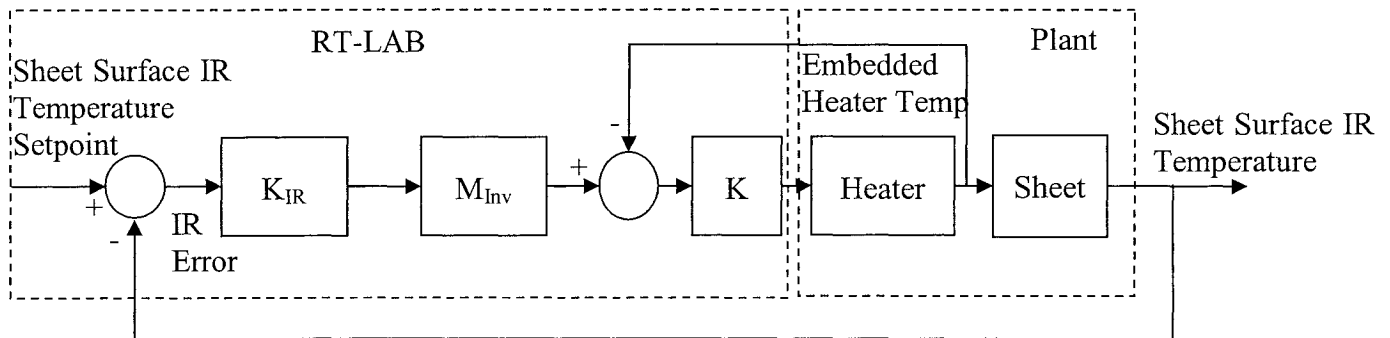


Figure 4-20: Outer Loop Controller Block Diagram

For this loop, the infrared temperature measurements on the plastic are being monitored and compared to their setpoints. The error signal is then sent into the sheet surface

temperature controller K_{IR} above. The design of this controller is covered in sections 4.2.4.3 and 4.2.4.4 below. The M_{INV} block represents the inverted steady-state gain matrix between the heating elements and the sheet temperatures (see section 4.2.4.2). The M_{INV} block is a decoupler, separating each of the IR temperature signals into 12 distinct embedded heating element temperatures. The M_{INV} block receives the output of K_{IR} , which is the new desired infrared setpoint, which is then converted by M_{INV} into the new heating element setpoints. These new setpoints are input to the inner loop controller K , which control the individual heating elements. Eventually, the sheet temperatures are adjusted, and the cycle then repeats. The RT-LAB system is running at a sampling rate of 0.1s; in other words, there are 10 sets of measurements and calculations per second.

4.2.3 Inner loop Control: Embedded Heating Element Temperatures

In the modeling section above, several reasons were given for replacing the hardware PID. The three gain parameters increase the order of the system by two, and create more state equations. To limit the number of states within the model, the decision was made to replace the heating element PID controllers with a software version.

Two types of controllers were implemented and tested for the heating elements: a combination feed forward-PI controller, and a simple on-off or bang-bang controller. The simpler controller was selected, because it reacted more quickly to the heating element dynamics (namely the different heating and cooling rates), as will be demonstrated.

4.2.3.1 Hybrid Feedforward-PID controller

The first controller designed to monitor the embedded heating element temperature was essentially a software version of the existing hardware one. The thermocouple outputs were sent to signal conditioners, so that the A/D card could digitize their values as described above. Consequently, these signals were then reconverted into °C, with small offset and calibration gains. The signal output block diagrams for the Analog Devices 3B37 and 3B47 are seen in Figure 4-21 and Figure 4-22:

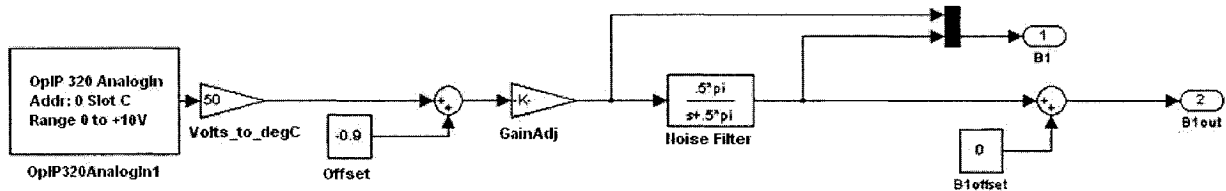


Figure 4-21: Signal input from Analog Devices 3B37 Signal Conditioner

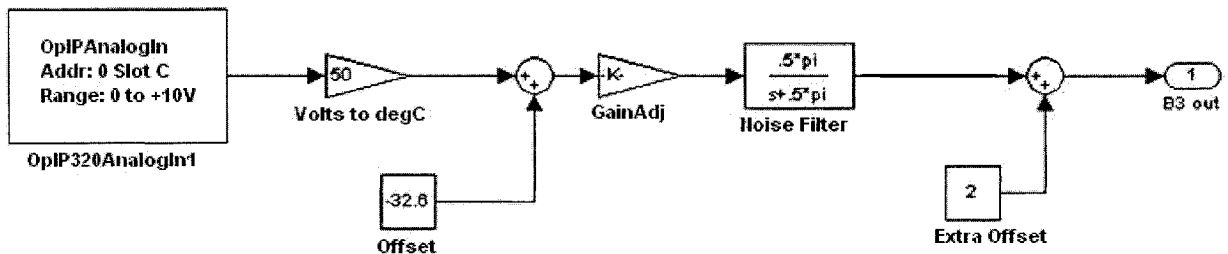


Figure 4-22: Signal input from Analog Devices 3B47 Signal Conditioner

The calibration offset and gain for the 3B37 are much smaller than their counterparts for the 3B47. The input temperature range for the 3B37 is 0-500°C, whereas for the 3B47, the range is much larger (from -100°C to 1350°C). Calibration was performed using an Omega Model CL23 Type J-K-T thermocouple calibrator at a setpoint of 300°C. The adjusted gain K for the 3B37 was 300/302.6, or close to 1, whereas the adjusted gain K

for the 3B47 was 300/106.5. The D/A output however was highly prone to noise, especially once the amplifications from mV to V to °C had been done. In each case, a gain of at least 10 was applied to the signal plus its noisy counterpart. With a sampling time of 0.1 seconds, a low pass filter was needed to eliminate the noise problem. The transfer function for this filter in the frequency domain is given below [13]:

$$\frac{V_o}{V_i} = \frac{1}{1 + sRC} \quad (4.5)$$

The cutoff frequency for the lowpass filter is $f = \frac{1}{2\pi RC} \text{ Hz}$.

This filter was first attempted in hardware, with large capacitors and resistances, but did not have a major effect other than to slow down the system response. Therefore a software version was implemented in Simulink, with a cutoff frequency of 0.25Hz. The effect of this filter can be seen in Figure 4-23:

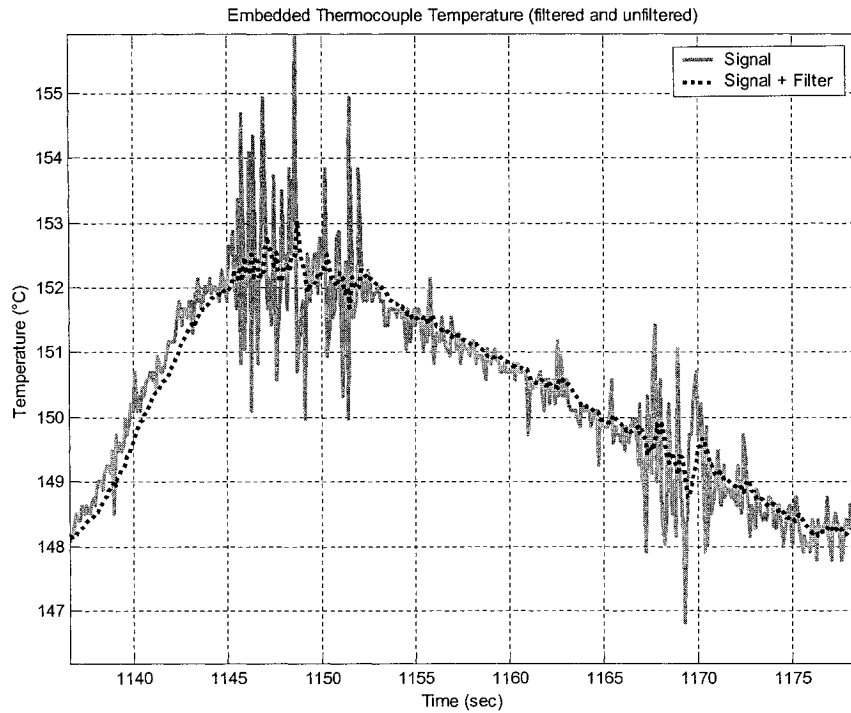


Figure 4-23: Filtered and Unfiltered embedded thermocouple signal

The signal noise is diminished by 2-3°C in some cases, which greatly improves the reaction of the controller, as it will be less prone to act on erroneous signals. The delay caused by the filter is approximately 2 seconds. The delay only affects the start of the heating curve (shown in Figure 4-24). Therefore, the effect of the delay on the heater response is minimized after startup.

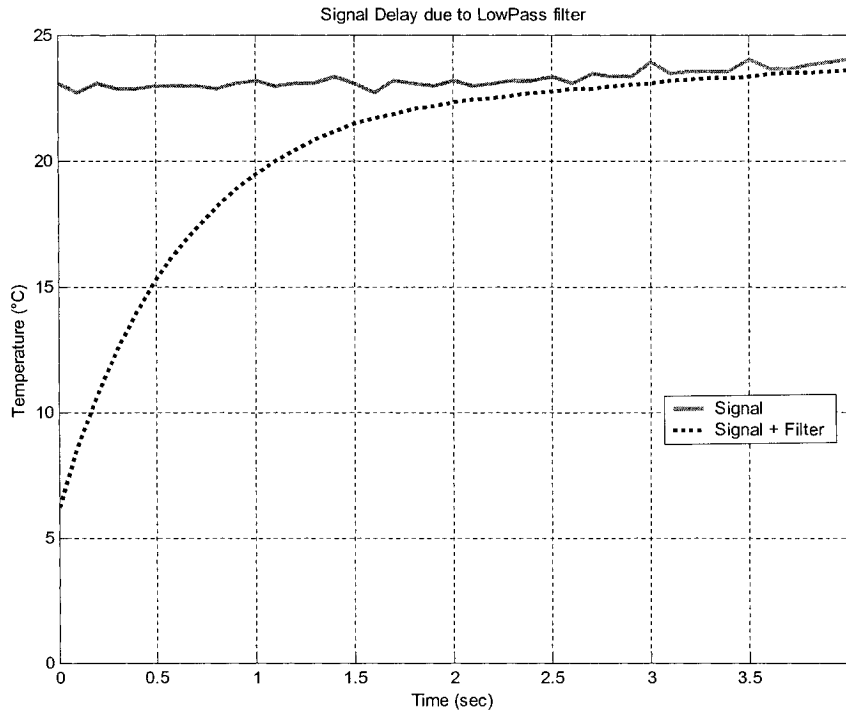


Figure 4-24: Signal delay due to low pass filter

The final offset block is simply added so that the display outputs on the PID bank all corresponded to the desired test setpoint of 150°C.

The feedforward control is a direct control of the reference signal. It can even be viewed as open-loop control. The feedforward path is used in this model simply to push the controller in the right direction at startup. Similarly, the velocity and acceleration terms are also feedforward or open-loop terms. These terms are there to test whether the controller can make the heating element follow a ramp or sinusoidal input.

The PI controller, however, works on the error signal, which is created by comparing the actual temperature measurement with the desired setpoint. The proportional gain simply acts upon this error signal, whereas the integral gain takes the sum of the error signal over time, and then corrects the steady-state or offset errors. The derivative term is not used, as

its primary use is to speed up the step response of the system. Since the dynamics of the heating element limit the speed of the response, the effect of increasing the derivative gain will be minimal.

The block diagram describing this controller is seen in Figure 4-25:

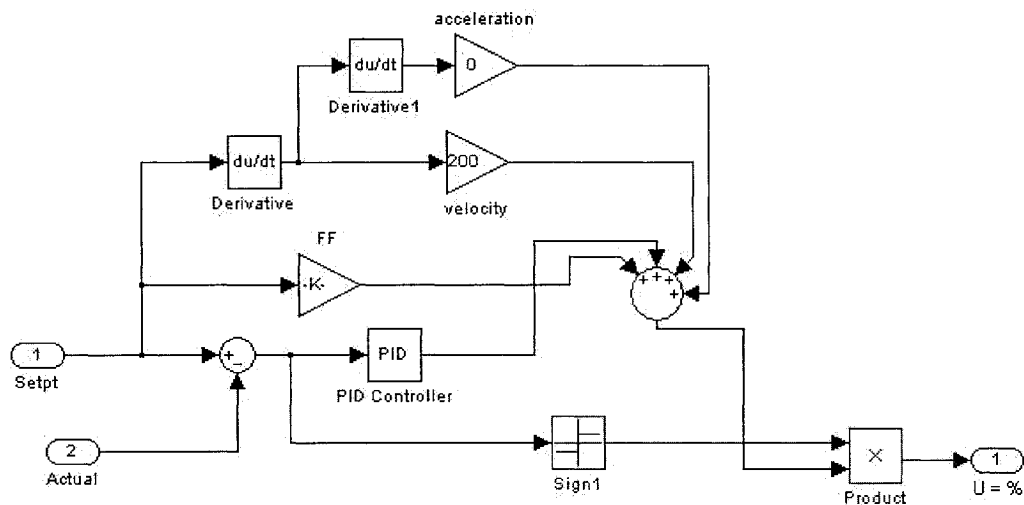


Figure 4-25: Hybrid Feedforward PID controller

The output of the hardware PID was a simple square wave signal with a period of 3 seconds. The hardware PID controlled the length of the duty cycle of the square wave which was then input to the SSR. Therefore the output u , if the hardware PID was to be completely replaced, needed to be a duty cycle percentage. Using Simulink, a square wave output was created (see Figure 4-26 below) from the percentage input. Since the sampling rate of 0.1 seconds was much higher than the 3 second PID period, the output u was changing much more quickly than the PID could react. In this way, only every 30th calculation of u was sent to the SSR. The saturation block is there to limit the input percentage to no more than 100% of the duty cycle (full heating) and no less than

0% (free cooling).

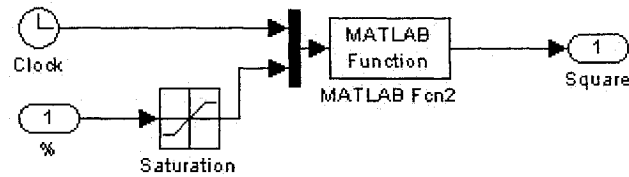


Figure 4-26: Square Wave Function

This controller was first used normally, acting on both positive and negative errors. The positive error case indicates that the actual temperature is less than the desired temperature. So the action that should be taken is to increase the energy going to the system, and to increase the actual temperature to reach the setpoint. For the negative case, the actual temperature is greater than the desired temperature. The controller reaction is to decrease the heating element temperature. Free convection is the only way for the heating element to cool down. As seen above in Table 4-2, the cooling rates for the heating element are smaller than the heating rates. However, the PID in this case is not shut off, and begins to accumulate negative error in the integral term because of the overshoot. Therefore, when the temperature drops down below the setpoint again due to cooling, it continues to drop, instead of increasing as expected. The PID now needs to accumulate positive error to eliminate all the negative error accumulated when the temperature was too high, before it can push the heating element in the right direction.

For this reason, the sign block and product block at the bottom of Figure 4-25 are present to shut off the PID when the temperature is too high (i.e., when the error is negative). Like the signum function, the sign block outputs 1 if its input is positive, -1 if its input is negative, and 0 if its input is 0. The combined output of the feedforward and PID terms is

equal to the new heating element setpoint, which is always positive. Therefore, the product block in Figure 4-25 will always output a negative value if the heating element is above its setpoint. This negative value is cut off by the saturator block in Figure 4-26, since there can be no negative duty cycle.

So, in effect the feedforward-PID controller acts in a one-sided manner, controlling only the heating, and letting the system cool via convection. Figure 4-27 below shows the reaction of the heater embedded temperature as the PID reaches various setpoints.

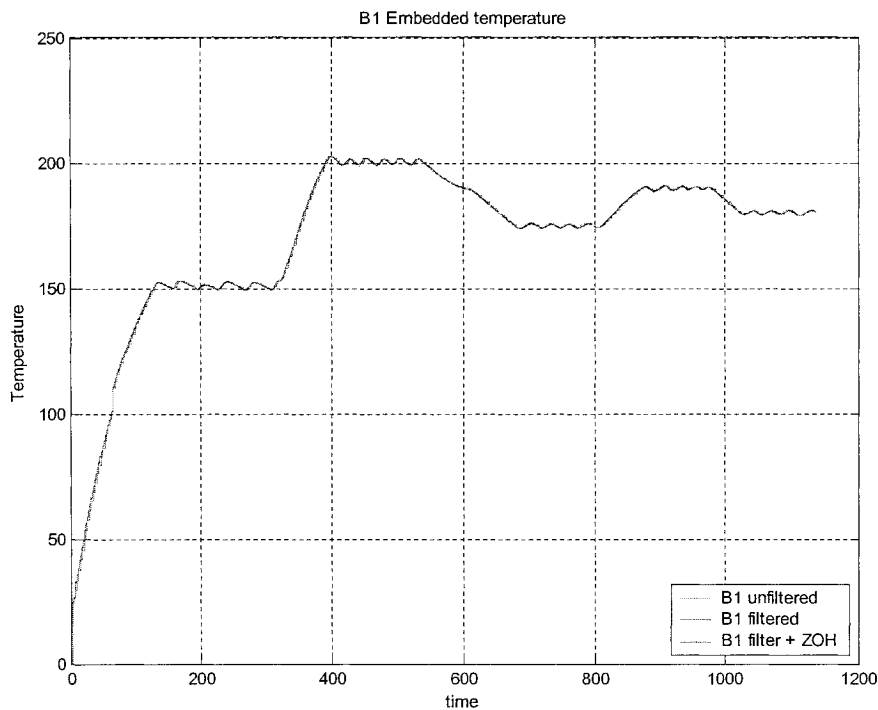


Figure 4-27: Embedded Thermocouple reaction to various PID setpoints (zone B1)

Note that all curves are on top of one another in this figure. The first setpoint is 150°C, which is reached after approximately 100 seconds. Note that the heating element oscillates about the setpoint because the heating and cooling rates are not the same. Once the error becomes positive (setpoint greater than actual), the SSR is closed and allows the

current to pass instantaneously, increasing the actual temperature almost as quickly. But, it must wait the full 3 seconds before obtaining the next input, in which time the heating element temperature can increase 2.5°C (from Table 4-2). After which, it will take at least 15 seconds to drop by that much afterwards.

Another cause of these oscillations is the proximity of the embedded thermocouple to the resistance coil within the heating element. A cross section of the heating element can be seen in the figure below:

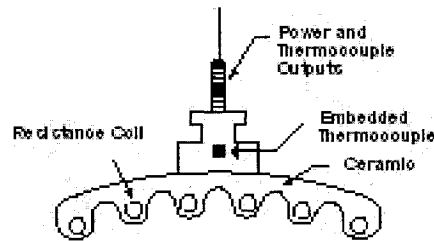


Figure 4-28: Cross section of ceramic heating element

The distance between the embedded thermocouple and the resistance coil is large enough to cause a delay between the closing of the SSR and the first measured increase in embedded temperature, due to the slow conduction heat transfer within the ceramic. The magnitude of the delay is between 4-10 seconds depending on the heating element. An example of the delay is shown in Figure 4-29:

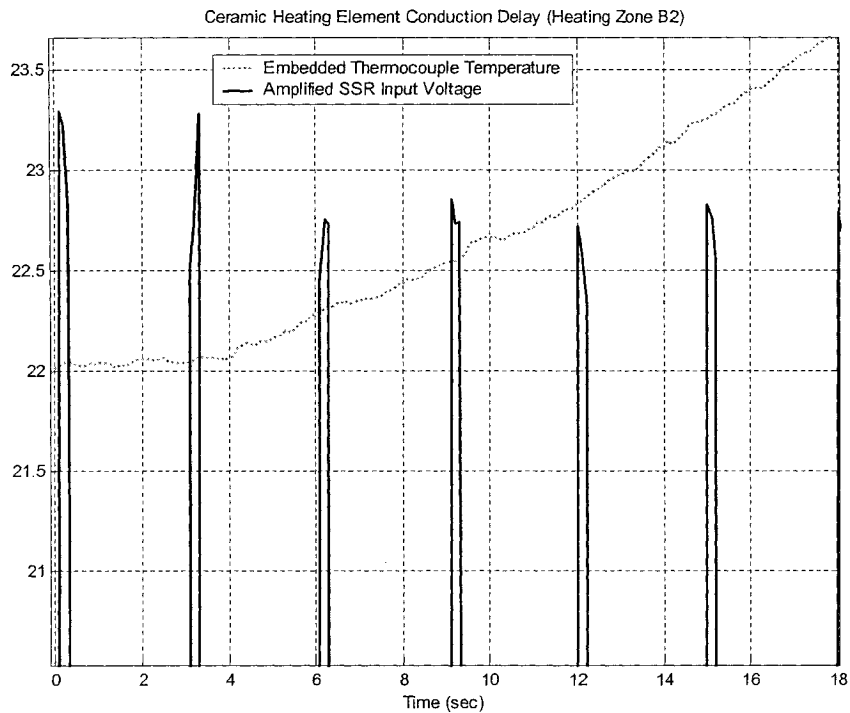


Figure 4-29: Ceramic Heating element Conduction Delay (Heating Zone B2)

Note that the amplified SSR voltage input (solid line) starts at 0s. This voltage is applied for 0.3 seconds, or 10% of the 3-second duty cycle. Approximately 4 seconds pass before the embedded thermocouple temperature (dotted line) begins to increase. So the approximate conduction delay is 4 seconds at startup. This delay is characteristic of the ceramic heating element, and there is no way to eliminate or improve it, short of changing to quartz or halogen heating elements.

The oscillation of the heater temperature about the setpoint does not have a great effect on the sheet temperature, however. The sheet surface temperatures at steady-state are very stable.

4.2.3.2 On-off or Bang-Bang Control

The next controller implemented and tested is much simpler than the one-sided feedforward PID. Since the cooling phase is not controllable, a bang-bang or on-off controller is the easiest way to regulate the embedded heating element temperature. The block diagram is shown in Figure 4-30:

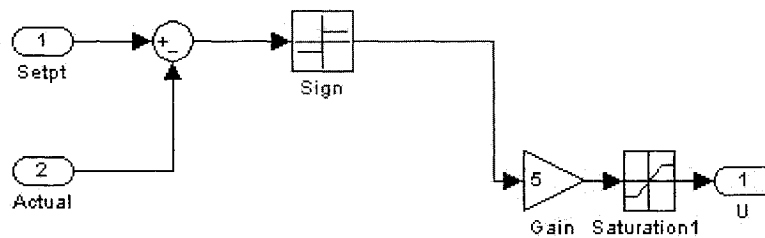


Figure 4-30: Block Diagram of Bang-Bang Inner Loop Controller

When the error is positive, the sign block outputs a 1 which is multiplied by the gain block, and then saturated. The output u is directly connected to the SSR, without the need for the three second duty cycle. In this way, the system can respond much faster to a change in actual temperature. When the error is negative (i.e. heater is cooling down), the sign block outputs -1. This signal is then multiplied and saturated to 0, indicating that the SSR should remain open and prevent current from flowing to the heating element. The conduction delay is still present, causing the oscillations seen in Figure 4-31:

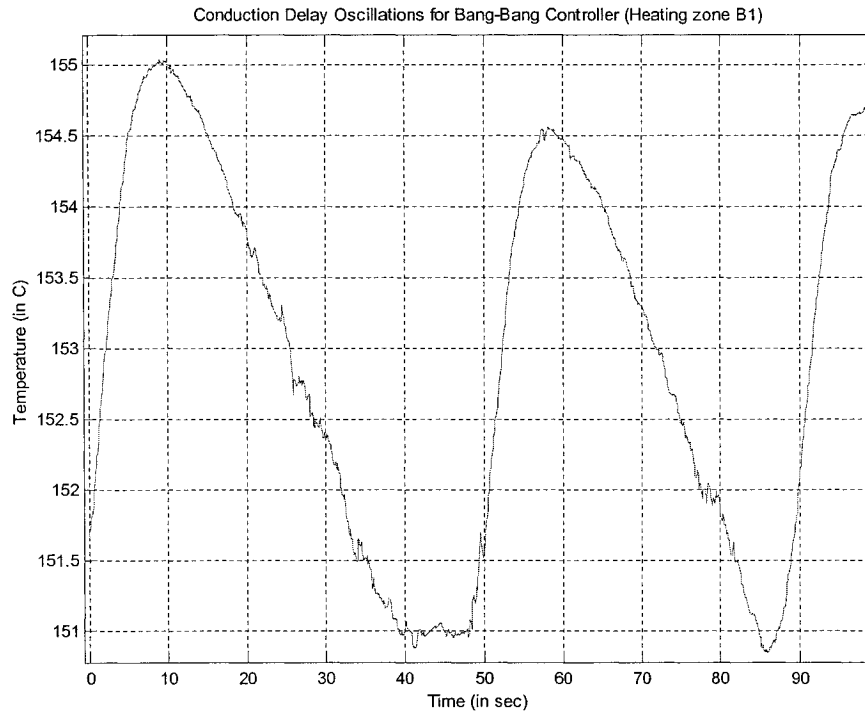


Figure 4-31: Conduction Delay Oscillations for Bang-Bang Controller (zone B1)

The bang-bang controller was selected for use in the inner control loop because of its simplicity and speed of response. The one-sided PID did not react as quickly after the heating element entered its first cooling phase, because of the building of negative error in the integral term. The bang-bang controller minimizes the effect of the conduction delay within the ceramic. After implementing one bang-bang controller per heating zone for a total of 12, the IR control is now ready to be studied.

4.2.4 Outer loop Control: Sheet Surface Temperatures using IR

The outer loop control algorithm was shown in Figure 4-20 above. First, the outputs of the infrared sensors must be conditioned. In order to control the sheet surface temperatures, the steady-state relationship between the heating element temperatures and the surface temperatures at different locations on the sheet must be determined. Then, using this gain matrix, a first-order model of the sheet surface temperatures can be obtained. Individual controllers for each location may then be designed, provided there are no coupling effects. These controllers are then tested in real-time, for either step or ramp inputs.

4.2.4.1 IR sensor output conditioning

Unlike the thermocouple outputs for the embedded heating element temperatures, the IR sensor outputs have many possible options. The temperature measurement range for the Raytek Thermalert® MIC™ Miniature Infrared Sensor is 0-500°C, and the output selected was 0-5VDC. This output was within the 0-10VDC range of the A/D, so no additional conditioning was required. The sensor is not capable of measuring more accurately than 0.1°C, so the loss of resolution was not a major factor. The signal conditioning of the IR output signal is shown in Figure 4-32:

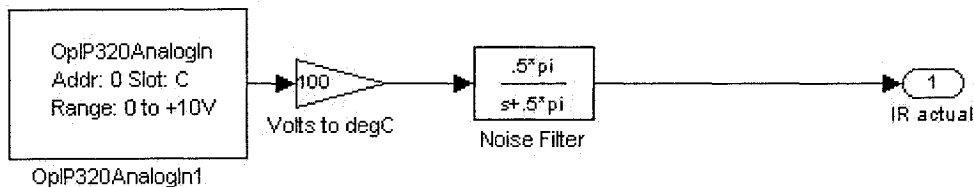


Figure 4-32: Signal conditioning of the IR output signal

The gain converts the output voltage back into a temperature, with the same lowpass noise filter that was designed for the embedded thermocouple outputs. The second output of the IR sensor is the ambient temperature of the sensor itself. This measurement is extremely important as the ambient temperature can begin to affect the sensor reading when it is above 85°C [27]. Above this temperature, air cooling must be applied to keep the sensors operating normally. The air flow to each sensor should be at least 0.65 litres per second. The maximum ambient temperature is 200°C, even with a high air flow.

In the AAA oven, the sensors are placed between the heating elements, and will reach temperatures above 85°C, especially when the heaters are at typical thermoforming operating conditions (above 300°C).

4.2.4.2 Steady-state relationship between heaters and sheet

In order to be able to control the sheet surface temperatures with the heating elements, the steady-state relationship between these two parameters must be determined. The steady-state experiment methodology and results are explained below.

4.2.4.2.1 Insulator sheet

Determining the steady-state relationship between the heating element temperatures and the plastic sheet surface temperatures is quite difficult. The sheet takes an extremely long time to heat, and will begin to melt and sag long before a steady-state temperature is reached. Therefore another material, with an emissivity similar to that of plastic, must be used for the steady-state experimentation. The emissivity needs to be close so that the

new material surface receives as much energy as the plastic sheet of comparable size and thickness would, and so that their respective temperatures are the same.

The material selected was a high temperature insulator sheet from D-M-E made from glass-reinforced polymer composite. The insulator sheet is primarily used in large industrial-scale plastic molds and die cast dies (see Appendix B for specifications). The primary role of the sheet is to inhibit heat transfer from the mold to the platen during forming. This conserves energy and will ultimately prolong the lifespan of the machine.

The size of the sheet was approximately 61cm by 91cm, or large enough to cover the entire heater tray. The major advantages of using this insulator sheet were its maximum heating temperature of 288°C, and its rigidity. The insulator sheet was also designed to remain at high temperatures for long periods of time. A plastic sheet at that high temperature would become molten extremely quickly and no longer hold its shape. This high tolerance temperature enabled the steady-state testing that was needed to determine the relationship between the sheet surface and heater temperatures.

4.2.4.2.2 Test Setup

Using the inner loop controllers, each of the 12 zones was set to 150°C. The IR surface temperatures were measured at points IRB1 (bottom centre), IRT1 (top centre), IRT2 (top front right – between heater zones T4 and T5), and IRT3 (top front left – between heater zones T5 and T6). Figure 4-12 above shows their approximate locations on the insulator sheet.

The first test was to establish the steady-state temperatures at each IR sensor location. Then, one zone at a time was raised by 50°C to 200°C and the resulting steady-state

temperature measurements were taken.

4.2.4.2.3 Experimental Results

The results can be seen in Table 4-3 below. The heater zone that has been raised to 200°C is in the left column.

Table 4-3: Open-Loop Insulator Sheet Step testing results

	<i>IRT1</i>	<i>IRB1</i>	<i>IRT2</i>	<i>IRT3</i>
Steady-State	116.5	110.6	98.9	99.4
B1	118.1	113.1	99.8	99.7
B2	121.1	120.9	99.4	100.1
B3	117.1	113.0	99.0	99.5
B4	118.6	113.3	104.2	100.1
B5	126.2	120.1	104.5	107.2
B6	119.1	113.5	100.0	103.5
T1	118.0	112.0	99.5	100.9
T2	122.5	116.9	100.6	102.6
T3	117.0	112.1	99.0	99.7
T4	118.0	110.6	108.9	1103.6
T5	126.6	113.3	108.8	112.0
T6	118.7	111.2	100.8	110.9

IRT2 and IRT3 are most affected when zones T4, T5 and T6 are increased, simply due to the larger view factors for these heating zones. It is also important to note that there are

only minor coupling effects between heating zones. For instance, if zones B1 and B2 were both raised 50°C, the effects on all IR sensors would be the same as summing the effects from each of the individual tests. This is a consequence of the linearization of the radiant heat transfer equation about the 150°C setpoint. Within a small heater operating range, all IR temperature changes become linear.

Using the data above, the steady-state gain m can be found from the following equation:

$$m_{IR,zone} = \frac{T_{IR_{new}} - T_{IR_{ss}}}{T_{zone_{new}} - T_{zone_{ss}}} \quad (4.6)$$

Here, $m_{IR,zone}$ represents the individual entries of the gain matrix M below. The subscript IR is the row index representing each of the IR sensors, and the subscript $zone$ the column index representing each of the heating zones. For a given heating zone, the denominator is simply the difference between the new heating zone temperature $T_{zone_{new}}$, or 200°C, and the steady-state heating zone temperature $T_{zone_{ss}}$, or 150°C, and is therefore always equal to 50°C. For a given IR sensor, the numerator is given by the difference between the new IR temperature measurement, $T_{IR_{new}}$, and its corresponding steady-state measurement, $T_{IR_{ss}}$, as stated in Table 4-3.

In this manner a 4×12 matrix M is defined:

$$M = 10^{-3} \times \begin{bmatrix} 32 & 92 & 12 & 42 & 194 & 52 & 30 & 120 & 10 & 30 & 202 & 44 \\ 50 & 206 & 48 & 54 & 190 & 58 & 28 & 126 & 30 & 0 & 54 & 12 \\ 18 & 10 & 2 & 106 & 112 & 22 & 12 & 34 & 2 & 200 & 198 & 38 \\ 6 & 14 & 2 & 14 & 156 & 82 & 30 & 64 & 6 & 84 & 252 & 230 \end{bmatrix} \quad (4.7)$$

Note that linear superposition applies for this system. For instance, if the heating

elements in zone B1 suddenly failed, the first column of the matrix M could be eliminated and the IR setpoints could still be reached using the inputs from the other 11 zones.

The next step is to invert the matrix M , so that from given IR setpoints, the new embedded setpoints can be calculated. But M is not square, and therefore, the pseudo-inverse must be calculated.

4.2.4.2.4 Pseudo-inverse

Given the $m \times n$ matrix M , the Moore-Penrose pseudo-inverse is M^+ of size $n \times m$ given in equation (4.8):

$$M^+ = M^T (MM^T)^{-1} \quad (4.8)$$

Such that equation (4.9) is solved:

$$u_0 = \left(M^T (MM^T)^{-1} \right) y \quad (4.9)$$

Here y is the 4x1 vector of IR sensor temperatures, and u_0 is the corresponding 12x1 vector of heating element embedded temperatures.

4.2.4.3 Steady-State Control of Sheet Temperatures

This section will demonstrate the effectiveness of the steady-state PI controller versus a simple open-loop control system. First, the transient sheet surface temperature responses will be studied for the purpose of building a model for each sensor. Then simple controllers will be designed to test these models. Finally these will be implemented on the real-time system and compared to the open-loop case.

4.2.4.3.1 Transient Sheet Surface Temperature Responses

The sheet surface temperatures at IRT1, IRB1, IRT2, and IRT3 are shown in Figure 4-33 for a nominal setpoint of 150°C on all heating elements.

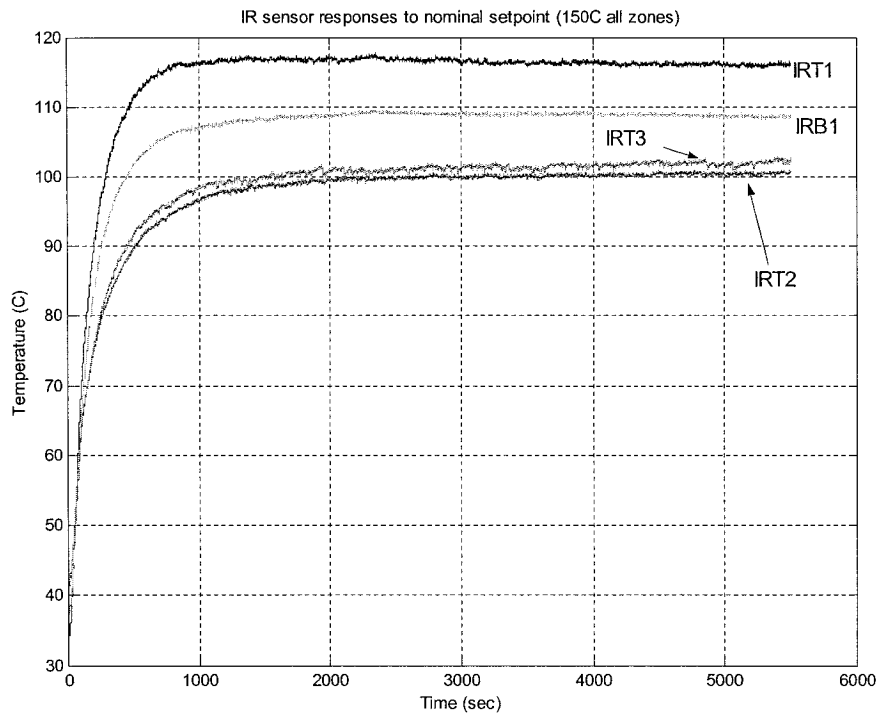


Figure 4-33: Transient Sheet Surface Temperature Responses

Note that each IR measurement takes at least 1000 seconds to reach a value close to its steady-state (IRT2 and IRT3 are much slower). By comparison, the heating elements reach their steady-state values 10 times faster (Figure 4-27). For this reason, the dynamics of the heating element were assumed to have very little effect on the sheet temperature. The heating elements are then presumed to reach their new setpoints instantaneously.

From these curves, simple first-order transfer functions can be determined. The

parameters K (gain) and τ (time constant) for each IR sensor are calculated from the actual data. Simple trial and error tuning of the first-order simulation was performed to obtain the correct time constants. The tuned first-order transfer functions for each sheet location are shown in Figure 4-34.

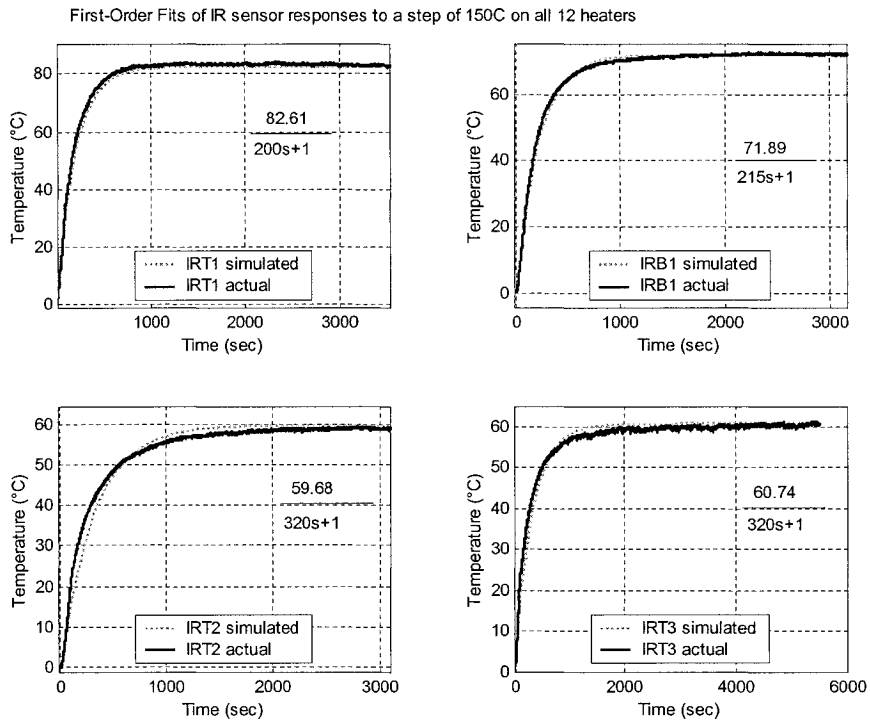


Figure 4-34: First-Order fit of IR sensor responses to 150°C step on all zones

From the data, it can be noted that certain sheet locations heat faster than others. For instance, the time constants in the centre of the sheet (i.e., for IRT1 and IRB1) are smaller than those on the periphery. This makes sense because the centre of the sheet has a larger view factor than the outer edges: it “sees” more heating elements and therefore receives more energy. Once all 14 sensors are installed, more comprehensive testing will be done to determine the geometrical effects on the time constants.

4.2.4.3.2 Model and Controller

The first-order responses can be modeled by a steady-state gain K and time constant τ , as was noted above. Using these values, a plant model can be built incorporating all the IR sensors. A set of controllers can then be designed to push the plant model to any desired setpoint. These controllers are decoupled, due to the linearization about the 150°C setpoint and the subsequent development of the gain matrix M . The block diagram is seen in Figure 4-35:

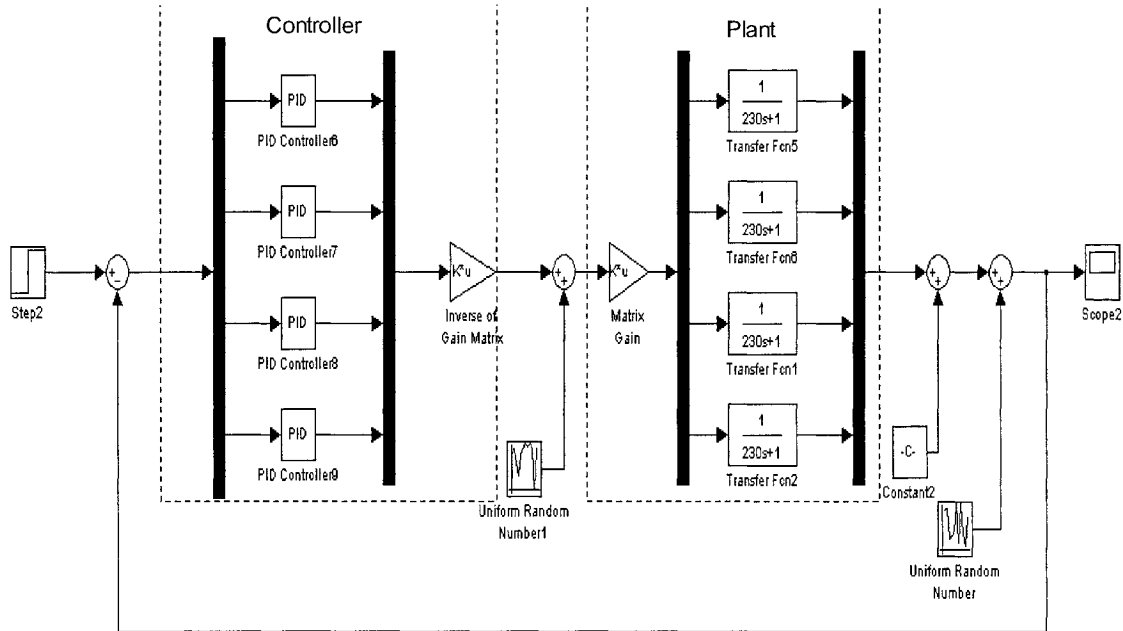


Figure 4-35: Simulink Model of Sheet/Heater system

The stable plant can then be perturbed with noise on both the input and output, as well as uncertainty on the gain matrix M . The magnitude of the uncertainty on M was 10 times the magnitude of M , i.e., each of the entries was increased by 1000%. Still, as can be seen in the figure, the sensor outputs converged to their setpoint values (IRT1 = 175°C, IRB1 = 150°C, IRT2 = 125°C and IRT3 = 100°C).

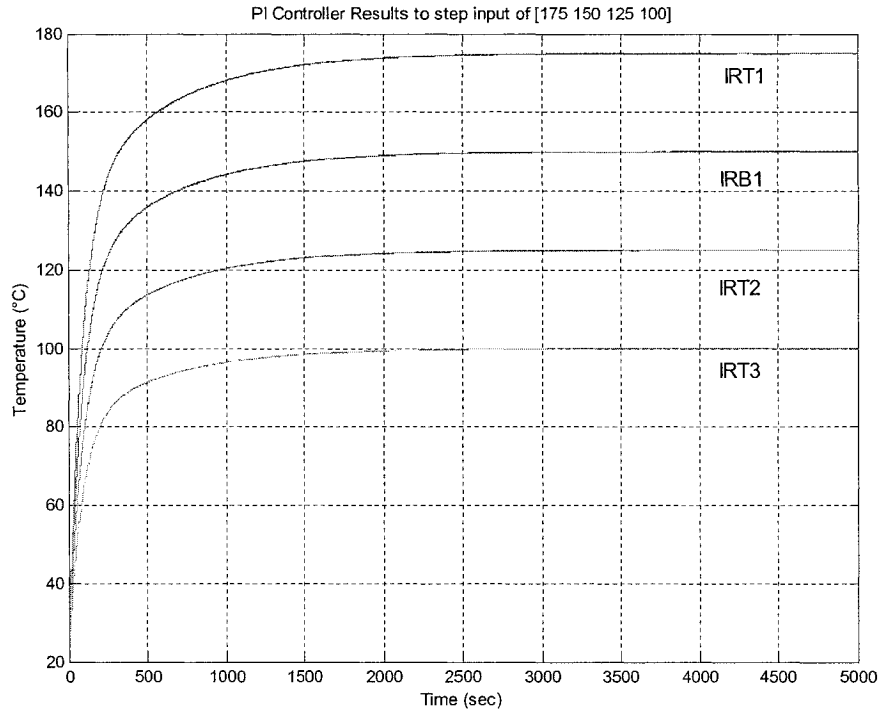


Figure 4-36: Simulated PI Control response to step I/P of [175 150 125 100]

The controller used in this case was a simple PI controller, as above. The proportional gain P was 2.1, and the integral gain I 0.0047. Again the individual PI controllers were tuned with a simple trial and error method. The results are satisfactory, with all IR sensors reaching their desired setpoints with no overshoot. This is primarily due to the stability of the plant (a slow first-order system).

4.2.4.3.3 Real-Time implementation

These PI controllers were then implemented and added to the existing RT-LAB model. The first figure below shows the results of open-loop control (the simple inversion of the gain matrix). In theory, this should reproduce the setpoints exactly, as the steady-state identification tests are essentially being duplicated here.

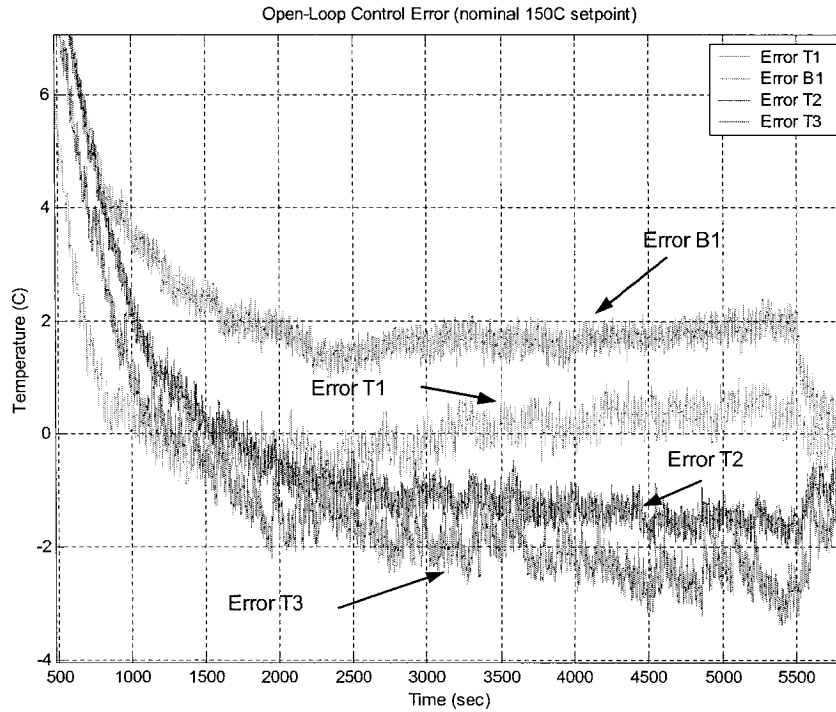


Figure 4-37: Open-loop Control of IR Measurements (nominal setpoint)

In practice, however, only IRT1 is within 1°C of its nominal measurement. The other IR sensors are even drifting away from their setpoints. As soon as the PI control is applied, though, the integral gain eliminates the steady-state error (see Figure 4-38).

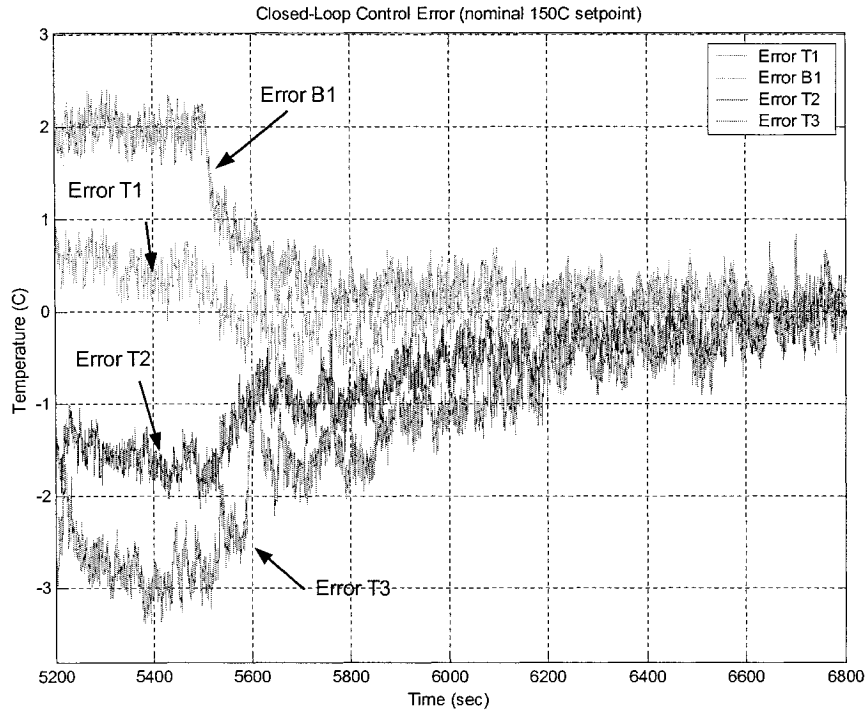


Figure 4-38: Closed-Loop Control of IR Measurements (nominal setpoint)

The PI control was turned on by manual switch at approximately 5500 seconds, according to the data. Within approximately 500 seconds, the errors on each IR measurement have dropped below 1°C. Figure 4-39 below shows the reactions of the heating elements before and after this moment. Before, the heating elements are oscillating around 150°C, and afterwards, are being controlled by the PI, and are therefore constantly being adjusted to maintain the outputs at their desired setpoints.

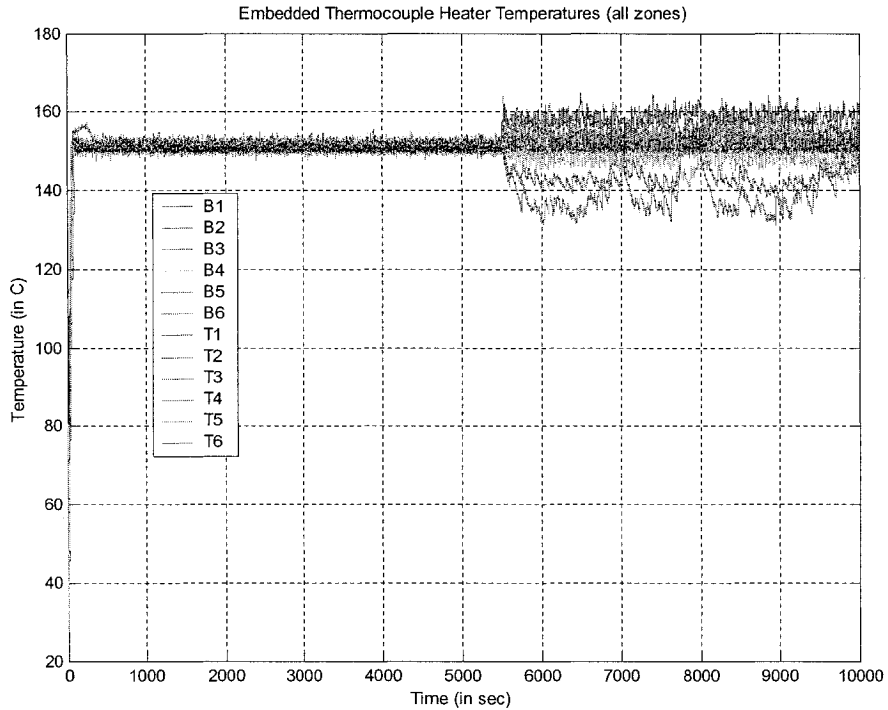


Figure 4-39: Embedded Thermocouple Heater Temperatures (all zones)

4.2.4.4 Ramp Input Control

In thermoforming, the plastic sheet is not heated to steady-state. Therefore, instead of a step input, a more typical input for a thermoforming oven is a ramp input, where the controller tries to follow a predetermined input slope over a given length of time. The limiting conditions in this case were to not to heat the insulated sheet over 200°C and not to exceed the fastest heating rate of the heating element. These tests are much shorter, since steady-state does not have to be attained.

The only addition to the controller is the velocity feedforward term that was discussed in a previous section. The velocity gains are different for each IR sensor because of the different ramp slopes. The block diagram of the velocity feedforward PI controller is in

Figure 4-40:

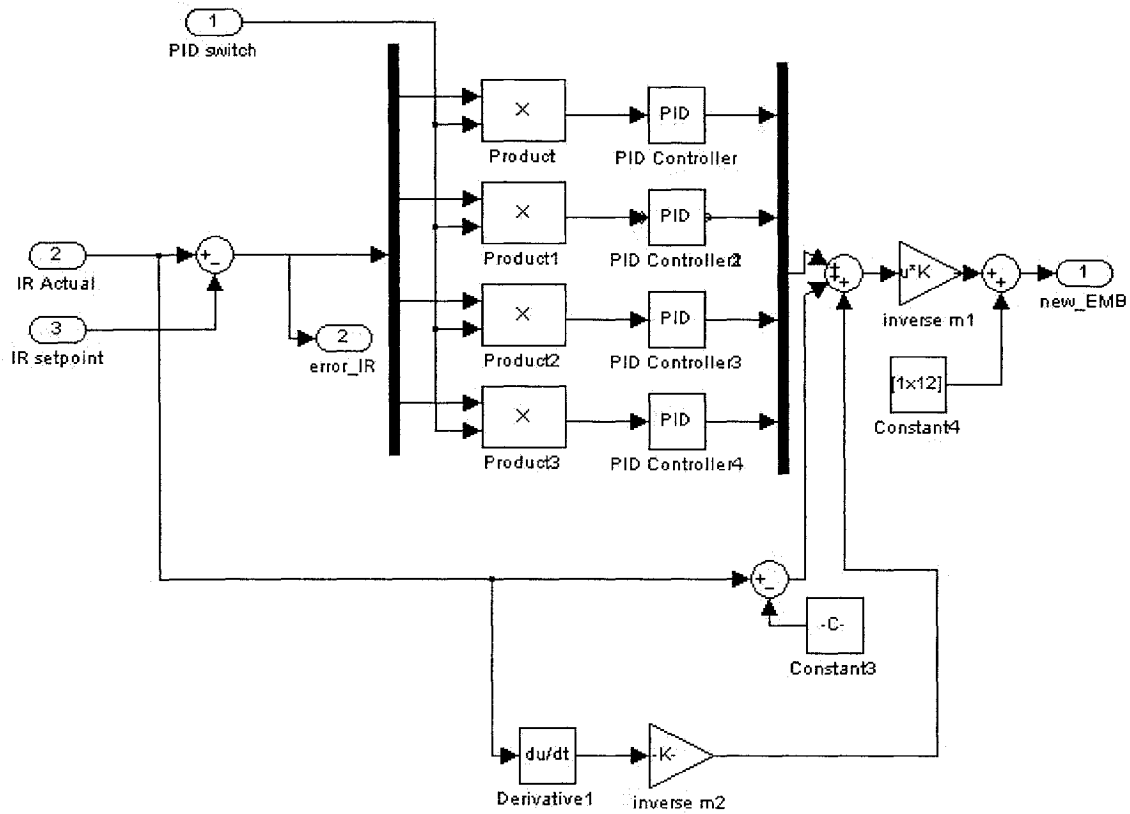


Figure 4-40: Velocity Feedforward PI controller for Ramp input

After some tuning, it was determined that the velocity gain K at the bottom of the figure is $[90 \ 120 \ 140 \ 140]$. The resulting ramp output and error curves for IRT1 are shown in Figure 4-41 and Figure 4-42:

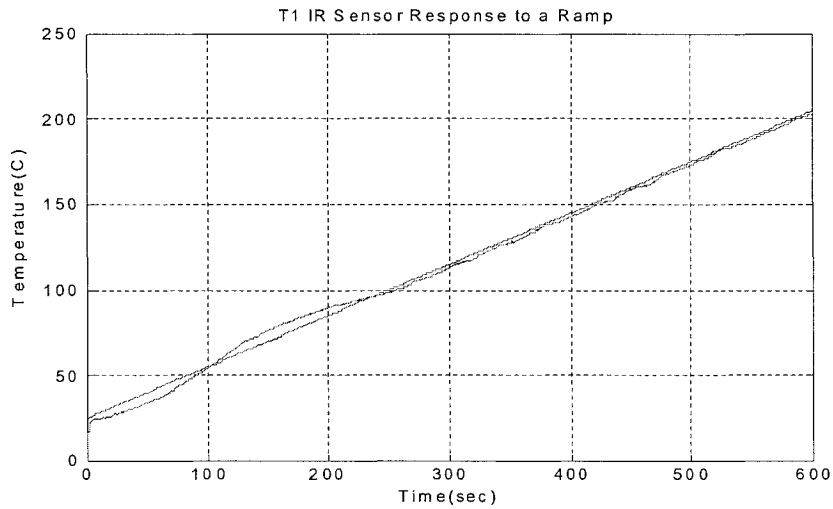


Figure 4-41: IRT1 Sensor Response to Ramp input

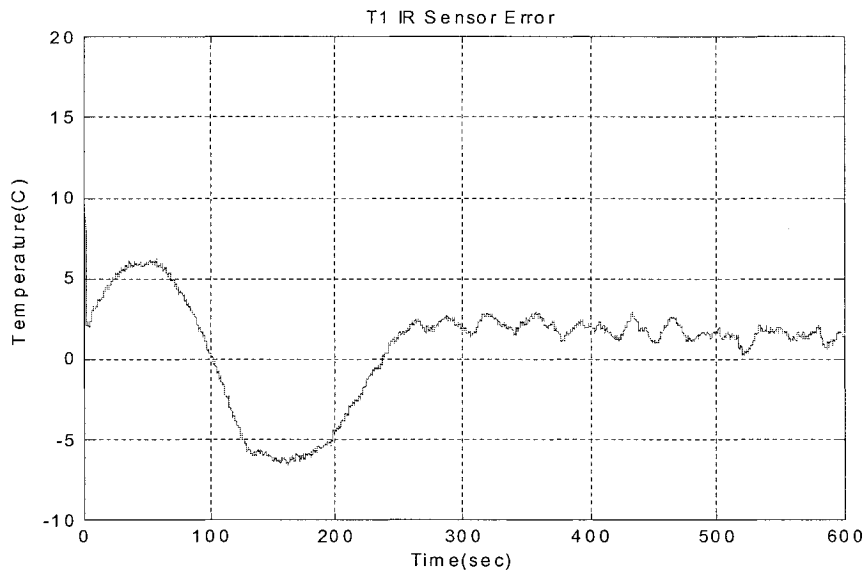


Figure 4-42: IRT1 Sensor Error for Ramp Input

Finally, Figure 4-43 shows the effect of the ramp input on the heating element temperatures. It is interesting to note that not all the heating elements are heated indefinitely, but some are asked to cool periodically.

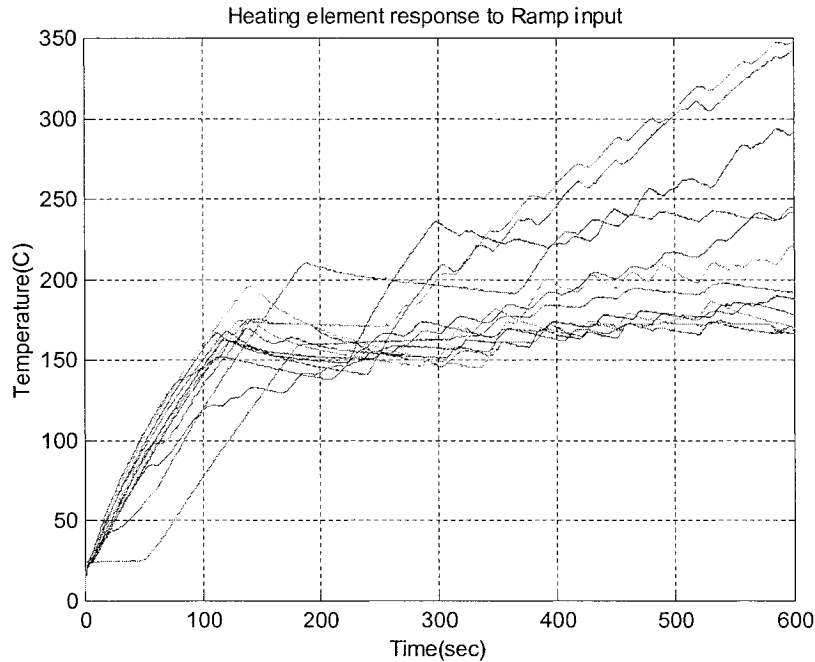


Figure 4-43: Heating Element Response to Ramp Input

Through all this discussion, the objective of controlling the temperature at different locations on the surface of a plastic sheet in real-time has been achieved. The IR sensor sheet temperature measurements can be controlled to within 1°C of a final steady-state value, or within 2°C of a ramp value. The ramp input is more typical of the thermoforming process, as each sheet will only be in the oven for a short length of time, and will not typically attain a steady-state value. With more precise desired input functions, the simple linear control methods devised in this chapter could be proven to be very useful in eliminating rejected parts, as well as decreasing the heating time. Both of these would increase throughput on a typical forming machine, a major benefit to industry.

Chapter 5 Conclusion

5.1 Summary

The objective of this thesis is twofold: to develop a reliable state-space model of sheet reheat for simulation analysis, and to develop and test an in-cycle real-time temperature controller for the sheet reheat stage of the thermoforming process. The primary reasons for this are to decrease the formed part rejection rate, and optimize the heating time. These will then lead to increased machine throughput, and even potentially decrease machine-related energy costs. A brief review of the literature followed, investigating the prospects of other real-time control algorithms implemented in industrial settings as well as the advantages and disadvantages of working with infrared technology.

In the next chapter, a model of the sheet heating phase was developed. Basic heat transfer theory was explained and then applied to the thermoforming sheet-heater system. The existing discretized sheet model was then improved by using the Beer-Lambert law to explain energy absorption within the sheet. The new state-space model was tuned to experimental results with great success, as most tuned model parameters were within their nominal range.

Finally, the real-time aspect was investigated. The dimensions of the existing oven were given, as well as the characteristics of both the actuators and the sensors. Infrared thermometry was briefly explained. The existing control structure was examined, and the real-time operating software was also described.

The real-time control algorithm was proposed in the final section. A linearization of the

non-linear state-space system was performed about a typical operating point. Inner-loop heating element controllers were designed and tested. The steady-state gain matrix between heating elements and sheet surface temperatures was determined next, enabling the modeling of the sheet surface temperature transfer functions. From these transfer functions, outer-loop PI controllers were designed. Finally, these were tested in real-time using both steady-state inputs and ramp inputs (to simulate a typical thermoforming run). The ramp results were satisfactory, maintaining the sheet surface temperatures within 5°C of the increasing ramp value.

To the author's knowledge, this was the first successful implementation of a real-time sheet temperature controller for thermoforming.

5.2 Recommendations and Future Work

The development of the real-time sheet reheat controller in thermoforming is far from complete. The work demonstrated in this thesis is but a small fraction of what remains to be done, before a commercially viable sheet reheat controller can be finalized.

The remaining IR sensors must first be installed into the oven, and the new gain matrix for all sensors must be calculated, using the D-M-E insulator sheet. This will give a more complete sheet surface temperature distribution, for both the top and bottom of the sheet. The sheet temperature transfer functions must then be identified for each IR sensor location, after which new PI controllers can be tuned and implemented. These new controllers will then be tested in real-time using the RT-LAB modeling software, both for step and ramp inputs. The ramp testing will then be repeated using HDPE sheets of different thicknesses, to demonstrate the effectiveness of the controllers in maintaining a

desired surface temperature distribution.

However, this only solves half the sheet reheat problem posed in the thesis introduction. The sheet heating time is not optimized in any way using these real-time PI controllers. But a tool has been developed to determine the sheet centerline temperature, namely the discretized sheet model. It has been established that there is no way to produce a formable part while measuring internal sheet temperatures using contact thermocouples. These would cause damage to the sheet, and most likely cause a rejected part. The discretized sheet model could then be used in real-time, in conjunction with the IR surface temperature measurements, in order to calculate the temperature at any depth within the sheet. Similar to the way Kalman filters are used for estimating position in aircraft control, the sheet model can be used to estimate the internal temperatures of the sheet. The IR sensor measurements are then used as time-varying boundary conditions, and as inputs to the Kalman filter. In this way, controllers can then be designed to optimize the heating time, by finding the correct parameters to increase the temperature at the sheet centre to the minimum forming temperature.

To fully demonstrate the effectiveness of this type of real-time model-based control system, the system would have to be tested against the existing open-loop “tweaking”-type control on an industrial scale. A typical batch should first be run for a given part under normal open-loop conditions, and repeated using the new model-based real-time in-cycle controller. The controller should decrease the part rejection rate, even while decreasing the heating time per part.

Chapter 6 References

- [1] Throne, James L. *Radiant Heat Transfer in Thermoforming*, ANTEC conference 1995, pp.810-821.
- [2] Lappin, J.F, Martin, P.J., *Sheet Temperature Measurement in Thermoforming*, ANTEC conference 1996, pp.878-882.
- [3] Yousefi, A., Bendada, A., DiRaddo, R., *Improved Modeling for the Reheat Phase in Thermoforming Through an Uncertainty Treatment of the Key Parameters*, Polymer Engineering and Science, May 2002, Vol. 42, No. 5, pp.1115-1129.
- [4] Duarte, F.M., Covas, J.A., *IR Sheet Heating in roll-fed Thermoforming Part I – Solving direct and inverse heating problems*, Plastics, Rubber and Composites 2002, Vol. 37, No. 7, pp.307-317.
- [5] Duarte, F.M., Covas, J.A., *IR Sheet Heating in roll-fed Thermoforming Part II – Factors Influencing Reverse Heating Solution*, Plastics, Rubber and Composites 1 Jan 2003, Vol. 32, No. 1, pp.32-39.
- [6] Monteix, S. et al., *Experimental study and numerical simulation of preform or sheet exposed to infrared radiative heating*, Journal of Materials Processing Technology 119 (2001), pp.90-97.
- [7] Bugbee, B., Droter, M., Monje, O., Tanner, B., *Evaluation and Modification of commercial infrared transducers for leaf temperature measurement*, Advanced Space Research, Vol. 22, No. 10, pp.1425-1434, 1998.
- [8] Schmidt, F.M., Le Maout, Y., Monteix, S., *Modelling of infrared heating process of thermoplastic sheet used in thermoforming process*, Journal of Materials Processing

Technology 143-144 (2003) pp.225-231.

[9] Baker, J.M., Noman, J.M., Kano, A., *A new approach to infrared thermometry*, Agricultural and Forest Meteorology 108 (2001), pp.281-292.

[10] Throne, James L., *Technology of Thermoforming*, Hanser/Gardner Publications, Inc., Munich, 1996, 882pp.

[11] Stewart, James, *Single Variable Calculus – 2nd edition*, Brooks/Cole Publishing Company, Pacific Grove, CA, 1991, 635pp.

[12] Belanger, Pierre, *Control Engineering – A Modern Approach*, Saunders College Publishing, Orlando, FL, 1995, 271pp.

[13] Sedra, A.S., Smith, K., *Microelectronic Circuits – Fourth Edition*, Oxford University Press, Inc., New York, NY, 1998, 1237pp.

[14] Tadmor, Z., Gogos, C.G., *Principles of Polymer Processing*, Wiley-Interscience Publications, New York, NY, 1979, 736pp.

[15] Holman, J.P., *Heat Transfer – Seventh Edition*, McGraw-Hill, Inc., New York, NY, 1990, 714pp.

[16] Moore, B., Girard, P., Boulet, B., DiRaddo, R., *In-cycle dynamics of forming operations*, Proc. 2002 American Control Conference, 2002, pp3349-3350.

[17] Moore, B., *In-Cycle Control of the Thermoforming Reheat Process*, McGill University, Montreal, Quebec, Canada, 2002, 141pp.

[18] Moran, M.J. et al., *Introduction to thermal systems engineering: thermodynamics, fluid mechanics, and heat transfer*, John Wiley and Sons, New York, NY, 2003, 562pp.

[19] Michaeli, W., van Marwick, J., Luling, M., *Quality Assurance in Thermoforming – Wall thickness distribution captured and regulated online*, Kunststoffe-Plast Europe 85

(9), pp.1316-1320.

[20] Sala, G., Di Landro, L., Cassago, D., A numerical and experimental approach to optimize sheet stamping technologies: polymers thermoforming, *Materials and Design* 23 (2002), pp.21-39.

[21] Safarty, M. et al., *Advance Process Control Solutions for Semiconductor Manufacturing*, IEEE/SEMI Advanced Semiconductor Manufacturing Conference, 2002, pp.102-106.

[22] Petterson, M., Stenstrom, S., Modelling of an electric IR heater at transient and steady state conditions - Part II: modelling a paper dryer, *International Journal of Heat and Mass Transfer* 43 (2000), pp.1223-1232.

[23] DiRaddo, R., Girard, P., Chang, S., *Process drift and model-based control of forming operations*, Proc. 2002 American Control Conference, 2002, pp.3588-3593

[24] Hossain, A., Choudhury, Z.A., Suyut, S., *Statistical Process Control of an Industrial Process in Real Time*, IEEE Transactions on Industry Applications, Vol. 32, No.2, 1996, pp.243-249.

[25] Peng, J, et al., *Real Time Optimization of Robotic Arc Welding Based on Machine Vision and Neural Networks*, Proceedings of the 24th Annual Conference of the IEEE, vol.3, 1998, pp.1279-1283.

[26] Boulet, B. et al., *Control of the Thermoforming Process*, 16èmes Entretiens Jacques Cartier Colloquium on Polymer Reaction Engineering: Modelling, Optimisation and Control, Dec 2-4, 2003.

[27] *Thermalert® MIDTM MICTM Miniature IR Sensor Operator's Guide*, Raytek Corporation, Rev.C, 01/02, <http://www.raytek->

northamerica.com/admin/file_handler/2ae6092f570efab9e577de9b6820919c/1051816133/MID_eng_RevC_Print.pdf

[28] *Visionary Solution™ Catalog: Section 7 Radiant Process Heaters*, TEMPCO Electric Heater Corporation, 2002, 46pp., <http://www.tempeco.com/Catalog/Section%207-pdf/Section%2007.pdf>

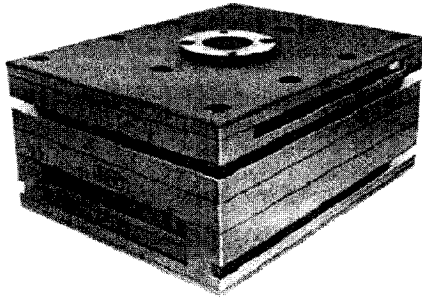
[29] Gruner, K-D., *Principles of Non-Contact Temperature Measurement*, Raytek Corporation, Rev. B, 2003, 32pp., http://www.raytek-northamerica.com/admin/file_handler/2ae6092f570efab9e577de9b6820919c/1017776674/IR_Theory_RevB_LR.pdf

[30] *RT-LAB v6.2 User's Manual*, Opal-RT Technologies, Inc., Rev. A, January 2003, 110pp., http://support.opal-rt.com/common/docs/pdf/rt-lab_usersmanual.pdf

Appendix A: List of Polymers

<i>Abbreviation</i>	<i>Polymer Definition</i>
ABS	Poly (acrylonitrile-butadiene-styrene)
CPET	Crystalline polyester (polyethylene terephthalate)
PET or APET	Amorphous Polyester (polyethylene terephthalate)
HDPE	High-density polyethylene
LDPE	Low-density polyethylene
HIPS	High-impact polystyrene
PC	Polycarbonate
PMMA	Acrylic (polymethyl methacrylate)
PS or PA	Nylon
PP	Polypropylene
PS	Polystyrene
PUR	Polyurethane
PVC	Polyvinyl chloride

Appendix B: D-M-E Insulator Sheet Specifications



- ASBESTOS-FREE MATERIAL
- HIGH COMPRESSION STRENGTH
- MACHINABLE WITH HIGH SPEED CUTTING TOOLS

D-M-E Standard High Temperature Insulator Sheets

FOR PLASTICS MOLDS AND DIE CAST DIES

D-M-E High Temperature Insulator Sheets are used on molds and dies between the top clamping plate and the stationary platen, and between the bottom of the ejector housing and the movable platen. The thermal insulating properties of this unique asbestos-free, glass-reinforced polymer composite inhibit heat transfer from the mold to the platen, or from the platen to the mold (depending on the application), which helps conserve energy and prolong machine life. These sheets have excellent non-deformation characteristics and a compressive strength* which is higher than asbestos and mica materials. Compression molded for high impact strength, they are supplied micro-finished top and bottom, parallel within $\pm .002$.

GENERAL DATA

Compressive Strength	(ASTM D-229)	49,400 psi at 75°F
		27,200 psi at 300°F
		18,000 psi at 400°F
		17,100 psi at 500°F
		15,000 psi at 550°F
Modulus of Elasticity in Compression	(ASTM D-229)	1.8 x 10 ⁵ psi at 75°F
		2.9 x 10 ⁵ psi at 425°F
Water Absorption	(ASTM D-229)	0.2%
Thermal Conductivity (K Factor) (Btu/hr/ft ² /in./°F)	(ASTM C-177)	1.9 at 75°F
		2.1 at 425°F
Flame Resistance	(UL Subject 94)	94V-0
Expansion Across Thickness	6.43 x 10 ⁻⁵ in/in/°F	
Expansion Across Surface	1.24 x 10 ⁻⁵ in/in/°F	
Maximum Recommended Service Temperature 550°F		

*49,400 psi at 75°F

ENERGY SAVINGS

1/4 THICK = 27,508 BTU/hr
1/2 THICK = 31,004 BTU/hr

HIGH TEMPERATURE INSULATOR SHEETS

THICKNESS	LENGTH	WIDTH	CATALOG NUMBER	NET WEIGHT
1/4	36"	18"	HTIS-1838-2	12
		24"	HTIS-2438-2	16
		36"	HTIS-3638-2	24
1/2	36"	18"	HTIS-1838-4	24
		24"	HTIS-2438-4	32
		36"	HTIS-3638-4	48

Special sizes available on special order:
Max. length = 96" Max. thickness = 1"
Max. width = 48" Min. thickness = 1/8"

Installation:
Use 1/4" 20 flat head screws
Drill & Tap base to suit.

Appendix C: Non-Linear Model MATLAB code

```
% function Thermal_light()
%
% (c) Guy Gauthier ing. and Mark Ajersch
%
% 12 juillet 2004
%
% This function determines the state-space model of the plastic sheet
temperatures.
% It also compares the model output to an input test vector, for tuning
purposes.
%
% Inputs: - Experimental test name
%         - Bottom Heat flag, Top heat flag
%         - Input Heater Settings
%
% Outputs: - Nodal sheet temperature distributions
%          - Error fcn between model and test

test_name = input('\nPlease enter Test Name here: ');
H_bottom = input('Heating from bottom (1 for Yes, 0 for No): ');
H_top = input('Heating from top (1 for Yes, 0 for No): ');
Heater_temp = input('Enter heater setpt temperatures (in C): ');

h = 0.5; %delta time
N = 10000; %number of points
t = (0:h:N*h); %time vector

Zt = 0.141; %distance in m from sheet to upper oven
Zb = 0.171; %distance in m from sheet to lower oven
Vft = AAA_view_factors_patrick(Zt); %view Factor top
Vfb = AAA_view_factors_patrick(Zb); %view Factor bottom

sbc = 5.669e-8; %boltzmann constant
emis = 0.45; %effective emissivity

l = 0.012/4; % delta thickness
Tambt = 115+273; %ambient air temperature top
Tambb = 145+273; %ambient air temperature bottom
hh = 30; % Convection coefficient
kk = (0.128/l)*.9; % Conduction coefficient

rho = 850; %density
Cp = 1700; %heat capacity

sx = 76.67e-3; %sheet zone width
sy = 102.5e-3; %sheet zone height
lo = 304.8e-3; %oven zone size

sevt = sbc*emis*Vft*(lo^2/sx*sy); %finding upper and lower multiplying
factors
sevb = sbc*emis*Vfb*(lo^2/sx*sy);
```

```

%ct = 1/(rho*Cp*1);

x(:,1) = (22+273)*ones(5*6,1); %initial sheet temps

%H_top    = 1; % If 0, heaters off # If 1, heaters work
%H_bottom = 0;

B_coef = 30; %absorption coefficient
Beer_1 = exp(-B_coef*1/2); %Beer-Lambert output for external layer
Beer_2 = exp(-B_coef*1);   %Beer-Lambert output for internal layer

u
([ones(6,1)*(Heater_temp+273)*H_top;ones(6,1)*(Heater_temp+273)*H_botto
m]).^4; %input vector

BB1 = []; BB2 = []; SEVt = [0;0;0;0;0;0]; SEVb = [0;0;0;0;0;0];
RAD1=[]; RAD5=[]; %initializations
for k=1:6;
    SEVt = SEVt + sevt(:,k);
    SEVb = SEVb + sevb(:,k);
    BB1 = [BB1;2*sevt(k,:)*(1-Beer_1);
           sevt(k,:)*Beer_1*(1-Beer_2);...
           sevt(k,:)*Beer_1*Beer_2*(1-Beer_2);...
           sevt(k,:)*Beer_1*Beer_2^2*(1-Beer_2);...
           2*sevt(k,:)*Beer_1*Beer_2^3*(1-Beer_1)]; %coefficients
for transmitted energy top
    BB2 = [BB2;2*sevb(k,:)*Beer_1*Beer_2^3*(1-Beer_1);...
           sevb(k,:)*Beer_1*Beer_2^2*(1-Beer_2);...
           sevb(k,:)*Beer_1*Beer_2*(1-Beer_2);...
           sevb(k,:)*Beer_1*(1-Beer_2);
           2*sevb(k,:)*(1-Beer_1)]; %coefficients for transmitted
energy bottom
    RAD1 = [RAD1 ;2*(1-Beer_1);...
            Beer_1*(1-Beer_2);...
            Beer_1*Beer_2*(1-Beer_2);...
            Beer_1*Beer_2^2*(1-Beer_2);...
            2*Beer_1*Beer_2^3*(1-Beer_1)]; %coefficients for
absorbed energy top
    RAD5 = [RAD5 ;2*Beer_1*Beer_2^3*(1-Beer_1);...
            Beer_1*Beer_2^2*(1-Beer_2);...
            Beer_1*Beer_2*(1-Beer_2);...
            Beer_1*(1-Beer_2);...
            2*(1-Beer_1)]; %coefficients for absorbed energy
bottom
end
BB = [BB1 BB2];

for k = 1:N
    if mod(k,100)==0 fprintf('*'); end
    if mod(k,1000)==0 fprintf('|'); end
    if mod(k,4000)==0 fprintf('\n'); end
    %rho = diag(1./(1000*Rho_poly_HDPE(x(:,k))));
    %Cp = diag(1./Cv_poly_HDPE(x(:,k)));
    ct = 1/(1*Cp*rho);
    B = ct*h*BB;
    SS1 = []; SS5= [];

```

```

    for k1 = 1:6
        for k2 = 1:5
            SS1 = [SS1 SEVt(k1)*x(1+(k1-1)*5,k)^4*H_top]; %radiant
energy striking top surface
            SS5 = [SS5 SEVb(k1)*x(k1*5,k)^4*H_bottom]; %radiant energy
striking bottom surface
        end
    end
    Sh = ct*h*(diag(SS1)*RAD1+diag(SS5)*RAD5); %radiant energy absorbed
by sheet
    Qrad = B*[u(1:6)*H_top;u(7:12)*H_bottom] - Sh; %net radiant energy

    dx = ct*h*deltaTemp_six_zones(x(:,k),Tambt,Tambb,hh,kk);
%conduction and convection energies
    x(:,k+1) = x(:,k) + dx + Qrad; %total energy distribution
end

% Plotting Simulated vs. Experimental results

data = load(test_name);
time = data(:,1);
T1 = data(:,2); %exp temperature at 1mm
T3 = data(:,4); %exp temperature at 3mm
T9 = data(:,8); %exp temperature at 9mm
T11 = data(:,10); %exp temperature at 11mm

% plotting experimental curves
figure(3)
P3= plot(time, T1,'r',time, T3,'g',time, T9,'b',time, T11,'k');
set(P3(1), 'LineWidth',2.5, 'LineStyle','--');
set(P3(2), 'LineWidth',2.5, 'LineStyle',':');
set(P3(3), 'LineWidth',2.5, 'LineStyle','-');
set(P3(4), 'LineWidth',2.5);
xlabel('Time (in sec)')
ylabel('Temperature (in C)')
title('Experimental Temperature Curves at 420C for 12mm sheet')
grid;
legend('1mm','3mm','9mm','11mm',0)

total = max(time);
if total > N
    fprintf('Simulation shorter than file length, please increase to at
least %f seconds', max(time));
else
    %concatenate simulation to data file length
    index = max(time)-mod(max(time),1);
    x7_sh = x(7,1:index*2)-273;
    x9_sh = x(9,1:index*2)-273;
    T3_sh = T3(2:length(T3)-1);
    T9_sh = T9(2:length(T9)-1);

    %calculating errors
    error_T3 = T3_sh - x9_sh';
    error_T9 = T9_sh - x7_sh';
end

```

```

% plotting errors at 3mm and 9mm depths
figure(4)
P4 =plot(time(2:length(time)-1), error_T3,'b',time(2:length(time)-1),
error_T9,'r');
grid;
set(P4(1), 'LineStyle', '--', 'Color', [0 1 1]); set(P4(2), 'Color', [0
0 0]);
xlabel('Time (sec)'); ylabel('Temperature (°C)'); title('Simulation
Error (vs. Experimental Data) at 280C for 12mm Sheet');
legend('Error at 3mm','Error at 9mm',0)

% calculating steady-state errors
ss_error3 = error_T3(length(error_T3))/max(T3_sh)*100;
ss_error9 = error_T9(length(error_T9))/max(T9_sh)*100;

fprintf('\n\nThe percent error at steady-state for 3mm is %5.2f%% \n',
ss_error3);
fprintf('The percent error at steady-state for 9mm is %5.2f%% \n',
ss_error9);

% plotting centre zone temperatures

figure(2)
P2=plot(t(1:index*2),x(6:10,1:index*2)-273);
grid
set(P2(1),'LineWidth',2.5, 'LineStyle',':', 'Color', [0 0 0]);
set(P2(2),'LineWidth',2.5,'LineStyle','-');
set(P2(3),'LineWidth',2.5,'LineStyle','--');
set(P2(4),'LineWidth',2.5,'LineStyle','-');
set(P2(5),'LineWidth',2.5);
xlabel('Time (sec)'); ylabel('Temperature (°C)'); title('Simulated
Model Temperature Curves at 280C for 12mm Sheet');
legend('Top Surface','9mm','6mm','3mm','Bottom Surface',0)

function dx = deltaTemp_six_zones(x,Tambt,Tambb,h,k)

% deltaTemp_6_zones calculates the incremental change in temperature
at any node
% due to conduction and convection only
%
% Synopsys: dx = deltaTemp_six_zones(x,SEV,Tamb,h,k)
%
% Entrées: x = actual temperatures (in °K)
% Tambt = top air temperature (in °K)
% Tambb = top air temperature (in °K)
% h = convection coefficient
% k = conduction coefficient (divided by distance b/w 2
nodes)
%
% Sorties: dx = Tempereure increments (in °K)
%

% (c) Guy Gauthier ing. and Mark Ajersch
%
% 12 juillet 2004

```

```

dx = [2*(h*(Tambt-x(1)) + k*(x(2)-x(1)));...
      k*(x(1)-2*x(2)+x(3));          k*(x(2)-2*x(3)+x(4));          k*(x(3)-
2*x(4)+x(5));...
      2*(h*(Tambb-x(5)) + k*(x(4)-x(5)));...
      2*(h*(Tambt-x(6)) + k*(x(7)-x(6)));...
      k*(x(6)-2*x(7)+x(8));          k*(x(7)-2*x(8)+x(9));          k*(x(8)-
2*x(9)+x(10));...
      2*(h*(Tambb-x(10)) + k*(x(9)-x(10)));...
      2*(h*(Tambt-x(11)) + k*(x(12)-x(11)));...
      k*(x(11)-2*x(12)+x(13));          k*(x(12)-2*x(13)+x(14));          k*(x(13)-
2*x(14)+x(15));...
      2*(h*(Tambb-x(15)) + k*(x(14)-x(15)));...
      2*(h*(Tambt-x(16)) + k*(x(17)-x(16)));...
      k*(x(16)-2*x(17)+x(18));          k*(x(17)-2*x(18)+x(19));          k*(x(18)-
2*x(19)+x(20));...
      2*(h*(Tambb-x(20)) + k*(x(19)-x(20)));...
      2*(h*(Tambt-x(21)) + k*(x(22)-x(21)));...
      k*(x(21)-2*x(22)+x(23));          k*(x(22)-2*x(23)+x(24));          k*(x(23)-
2*x(24)+x(25));...
      2*(h*(Tambb-x(25)) + k*(x(24)-x(25)));...
      2*(h*(Tambt-x(26)) + k*(x(27)-x(26)));...
      k*(x(26)-2*x(27)+x(28));          k*(x(27)-2*x(28)+x(29));          k*(x(28)-
2*x(29)+x(30));...
      2*(h*(Tambb-x(30)) + k*(x(29)-x(30)))]];

```